UNIVERSITAT ROVIRA I VIRGILI

FABRICATION AND CHARACTERIZATION OF POLYMER MICRO- AND NANOSTRUCTURES BY TEMPLATE-BASED METHOD

Raquel Palacios Higueras

ISBN: 978-84-693-9440-3
Dipòsit Legal: T.63-2011

ADVERTIMENT. La consulta d'aquesta tesi queda condicionada a l'acceptació de les següents condicions d'ús: La difusió d'aquesta tesi per mitjà del servei TDX (www.tesisenxarxa.net) ha estat autoritzada pels titulars dels drets de propietat intel·lectual únicament per a usos privats emmarcats en activitats d'investigació i docència. No s'autoritza la seva reproducció amb finalitats de lucre ni la seva difusió i posada a disposició des d'un lloc aliè al servei TDX. No s'autoritza la presentació del seu contingut en una finestra o marc aliè a TDX (framing). Aquesta reserva de drets afecta tant al resum de presentació de la tesi com als seus continguts. En la utilització o cita de parts de la tesi és obligat indicar el nom de la persona autora.

ADVERTENCIA. La consulta de esta tesis queda condicionada a la aceptación de las siguientes condiciones de uso: La difusión de esta tesis por medio del servicio TDR (www.tesisenred.net) ha sido autorizada por los titulares de los derechos de propiedad intelectual únicamente para usos privados enmarcados en actividades de investigación y docencia. No se autoriza su reproducción con finalidades de lucro ni su difusión y puesta a disposición desde un sitio ajeno al servicio TDR. No se autoriza la presentación de su contenido en una ventana o marco ajeno a TDR (framing). Esta reserva de derechos afecta tanto al resumen de presentación de la tesis como a sus contenidos. En la utilización o cita de partes de la tesis es obligado indicar el nombre de la persona autora.

WARNING. On having consulted this thesis you're accepting the following use conditions: Spreading this thesis by the TDX (www.tesisenxarxa.net) service has been authorized by the titular of the intellectual property rights only for private uses placed in investigation and teaching activities. Reproduction with lucrative aims is not authorized neither its spreading and availability from a site foreign to the TDX service. Introducing its content in a window or frame foreign to the TDX service is not authorized (framing). This rights affect to the presentation summary of the thesis as well as to its contents. In the using or citation of parts of the thesis it's obliged to indicate the name of the author.

UNIVERSITAT ROVIRA I VIRGILI
Departament d'Enginyeria Electrònica, Elèctrica i Automàtica

Fabrication and characterization of polymer micro- and nanostructures by template-based method

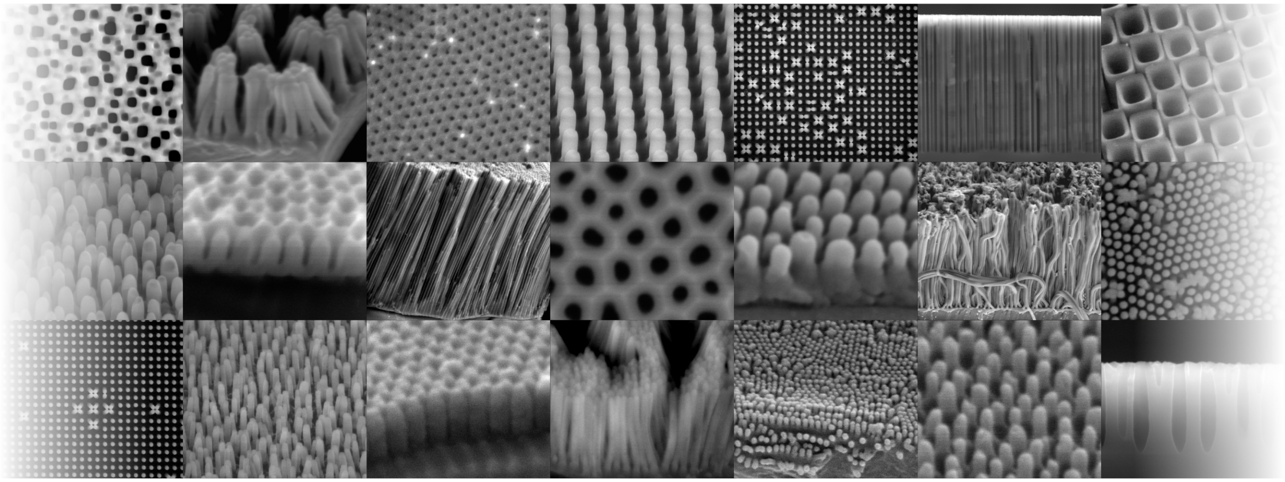

DOCTORAL THESIS

Raquel Palacios Higueras

Raquel Palacios Higueras

FABRICATION AND CHARACTERIZATION OF POLYMER MICRO- AND NANOSTRUCTURES BY TEMPLATE-BASED METHOD

Doctoral thesis supervised by
Dr. Lluís F. Marsal Garví

Departament d'Enginyeria Electrònica, Elèctrica i Automàtica

UNIVERSITAT ROVIRA I VIRGILI

Tarragona
2010

UNIVERSITAT
ROVIRA I VIRGILI

ESCOLA TÈCNICA SUPERIOR D'ENGINYERIA
DEPARTAMENT D'ENGINYERIA ELECTRONICA, ELÈCTRICA I AUTOMÀTICA

Avinguda dels Països Catalans, 26
Campus sescelades
43007 Tarragona
Tel. (977) 55 96 10
Fax (977) 55 96 05
e-mail: secelec@etse.urv.es
http://www.etse.urv.es/DEEEA/

I STATE that the present study, entitled "Fabrication and characterization of polymer micro- and nanostructures by template-based method", presented by Raquel Palacios Higueras for the award of the degree of Doctor, has been carried out under my supervision at the Department of Electrical, Electronic and Automatic Control Engineering of this university, and that it fulfils all the requirements to be eligible for the European Doctorate Award.

Tarragona, 20th September 2010

Doctoral Thesis Supervisor

Dr. Lluís F. Marsal Garví

Acknowledgements

First of all, I would like to express my deepest gratitude to my supervisor Dr. Lluís F. Marsal for his guidance, support, encouragement and invaluable advices throughout these years in all aspects of the work.

My special gratitude to Dr. Pilar Formentín for her support, suggestions, discussions and for her valuable guidance in the laboratory. And I am also grateful for her kindness and friendship during these years.

Many thanks are also given to Dr. Josep Pallarès and Dr. Josep Ferré-Borrull, and the colleagues in the NePhoS group for the coffee times and comradeship in the laboratory. My special thanks to Elisabet and Lukas for teaching me how to make porous silicon and alumina. And I am also grateful to Joaquin for his essential help with the bureaucracy.

Many thanks Dr. Trifon Trifonov at Universitat Politècnica de Catalunya for providing the macroporous silicon samples in the beginning of this thesis.

I would like to thank all the people of the Departament d'Enginyeria Electrònica, Elèctrica i Automàtica at Rovira I Virgili University, especially to Raúl and Roser for the help, support and the good moments.

As well, my gratitude to the technicians of Servei de Resursos Científics i Tècnics at Universitat Rovira i Virgili for the help and guidance with the equipments, and to Mariana for teaching me how to manage the ESEM.

I wish to thank Dr. Emilio Palomares and his group at Institute of Chemical Research of Catalonia (ICIQ), especially to Dr. Eugenia Martínez-

Ferrero for her kindness and help with the spectrophotometer and spectrofluorimeter equipments.

I am grateful to the Nanotechnology group at Tyndall National Institute, especially to Dr. Daniela Iacopino for her kindness that made possible my stage there, and for all the help, support and guidance.

The doctoral fellowship from Universitat Rovira i Virgili is gratefully acknowledged for making possible to conduct the doctoral work.

I wish to thank all my family, family-in-law and friends; despite the distance their encouragement was always invaluable. As well, I would like to thank Ainara because living this process together has been a great experience.

Finally but not the least, my deepest love to my mother and grandmother for all their cares for me, and to Loren for his unconditional love and understanding, and for his great patience these last months.

This work has been supported by Spanish Ministry of Ciencia e Innovación (MICINN) under grant number TEC2006-06531, TEC2009-09551 and TME2008-01342, HOPE CSD2007-00007 (Consolider-Ingenio 2010) and Generalitat de Catalunya under project number 2009 SGR 549.

Publications related to this thesis

Journal articles

P. Formentín, R. Palacios, J. Ferré-Borrull, J. Pallarès, L. F. Marsal, "Polymer-dispersed liquid crystal based on E7: Morphology and characterization", *Synthetic Metals* **158**(21-24), 1004-1008 (2008)

L. F. Marsal, P. Formentín, R. Palacios, T. Trifonov, J. Ferré-Borrull, A. Rodríguez, J. Pallarès, R. Alcubilla, "Polymer microfibers obtained using porous silicon templates", *Physica Status Solidi a* **205**(10), 2437–2440 (2008)

R. Palacios, P. Formentín, T. Trifonov, M. Estrada, R. Alcubilla, J. Pallarès, L. F. Marsal, "Semiconducting P3HT microstructures: fibres and tubes obtained from macroporous silicon template", *Physica Status Solidi (RRL)* **2**(5), 206–208 (2008)

R. Palacios, P. Formentín, J. Ferré-Borrull, J. Pallarès, L. F. Marsal, "Polymer nanopillars using self-ordered nanoporous alumina templates", *Physica Status Solidi c* **6**(7), 1584–1586 (2009)

L. F. Marsal, R. Palacios, A. Santos, P. Formentín, E. Martínez-Ferrero, J. Ferré-Borrull, J. Pallarès, "Synthesis and characterization of photoluminescent polymer micro- and nanopillar arrays", *ECS Transactions* **28**(3, Nanoscale Luminescent Materials), 105-113 (2010)

R. Palacios, P. Formentín, E. Martínez-Ferrero, J. Pallarès, L. F. Marsal, "β-Phase morphology in poly(9,9-dioctylfluorene) ordered nanopillars by template wetting method", *Nanoscale Research Letters* (Accepted)

R. Palacios, P. Formentín, E. Martínez-Ferrero, J. Ferré-Borrull, J. Pallarès, L. F. Marsal, "F8BT nanopillars from porous anodic alumina: influence of the solvent" (submitted to *Physica Status Solidi a*)

R. Palacios, P. Formentín, A. Santos, E. Martínez-Ferrero, J. Ferré-Borrull, J. Pallarès, L. F. Marsal, "Template-assisted fabrication and characterization of photoluminescent polymer nanopillars" (submitted to *Physica Status Solidi a*)

Communications to international conferences

R. Palacios, P. Formentín, J. Ferré-Borrull, J. Pallarès, L. F. Marsal, "Polymer nanopillars using self-ordered porous alumina templates", *Porous Semiconductors Sciencie and Technology*, Mallorca, Spain (2008) (poster presentation)

L. F. Marsal, P. Formentín, R. Palacios, L. Vojkuvka, T. Trifonov, A. Rodríguez, J. Ferré-Borull, J. Pallarès, R. Alcubilla, "Micro and nanostructures based on silicon and alumina templates for photonic and optoelectronic applications", *214th ECS Meeting, E5 - Integrated Optoelectronics 4*, Honolulu, USA (2008) (invited oral communication)

R. Palacios, A. Santos, P. Formentín, T. Trifonov, R. Alcubilla, J. Pallarès, L. F. Marsal, "P3HT micro- and nanostructures using ordered porous templates", *First International Conference on Multifunctional, Hybrid and Nanomaterials*, Tours, France (2009) (poster presentation)

L. F. Marsal, R. Palacios, P. Formentín, E. Martínez-Ferrero, A. Santos, J. Ferré-Borrull, J. Pallarès, "Fabrication and optical characterization of conducting and photoluminescent polymer micro- and nanopillars", *216th ECS Meeting, E7 - Organic Semiconductor Materials, Devices, and Processing 2*, Vienna, Austria (2009) (oral communication)

R. Palacios, P. Formentín, E. Martínez-Ferrero J. Pallarès, L. F. Marsal, "F8BT micro- and nanofibres from porous alumina and porous silicon", *Porous Semiconductors Sciencie and Technology,* Valencia, Spain (2010) (oral communication)

L. F. Marsal, R. Palacios, A. Santos, P. Formentín, E. Martínez-Ferrero, J. Pallarès, J. Ferré-Borrull, "Template-assisted fabrication and characterization of photoluminescent conducting polymer nanopillars", *Conference on Optical, Optoelectronic and Photonic Materials and Applications,* Budapest, Hungary (2010) (invited oral communication)

Communications to national conferences

R. Palacios, P. Formentín, T. Trifonov, J. Ferré-Borrull, J. Pallarès, A. Rodríguez, R. Alcublilla, L. F. Marsal, "Ordered arrays of polymer microfibers by using macroporous silicon as template", *Graduated Student meeting on Electronic Engineering*, Tarragona, Spain (2007) (poster presentation)

L. F. Marsal, P. Formentín, R. Palacios, T. Trifonov, J. Ferré-Borrull, A. Rodríguez, J. Pallarès, R. Alcublilla, "Ordered arrays of polymer microfibers obtained using macroporous silicon as template", *Trends in nanotechnology*, San Sebastián, Spain (2007) (poster presentation)

R. Palacios, P. Formentín, T. Trifonov, J. Ferré-Borrull, J. Pallarès, A. Rodríguez, R. Alcubilla, L. F. Marsal, "Polymer micro- and nanostructures from ordered porous templates", *Conferencia Española de Nanofotónica*, Tarragona, Spain (2008) (poster presentation)

R. Palacios, P. Formentín, A. Santos, T. Trifonov, R. Alcubilla, J. Pallarès, L. F. Marsal, "Technology development of polymer ordered micro- and nanostructures based on porous templates" *Spanish Conference on Electron Devices*, Santiago de Compostela, Spain (2009) (oral communication)

R. Palacios, P. Formentín, E. Martínez-Ferrero, J. Pallarès, L. F. Marsal, "Optical and Raman spectroscopic investigation of polymer micro- and nanopillars", *Graduated Student meeting on Electronic Engineering*, Tarragona, Spain (2010) (oral communication)

R. Palacios, A. Santos, P. Formentín, E. Martínez-Ferrero, J. Pallarès, L. F. Marsal "Synthesis and characterization of polymer nanopillars for photonic and optoelectronic applications", *Conferencia Española de Nanofotónica*, Segovia, Spain (2010) (poster presentation)

I have no special talents.
I am only passionately curious.

Albert Einstein

Contents

Chapter 1

Introduction

The preparation of micro- and nanostructures by distinct techniques has been investigated in recent years. The template assisted-technique was first reported by Martin et al. in 1991. This method is a suitable and versatile technique for preparing structures from metals, oxides and polymers. Polymers have been receiving an increasing interest for preparing micro- and nanostructures due to their applications in different areas in the micro- and nanotechnology. Conjugated polymers have optical and electrical properties which increase their applications in fields such as polymer light emitting diodes and polymer solar cells.

In this context, this thesis focuses on the study of template-assisted technique in order to prepare polymer micro- and nanostructures by different experimental processes and characterize the obtained structures. First, the fabrication of useful templates has been developed in home-made electrochemical cells. Macroporous silicon and self-ordered alumina appear as interesting templates due to the possibility of selecting the suitable dimensions in a large area. In order to infiltrate these templates, different methods have been developed, from vacuum-based to spin-coating processes. The obtained structures have been studied to investigate their properties by different techniques: scanning electron microscopy, UV-Vis absorbance, photoluminescence, X-ray diffraction and Raman spectroscopy.

This thesis is organized as follows:

Chapter 2 presents the state-of-the-art of the techniques for preparing polymer micro- and nanostructures. As well, the most common polymers employed to be infiltrated and their properties are introduced. We show some potential application of polymer micro- and nanostructures which start to be developed in the literature.

Chapter 3 is devoted to the preparation of the porous templates. Macroporous silicon, from n-type and p-type silicon, and self-ordered nanoporous alumina were obtained to be used as templates. The chemistry of the pore formation and the elements of the home-made electrochemical cell is studied for each case. As well, the main process sequence for each porous material preparation is detailed. We show the porous templates which can be obtained with pore diameter from 50 nm to 2 μm and pore depth from 200 nm to hundreds of microns.

Chapter 4 is concerned with the preparation of polymer micro- and nanostructures by template-assisted technique using different experimental processes. The vacuum-based infiltration, melt-assisted technique, wetting-based infiltration and spin-coating process are developed in order to prepare structures using different kinds of polymer, such as PMMA, PDMS and polymers from families as polythiophenes, PPV derivatives and polyfluorenes.

By these experimental methods, polymer structures as microtubes, microfibres, micro- and nanopillars are obtained.

Chapter 5 deals with the UV-Vis absorbance and photoluminescence characterization of the structures obtained by infiltration of conjugated polymers. The polymer solutions and films are studied using different solvents, which can modify their optical properties. Micro- and nanopillars are measured and compared in order to investigate the changes due to the micro- or nanostructure, the solvent and the experimental process.

Chapter 6 is dedicated to the study of the polymer structures characterization by X-ray diffraction and polarized Raman spectroscopy. X-Ray diffraction studied the crystallinity degree of polymer film, micro- and nanopillars. The polarized Raman spectroscopy provided information about the distribution and the preferential orientation of the polymer chains in films compared to nanopillars prepared with different solvents and by wetting-based or spin-coating method.

Finally, chapter 7 presents the conclusion of this work.

Chapter 2

State-of-the-art of micro- and nanostructures

In this chapter, the state-of-the-art of fabrication methods for micro- and nanostructures, especially the template-assisted technique which is the aim of this thesis, is presented.

By this technique, many materials can be structured, such as semiconductors, metals and oxides. We have paid attentions to the polymers, which can be employed in a wide range of potential applications in microfluidic devices, sensor, actuators, polymer light-emitting diodes (PLEDs) and polymer solar cells.

Finally, the fundamentals of the most promising applications are also presented.

2.1. Fabrication techniques for micro- and nanostructures

Fabrication of micro- and nanostructures has been receiving an increasing attention. At the moment, different techniques, such as lithography, electrospinning, self-assembly and template-assisted methods, to name a few, have been developed in order to fabricate micro- and nanostructures [1-4]. Structures developed can be classified in: 0 dimensions (0D) (particles), 1D (fibres, pillars), 2D (films) and 3D [5].

We have paid attention to 1D structures which can be generally classified in two large families depending on the aspect ratio (length/diameter): wires, fibres and tubes with high aspect ratio, and rods and pillars of lower aspect ratio [6].

The methods for preparing micro- and nanostructures are commonly characterized as “top-down” and “bottom-up”. Template-assisted, embossing and printing methods are primarily top-down approaches. Scanning probe lithography and self-assembly bridge top-down and bottom-up strategies, which often use templates fabricated by top-down methods to direct the bottom-up assembly of components.

All methods for preparing 1D structures have their own specificity and potentials that many cases do not cover the entire spectrum of the fabrication requirements. The suitable strategy, or a combination of various, strictly depends on the requirements for a particular application [2]. Some of most applied techniques are briefly explained below.

Lithography

Various techniques of lithography have been explored in the last decade such as photolithography, electron beam lithography, ion beam lithography, X-ray lithography and soft lithography. Briefly, lithography is a complex process that converts a design layout on a mask into the structure on a substrate. Although some new lithography techniques do not require a mask, one example of this is the serial writing with charged particles (electron or ion) which has the disadvantage of have low throughput and they are only suited for small area fabrication [2, 7-9].

Fig. 2.1 shows a typical photolithography process. The first step is the spin-coating of the photoresist, then the sample is exposed through the mask, and finally the patter is developed and transferred into the substrate.

Electrospinning

Electrospinning technique has been originally developed for generating ultrathin polymer fibres. Electrospinning uses electrical forces to produce polymer fibres with nanometer-scale diameters. Electrospinning occurs when the electrical forces at the surface of a polymer solution or melt overcome the surface tension and cause an electrically charged jet to be ejected. When the jet dries or solidifies, an electrically charged fibre remains [10-12].

Self-assembly

Self-assembly is defined as the spontaneous organization of two (or more) components into larger aggregates using covalent and/or noncovalent bonds [1]. The components assemble spontaneously in a predefined way to produce a larger structure in two or three dimensions. This self-assembly can be helped by an external force or spatial constraint. Many examples of this technique are presented in the literature [13].

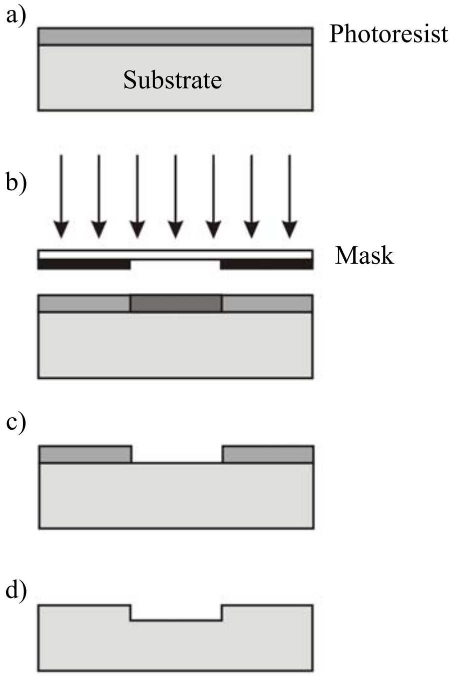

Fig. 2.1. Diagram of the photolithography process. (a) Spin-coating of the photoresist on the substrate, (b) exposure through the mask, (c) development of photoresist pattern and (d) transference of photoresist pattern into the substrate.

Template-assisted methods

The aim of this thesis is the development of the template-assisted technique, which was introduced first by Martin et al. [14-16] in 1991 in order to prepare metal microtubes.

This technique consists on the infiltration of a specific material into a cavity (called template) with a well-defined shape and, then, the template is removed (when a free structure is required) to obtain the inverse replica of the template [6]. It has the advantage of being able to create large area and arrays of structures with control over structural parameters.

This method of template infiltration does not required specialized equipment and is applicable to a wide range of materials such as polymers, metals, semiconductors and oxides [17-19]. For example, oxides and metals can be electrodeposited into the template.

This work is focused on polymer micro- and nanostructures prepared by this technique due to their promising application. They can be melted or infiltrated by a solution or, in some cases, a precursor is infiltrated and the polymerisation is carried out inside the template.

In general, the infiltration process of a solution-based or molten polymer by template-assisted technique consists in the steps illustrated in Fig. 2.2. Firstly, the polymer is placed on top of the template (Fig. 2.2a-d). Secondly, due to the high surface energy of the template compared to that of organic liquids such as polymer melts or solutions, a mesoscopic polymer film of a few tens of nanometers rapidly covers the pore walls of the template. When the template used is a membrane, the solidification of this film yields tubular structures with a length corresponding to the depth of the template pores. Then, the pores have not been completely filled by the polymeric solution (Fig. 2.2b). However, when the template is open only at one end, such as closed-end-pore silicon and alumina, a complete filling of the pore occurs [20-23]. In this case, obtained structures as replicas of the template pores are obtained (Fig. 2.2e). Fig. 2.2c-f show the obtained structures after removing the template.

In organic devices, size and shape of polymer structures and crystallinity or polymer chain orientation have been shown to have strong effect on charge-carrier mobility and overall device performance [24]. Furthermore, it has been found that the template-synthesized polymers have unique supermolecular features of electrochemical, electronic, optical and enhanced conductivity [25].

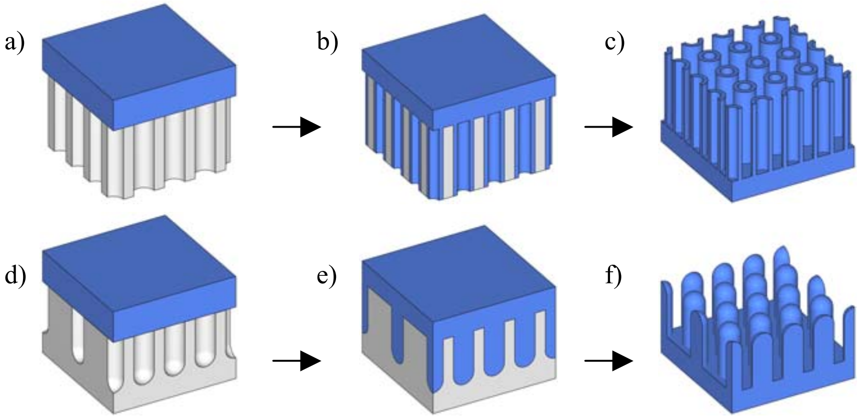

Fig. 2.2. Schematic diagram of (a–c) infiltration process using a membrane and (d–f) infiltration process using a substrate open only at one end. (a, d) A polymer solution is placed on top of the template. (b) A mesoscopic film of the liquid wets the pore walls in order to form tubular structures. (e) Polymer structures formed as replicas of the template pores. (c, f) Polymer structures after removing templates.

In template-assisted technique, the dimensions and shape of the polymer structures can be tuned by the dimensions of the template employed. In this sense, porous materials can be employed as templates. Porous silicon and alumina are attractive materials as template for many reasons, such as fabrication can be performed ordered in a large scale, and the porosity, pore size and pore depth can be tuned under appropriate preparation conditions.

Since the first studies of Uhlir [26] and Turner [27], the preparation of porous silicon by electrochemical dissolution of silicon wafers in solutions based on hydrofluoric acid (HF) has been developed. The surface of the silicon wafer must be contacted on the back and in contact with the HF solution. Applying a voltage between the wafer and an electrode in the HF solution, the silicon dissolution starts as pores. At the moment, macroporous silicon templates, disordered or ordered, with different dimensions and shapes can be prepared in HF solution.

We will apply porous silicon as template to prepare polymer microstructures with the desired dimensions. Potential applications of porous silicon are also presented in the area of opto-electronic devices, micro-optics, environmental monitoring (sensors), micromachining and biotechnology.

Furthermore, Masuda and Fukuda reported in 1995 a novel technique for aluminium anodization in two steps that is based on naturally occurring phenomenon of pore self-ordering [28]. By this two-step method, self-ordered nanoporous alumina templates can be prepared. The fabrication consists in a redox (reduction/oxidation) reactions which are simultaneously in progress on the electrodes. The aluminium (anode) is oxidized by negative electrolyte substances resulting in the formation of anodic oxide layer on the metal surface. Using the suitable acid solution and the fabrication parameters, a wide range of pore diameter and pore depth can be obtained.

Apart from the application as template in order to prepare polymer nanostructures, during last two decades, porous alumina has attracted much interest in the investigation and application fields due to its unique nanometric properties which are highly required in the world of nanotechnology.

2.2. Chemistry of polymer families

A polymer is a large molecule composed of repeating structural units typically connected by covalent chemical bonds. While polymer in popular usage suggests plastic, the term actually refers to a large class of natural and synthetic materials with a wide variety of properties

Some advantages of organic technology compared with the inorganic one are the possibility to tailor-make the electronic properties of materials in an almost infinite number of ways by chemical engineering and the possible use of flexible substrates [29].

Polymers have contributed to the development of highly innovative technologies. The polymeric structures can be applied in the area of micro- and nanoelectronic, microbiology, micro- and nanoengineering and microfluidics. In a view of this, a number of different properties, such as solubility, electrical conductivity, biological activity, reactivity, photoluminescence, optical absorption and order in a solid state, have been to be combined for optimising the applications.

During the latter half of the 20th century, polymer chemists have successfully developed the necessary tools to control various molecular structural parameter in polymers, such as their molecular weight and polydispersity, regio- and stereo-regularity, topology of repeat unit connectivity and to a limited extent even copolymer sequence distribution. However, the control over the next level of organization, namely chain conformation and the subsequent packing of chains, has proven to be a far more difficult task.

Some polymers with many potential applications in several of interesting fields are presented below.

Poly(methyl)methacrylate (PMMA) was initially developed in 1928. PMMA is an acrylic polymer that is lighter and has greater impact strength than glass. It is more easily scratched than glass, but has optical properties similar to glass in that it transmits up to 98% of light with low reflection. It is inferior to glass with respect to environmental stability and resistance to solvent, thought its environmental stability is better than most other plastics. As already noted, PMMA is often used as alternative to glass. PMMA is also employed in many devices in fields such as medicine due to its good compatibility with human tissues [30, 31].

Poly(dimethylsiloxane) (PDMS) has proven to be an outstanding material for micro- and nanotechnology. It is an elastomer with an excellent thermal stability, dielectric properties, and low temperature flexibility. PDMS is non-toxic, chemical inert, transparent in the UV-Visible regions and it has low polarity. As well, PDMS can be deformed reversibly and repeatedly without residual torsion. The cost of fabrication in PDMS is low compared to that for many materials (e.g. glass or silicon). These properties confirm that it is an excellent material for many applications in fields such as microdevices (valves, pumps and channels) and Micro-Electron-Mechanical Systems (MEMS) [32,33].

While polymer have been known and utilized broadly for many decades, polymers with the intrinsic properties of semiconductors and metals, such as conjugated polymers, are relatively recent phenomenon. The report about doped polyacetylene to achieve relatively high conductivity opened up important new vistas for physics and chemistry and for technology in general. [34].

In the 1960s-1970s, a breakthrough, polymer becoming electrically conductive, was coming-out. The breakthrough implied that a polymer has to imitate a metal, which means that the electrons in polymer need to be free to move and not bound to the atoms. This breakthrough was realized by three awarders of Chemistry Nobel prize in 2000, who were Alan J. Heeger at the University of California at Santa Barbara, USA, Alan G. MacDiarmid at the University of Pennsylvania, Philadelphia, USA, and Hideki Shirakawa at the University of Tsukuba, Japan. In 1977, they accidentally discovered that insulating π-conjugated polyacetylene could become conductor with a conductivity of 10^3 S/cm by iodine doping. The unexpected discovery not only broken a traditional concept, which organic polymers were only regarded as the insulators, but also establishing a new filed of conducting polymers [35].

Early studies recognized that the key feature of conjugated polymers was a backbone consisting of alternating single and double bonds resulting in a “π-conjugated network”. That is a conjugated π-electron system which is formed by the p_z-orbitals and sp^2-hybrized C-atoms in the molecules (Fig. 2.3). The lowest electronic excitation of conjugated molecules are de π-π*-transitions. The energy gap can be controlled by the degree of conjugation in a molecule. Thus, chemistry offers a wide range of possibilities to tune the opto-electronic properties of organic semiconducting materials. In the past decade, interest also has increased in the semiconducting forms of these polymers, including their photophysics and their use in a wide variety of devices [36].

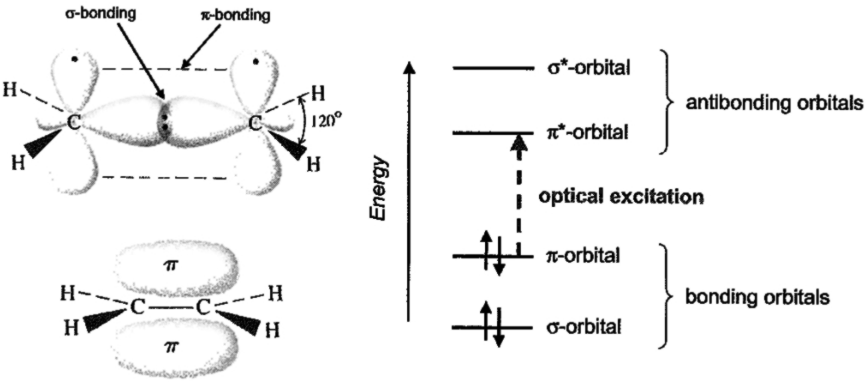

Fig. 2.3. (a) σ- and π-bonds in ethane, as an example for the simples conjugated pi-electron system. (b) The energy levels of a π-conjugated molecule. The lowest electronic excitation is between the bonding π-orbital and the antibonding π*-orbital [36]

In general, a material with conductivity less than 10^{-7} S/cm is regarded as an insulator. A material with conductivity larger than 10^{3} S/cm is called as metal whereas the conductivity of a semiconductor is in a range of 10^{-4}-10 S/cm depending upon doping degree.

The insulating conjugated polymers can be converted to conducting polymers by a chemical or electrochemical doping and which can be consequently recombacked to insulated state by de-doping. This suggest that not only de-doping can take place in conducting polymers, but also doping/de-doping process, which is different from inorganic semiconductors where the re-doping cannot take place. Conductivity of conducting polymer at room temperature covers whole insulator-semiconductor-metal region by changing doping degree.

Furthermore, one of the major attractions of conjugated polymers, as material for devices, is their processability from solution, using spin-coating or other solution-processing technique, such as template-assisted technique.

2.2.1. Polyfluorenes

Polyfluorenes (PF) are conjugated polymers which have been recently studied due to the interesting properties, such as their high quantum yield and good charge transport. Fig. 2.4 shows the chemical structure of a polyfluorene molecule. The photophysical properties can be tuned through the use of copolymers, blends and side chain modifications resulting in an enhancement of device characteristics [37]. The first report on synthesis of soluble poly(9,9-dialkylfluorenes) was given by Yoshino et al. in 1989 [38].

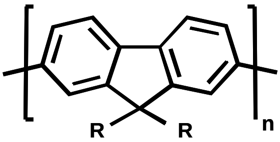

Fig. 2.4. The chemical structure of a polyfluorene molecule.

The photophysics of PF-type polymers has been intensively studied and impressive improvements concerning colour purity and device stability of PF-based devices have been made. They have emerged as emitting materials suitable due to their highly efficient photoluminescent and their thermal and oxidative stability [39].

One of the most well-known polyfluorenes is the poly(9,9-dioctylfluorene) (PFO) which emits in the blue region. The most important properties of this polymer are its highly efficient photoluminescence, good thermal and chemical stability at elevated temperatures and solubility in organic solvents. In addition, the polymorphism of PFO provides to study the influence of phase morphology on the photophysics of it without chemical modifications. Four different phases, nematic phase (N), two crystalline phases (α, α′) and β-phase, of this material may exist, which can be identified by spectral features apparent in absorption and photoluminescence [40-44]. A well-studied example is the β-phase (Fig. 2.5), which is a phase with a planar zigzag conformation resulting in an extended conjugation length. Recently, β-phase PFO has been shown as a favourable environment for charge carriers, with an enhanced charge carrier mobility [43]. These properties make it a good material for organic display devices. β-Phase morphology may be induced by different experimental process [43, 45] and the incorporation of it into polyfluorene nanostructures could be an interest advanced in order to exploit the benefits of this morphology in polymer structures based in photonic and electronic devices.

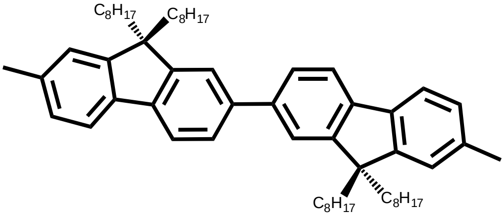

Fig. 2.5. The chemical structure of a segment of a PFO chain in the β-phase conformation. In β-phase PFO, the rotational angle between monomer units is fixed at 180º.

Poly(9,9-di-n-octylfluorene-alt-benzothiadiazole) (F8BT) and Poly[(9,9-dioctylfluorenyl-2,7-diyl)-co-bithiophene] (F8T2), poly[10,10-bis(2-ethylhexyl)-10*H*-spiro(anthracene-9,9'-fluorene)-2',7'-diyl-co-bithiophene] (SFT2) are examples of PF copolymers.

For example, F8BT, which emits in the green region of visible spectrum, has been extensively used in blends with other fluorene copolymers for efficient light-emitting diodes and photovoltaic cells, in which F8BT plays the role of the electron transports agent [46]. Optoelectronic and structural properties of F8BT are well established [47]. In contrast, F8T2, which emits in the yellow region of the visible spectrum, shows good hole transporting properties, which allows better chain packing via self-assembly, as know in many studies of organic field-effect transistors [48].

2.2.2. PPV derivatives

The first report of electroluminescence in the conjugated polymer poly(*p*-phenylene vinylene) (PPV) in 1990 has led to a major effort to develop light emitting diodes (LEDs) based on PPV and its derivatives and to understand the chemistry and physics for the fabrication and operation of these devices [49]. The chemical structure of PPV is shown in Fig. 2.6. PPV is insoluble so it is processed via a soluble precursor polymer. By substituting alkoxy groups on the benzene ring, it is possible to achieve polymers which are soluble. The most common PPV derivative is the orange-red emitting polymer poly(2-methoxy-5-(2´-ethyl-hexoxy)-1,4-phenylenevylene) (MEH-PPV) which has been extensively investigated in photovoltaic devices [50].

Poly(2-methoxy-5-dodecyloxy-*p*-phenylenevinylene) (MDDOPPV) and poly(2-methoxy-5-(3',7'-dimethyloctyloxy)-1,4-phenylenevinylene) (MDMO-PV) are also PPV derivatives [51]. MDMO-PPV is a donor semiconducting polymer commonly used for light emitting diodes and photovoltaic devices [52].

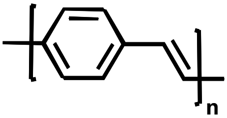

Fig. 2.6. The chemical structure of a poly(*p*-phenylene vinylene) (PPV) molecule.

2.2.3. Thiophenes

Finally, one of the most interesting polymer families for semiconductor and optical applications are polythiophenes. Due to the relatively low band gap of the polythiophenes, they emit in the red range. However, the gap is very sensitive to the torsion angle between consecutive thiophene units, and theoretical study has suggested that it may vary from the perfectly planarized chain to chains with torsion angle of 90º. Fig. 2.7 presents the chemical structure of a polythiophene molecule.

Poly(3-hexylthiophene) (PHT) and poly(3-alkylthiophenes), for example poly(3-alkylthiophene) (P3AT), belong to the polythiophenes [53], [54]. An example of a well-known polythiophenes is Poly(3-hexylthiophene-2,5-diyl) (P3HT). It is a donor polymer which has attracted a lot of attention due to its high charge carrier mobility among the conjugated polymers and its high hole mobility. These characteristics make P3HT a good candidate for polymer photovoltaic applications [55, 56].

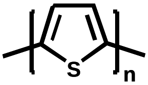

Fig. 2.7. The chemical structure of a polythiophene molecule.

2.3. Polymer devices applications

Polymers have a wide range of potential applications in different fields, such as medicine, sensor, actuators and opto-electronic devices.

The fabrication and characterization of structures obtained from conjugated polymers have attracted an increasing interest. These polymers have been established themselves as useful components in opto-electronic devices, such as field-effect transistors (FETs), polymer light-emitting diodes (PLEDs) and organic solar cells [57].

Many polymer-based devices can be found in the literature. The most interesting applications for polymer (1D) structures are presented below.

Sensor and actuators

Due to their properties, PDMS and PMMA have a wide range of potential application in fields such as microfluidics devices for microanalysis [33]. PDMS microstructures can be also employed for actuators as is shown in the literature [32, 58-60].

Furthermore, novel biosensors are always needed for improving modern medical diagnosis and biomedical research. Optical and/or electrochemical properties of some conjugated polymers can be dramatically altered by the specific presence of relatively few copies of various biomolecules, such as DNA, RNA, proteins and cells. Depending on the detection methods, sensor can be classified as: colorimetric, fluorometric and electrochemical. The development of these polymeric biosensors is an increasing direction of research [61].

Field effect transistors

Organic field-effect transistors (OFETs) are 3-terminal devices in which the charge carrier density in the channel between source and drain contacts can be controlled by the applied gate voltage across a thin dielectric [62, 63]. Fig. 2.8 shows the typical field-effect transistor.

OFETs are devices where the π-π interactions are extremely important in governing the mobility of the carrier, one of the main factors in the working mechanism of these devices. So, to optimise it is necessary the overlap among the π backbones of the polymer, and usually a crystalline order is the best way to obtain that [64]. It can be anticipated that strong π-π interaction can be obtained due to 1D structures to produce higher field-effect mobilities [65].

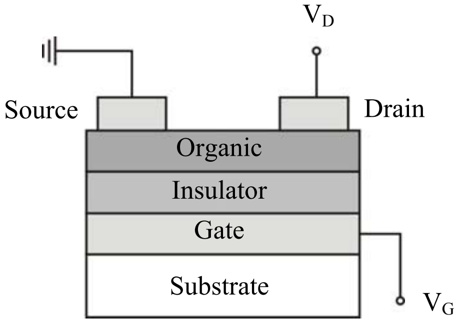

Fig. 2.8. The basic structure of a organic field-effect transistor (OFET) in p-channel.

Photovoltaic devices

Light emitting diodes (LEDs) are one of important electronic device. The light emission process in LEDs consists of charge injection, separation and transport of the injected charges and radiative decay of single exciton.

For the preparation of highly efficient organic LEDs, string interchain interactions should be avoided because they are responsible for the decrease in the electroluminescent efficiency, so highly amorphous materials with high interchain distances are desirable [64].

The basic structure of a typical bilayer polymer light emitting diode (PLED) is shown in Fig. 2.9. The first layer above the glass substrate is a transparent conducting anode, typically indium tin oxide (ITO). The single- or multi-layer polymer films are deposited on the transparent anode. Appropriate multiplayer structures enhance the performance of the device. Hence, the layer deposited on the anode would generally be a good hole transport material, providing the hole transport layer (HTL). Similarly, the polymer in contact with the cathode would be the optimised electron transporting layer (ETL) [49].

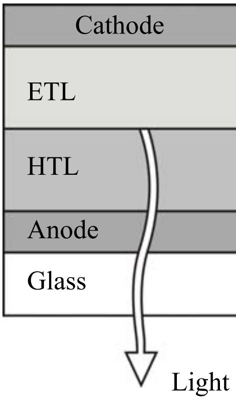

Fig. 2.9. The basic structure of a bilayer polymer light emitting diode (PLED).

The other important application of conjugated polymers is in organic photovoltaic cells. Photovoltaic cells are able to directly convert light into electric power so that is cheap and friendly environment energy source. Inorganic semiconductor-based photovoltaic cells have been widely used as common solar cells but other materials have been also explored for this application.

In order to prepare an efficient organic solar cell, the light-generated excitons need to diffuse to the donor-acceptor interface to reach the dissociation centre. The exciton diffusion length limits the width of the effective photo-active region. Many optimisations have been developed in order to increase the surface area of the donor-acceptor interface [64].

This can be overcome by hybrid photovoltaic cells consisting of semiconducting polymers and nanocrystalline metal oxides. These devices have gained attention as promising photovoltaic cells. They can be easily patterned into continuous 3D network for electronic conduction as well as having good mechanical and chemical stability [48, 66, 67].

One of the most promising device structures for organic photodevices is the bulk-heterojunction, where a hole-conducting polymer is blended with an electron-conducting small molecular compound, such as P3HT with a fullerene derivative, respectively [68].

Other technique could consist in devices containing structures donor/acceptor interspaced with an average length equal or less than the exciton diffusion length [69-71]. These solar cells structured can be polymer 1D nanostructures as Fig. 2.10 shows.

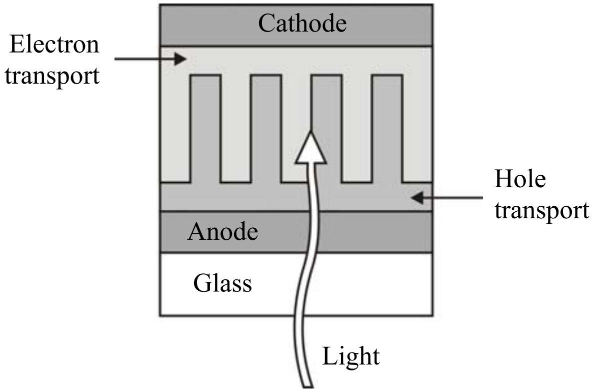

Fig. 2.10. The basic structure of organic solar cell structured.

Chapter 3

Macroporous silicon and nanoporous alumina templates fabrication

This chapter is devoted to the preparation of macroporous silicon and nanoporous alumina. Both porous materials are used as templates in the following chapters in order to prepare polymer micro- and nanostructures as inverse replicas of them by template-assisted technique.

Porous silicon and aluminium oxide, commonly called alumina, can be prepared ordered in a large scale, and the porosity, pore size and pore depth can be tuned under appropriate fabrication conditions [28]. Porous silicon is prepared by electrochemical etching in hydrofluoric acid (HF) solution, and self-ordered porous alumina is fabricated by two-step anodization in acid solution. In order to obtain ordered macroporous silicon, the silicon wafer must be pre-treated as is explained below.

By these experimental processes, we have prepared disordered macroporous silicon, using p-type silicon, ordered macroporous silicon, using n-type silicon, and self-ordered nanoporous alumina.

3.1. Macroporous silicon

The preparation of porous silicon by electrochemical dissolution of silicon wafers in solutions based on hydrofluoric acid (HF) has been developed since the first studies of Uhlir [26] and Turner [27], but the fabrication of macropores in an arbitrary pattern using a pre-structured n-type silicon electrode was first reported in 1990 by Lehman and Föll.

In order to prepare porous silicon, the surface of the silicon wafer, contacted on the back, is in contact with a solution containing HF. After applying a voltage (in the right direction) between the wafer backside contact and an electrode in the HF solution, the pore growth by silicon dissolution starts, provided certain key parameters are set correctly.

The silicon wafer must be anodically biased. This corresponds to forward biasing for p-type silicon, and reverse biasing for n-type silicon. In order to prepare porous silicon the current at the silicon side of the silicon/electrolyte interface must be carried by holes, injected from the bulk towards the interface. The current must be kept between zero and the electropolishing threshold. This limit depends on the etching parameters and wafer doping. In order to achieve significant hole current in n-type silicon, external illumination of the sample is required, depending on the doping level. If the current exceeds the electropolishing threshold, the anodization results in a progressive, complete removal of silicon. After this electropolishing, the wafer has a mirror-like appearance.

If a flat polished silicon wafer is etched in HF electrolyte the pores will grow randomly across the sample surface, with average pore diameters and spacing depending on the substrate resistivity and applied current. To get ordered pores we need first to prepare the sample, marking the sites where pores should grow.

3.1.1. Chemistry of porous silicon formation

Up to now, several different mechanisms regarding the dissolution chemistry of silicon have been proposed but it is generally accepted that holes are required for both electropolishing and pores formation.

The global anodic semi-reaction can be written during pore formation as

$$Si + 6HF \rightarrow H_2SiF_6 + H_2 + 2H^+ + 2e^- \qquad \text{(eq. 3.1)}$$

The final and stable product for silicon in HF is H_2SiF_6, or some of its ionized forms; it follows that during the pore formation only two of the four available silicon electrons participate in an interface charge transfer while the remaining two undergo a hydrogen formation (bubbles).

Pores grow preferentially along (100) directions and silicon dissolution occurs mainly at the pore tips, where enough holes are available. For the case of n-type silicon, the application of back-side illumination in potentiostatic regime allows further control on the hole injection, both in terms of carrier flux (which is proportional to illumination intensity) and localization of the injection, which is concentrated in the region of the pore tips, acting as hole collectors. Then, the etching process leads to a very regular pore growth.

The dissolution reaction begins at defects on the silicon wafer surface, the pores are formed and their walls are eroded until they are emptied of the holes. This formation process passivates the walls from further attack, and the reaction proceeds at the pore end, as has been represented in Fig. 3.1.

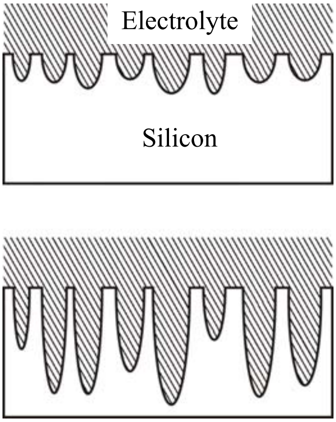

Fig. 3.1. Diagram of the porous silicon formation. The upper figure shows the initial stage, where the pores develop randomly on the silicon surface. The bottom figure shows how the dissolution advances only at the pore tips.

The preparation of porous silicon with electrochemical etching has been widely developed by many authors [72-77]. The most important parameters which determine the characteristics of porous silicon obtained by electrochemical etching are: the doped of the silicon wafer (type and resistivity), the electrolyte composition, the current density across the wafer, the time of current application and, in n-type silicon, the back-side illumination because hole supply is needed.

In n-type silicon, there are other effects that should be taken into account in order to obtain macropore arrays with good structural characteristics. For example, with increasing pore depth the distance between the pore tips and hole generation area decreases. The pore tips become then more effective in collecting the photo-generated holes which leads to an increase in the total current, depending on the minority carrier diffusion length of the sample. If the backside illumination is kept constant, the increasing in the current will lead to an increase in the pore diameters in depth [78].

The thickness of a porous silicon layer is determined by the time that the current density is applied, that is the etching time. To have a thicker layer, a longer etching time is required.

3.1.2. Experimental process for p-type silicon

In this section, we describe all the elements that are a part of the fabrication system and the results obtained for p-type silicon. The obtained samples are disordered macroporous silicon. A self-controlled system created for the fabrication of porous silicon has been established at the Department of Electronic, Electric and Automatic Engineering at Rovira i Virgili University [79]. In this section, the importance of each element and its usefulness are explained.

The wafers used for the formation of macroporous silicon were p-type (boron doped) silicon wafers with orientation (100). The growth of porous silicon was realized in CZ (Czochralski grown) wafers with two different resistivities: 10-20 and 20-30 Ωcm. The resistivity of the wafer influences the macroporous structure.

Fig. 3.2 shows the digital photograph of the fabrication system. The main elements of the system are: (1) the electrochemical cell, (2) Keithley 2420 SourceMeter which applies the current during the etching, (3, 4) two multimetersto measure current and voltage, (5) LabVIEW (National Instruments) based software, which controls the applied current and the etching time, and (6) stirrer motor.

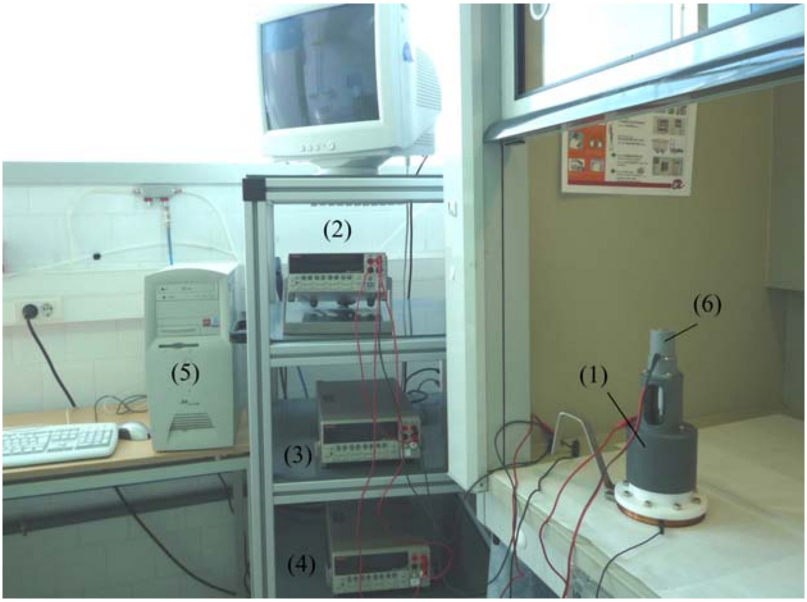

Fig. 3.2. Digital photograph of home-made electrochemical cell and the experimental set-up designed and fabricated for the formation of porous silicon using p-type wafers.

Fig. 3.3 shows the electrochemical cell which is the most important part of the fabrication system because the homogeneity of the porous silicon samples depends on its structure. Our cell was made of polytetrafluoroethylene (PTFE or Teflon), due to its resistance to HF even at high concentrations. The cell body is a cylindrical-section recipient that facilitates the renovation of the electrolyte with the stirrer. Besides, the walls of the hole at the bottom of the recipient, made for the contact of the electrolyte with the wafer, are not vertical but tilted to facilitate the renovation of the electrolyte and the removal of the hydrogen bubbles on the surface of the wafer. The volume of the cell has been adjusted to stir the lowest quantity of electrolyte possible (around 200 ml in our case).

The wafer is situated at the bottom of the cell in order to the bubbles formed on the surface are removed due to the stirrer effects and with the help of the gravity. The cell is sealed by pressing the wafer against a vinylidene fluoride-hexafluoropropylene (Viton®) O-ring. The O-ring seal defines the sample area which will be exposed to the electrolyte.

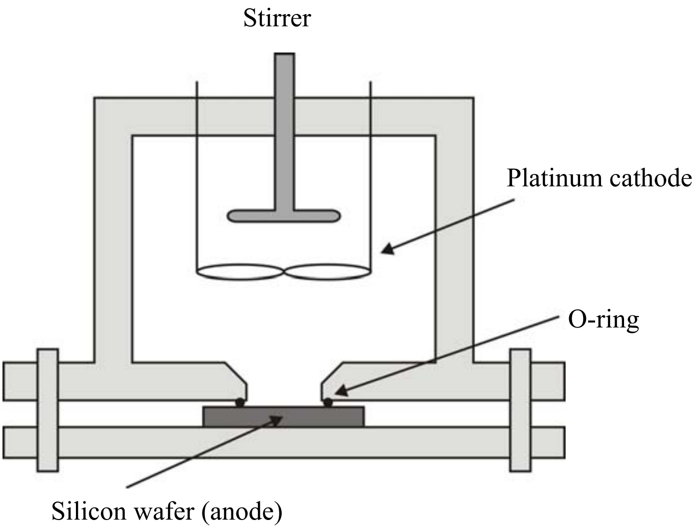

Fig. 3.3. Schematically diagram of the electrochemical cell for porous silicon fabrication.

The backside contact of the wafer is a copper disk which enables a uniform contact on the whole area of the wafer. Due to the high resistivity (low doped) of the wafers used a thin gold layer of some tens of nanometers were deposited in the back surface of the wafers in order to provide a good contact between the wafer and its back-side metallic connection (copper disk).

The stirrer is mechanic and its shape has been specially selected to stir the electrolyte from bottom to top. The stirrer rotates because of a continuous motor. The rotation velocity is selected by adjusting the voltage applied to the motor.

The process of pore growth can be realized either by controlling the anodic current or the potential. The most widely used method is the current control, because it allows a better control of thickness and reproducibility of the porous silicon. For our fabrication system we have realized current control using a Keithley 2420 SourceMeter. This source enables a perfect control of the time and current applied during the growth. Two multimeters are used for the measurement of the current and the voltage of the system during the etching process.

The electrolyte used for the fabrication of porous silicon is a solution of hydrofluoric acid (HF) and a sulfactant. Surfactants protect the sidewalls against dissolution in order to obtain deep macropores and thick and smooth pore walls. Different types of surfactants can be added, such as cetyltrimethylammonium chloride (CTAC), ethanol, dimethylsulfoxide (DMSO), dimethylformamide (DMF) or a mixture with some of them. The electrolyte that we have used for the fabrication of macroporous silicon templates is composed of high purity hydrofluoric acid (HF) in 40% aqueous solution and DMF. We have used the electrolyte in proportion 1:10 (HF:DMF). This electrolyte solution is reported in many works [80-82] and it provides smooth pore walls.

Using this solution, macroporous silicon was obtained with different etching times and current densities, as is shown in Fig. 3.4-3.5. The images obtained by Environmental scanning microscopy (ESEM) were studied using a software application for image analysis in order to obtain the dependences presented in Fig. 3.6 and 3.7 [83].

Fig. 3.6 presents the pore diameter and porosity dependence on etching time with a constant current density of 10 mA/cm^2. In Fig. 3.7, the etching rate and porosity versus the current density is presented for an etching time of 20 min.

With the concentration of the HF solution constant, the results reveal that the pore diameter obtained was about 1 μm in the conditions analysed by both 10-20 and 20-30 Ωcm silicon wafers. As Fig. 3.6 shows, the pore depth increases faster in silicon wafers of 20-30 Ωcm, which means that the higher resistivity produces higher etching rate. The same effect is shown when the current density increases (Fig. 3.7). The porosity is constant during the etching time (Fig. 3.6) whereas the porosity increases when current density increases (Fig. 3.7). Fig. 3.6-3.7 show that, in the same conditions, the macroporous silicon prepared present less porosity when the wafer used has higher resistivity [80].

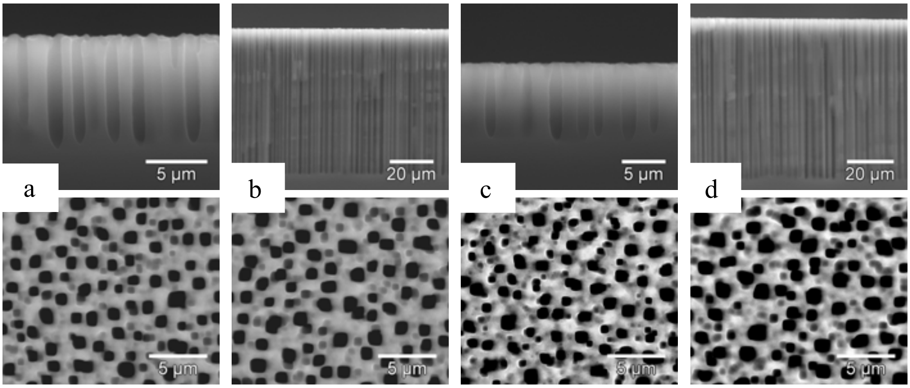

Fig. 3.4. ESEM images of (a-b) macroporous silicon from 10-20 Ωcm wafers etched at 10 mA/cm^2 for 10 and 60 min, respectively, and (c-b) macroporous silicon from 20-30 Ωcm wafers etched at 10 mA/cm^2 for 10 and 60 min, respectively.

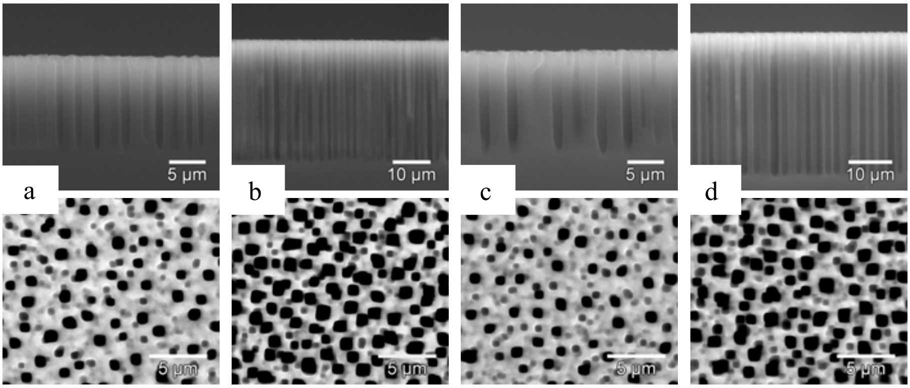

Fig. 3.5. ESEM images of (a-b) macroporous silicon from 10-20 Ωcm wafers etched for 20 min at 5 and 20 mA/cm^2, respectively, and (c-b) macroporous silicon from 20-30 Ωcm wafers etched for 20 min at 5 and 20 mA/cm^2, respectively.

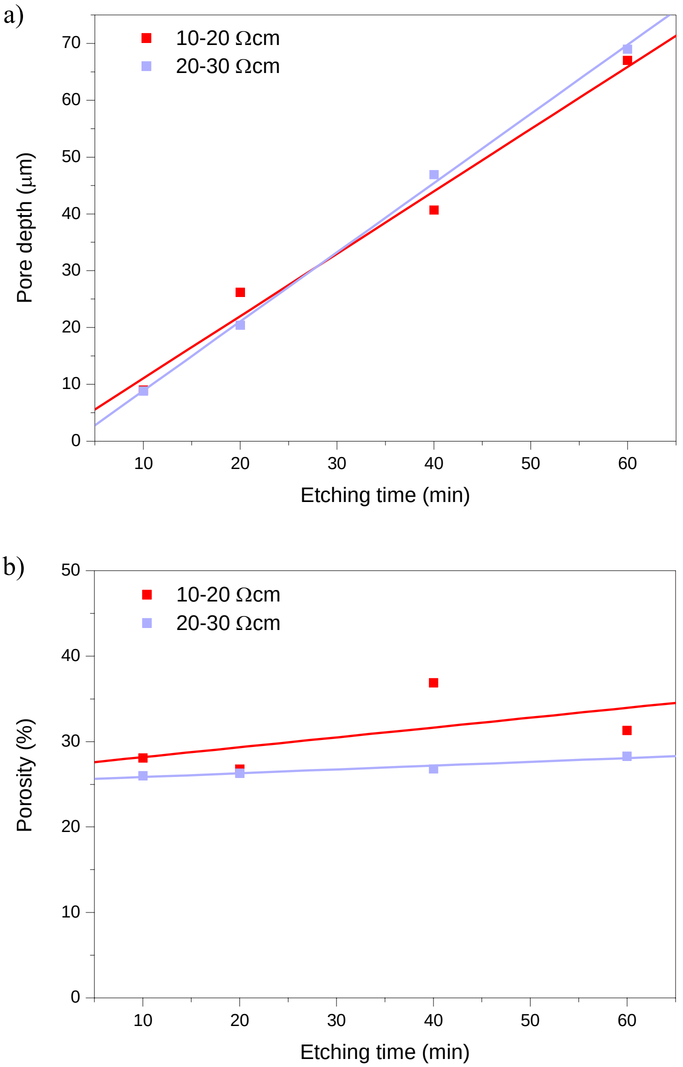

Fig. 3.6. (a) Pore depth and (b) porosity versus etching time for silicon wafers of 10-20 and 20-30 Ωcm using a current density of 10 mA/cm^2.

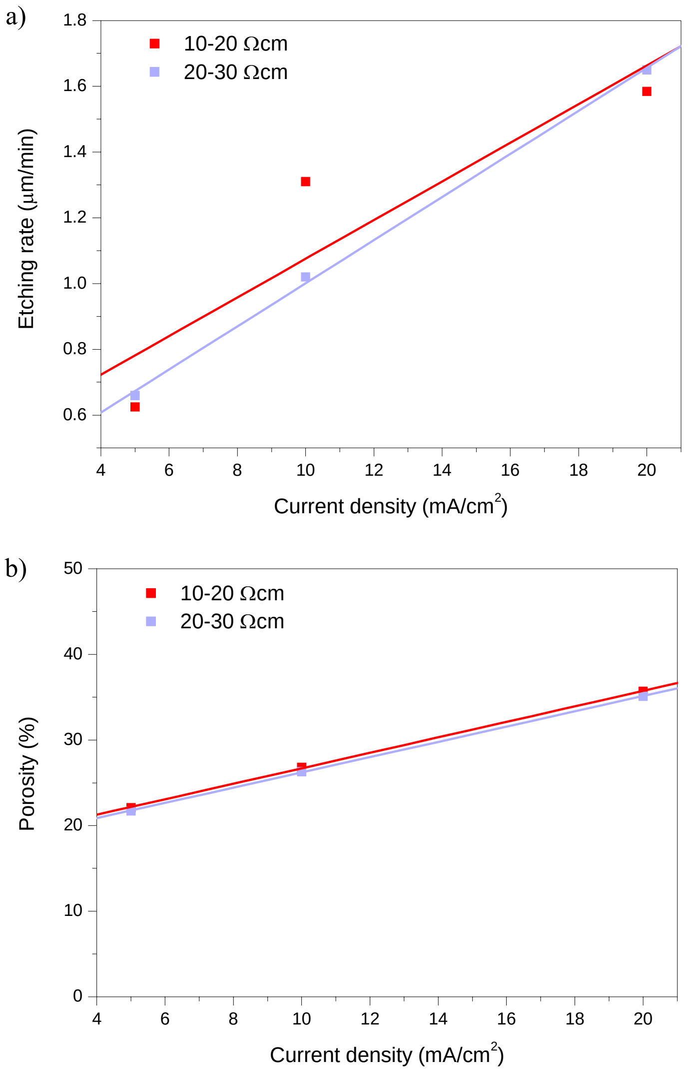

Fig. 3.7. (a) Etching rate and (b) porosity versus current density for silicon wafers of 10-20 and 20-30 Ωcm after an etching time of 20 min.

3.1.3. Experimental process for n-type silicon

This section is concerned with the description of the different experimental aspects of the etching process for n-type silicon in order to prepare ordered macroporous silicon. The electrochemical etching apparatus was elaborated in collaboration with the Group for Semiconductor Devices at Technical University of Catalonia, Barcelona. The sample preparation was realized by Dr. Trifon Trifonov using the clean room facilities of the Department of Electronics at Technical University of Catalonia [84].

The starting material was n-type (phosphorus doped) silicon wafers with orientation (100) and resistivity 1-10 Ωcm. Both CZ (Czochralski grown) and FZ (Float zone) wafers were used. It is worth mentioning that the use of FZ wafers is preferred, because of the higher minority carrier lifetime in these wafers.

Fig. 3.8 shows a digital photograph of the developed electrochemical etching set-up in operation. The etching apparatus comprises: (1) electrochemical cell, (2) circuit for nitrogen bubbling, (3) IR blocking filter, (4) 100 W halogen lamp, (5) custom-built voltage-to-voltage transformer for controlling the backside illumination circuit, (6) multimeter, (7) HP E3631A power supply, (8) MEMS potentiostat, (9) LabVIEW based software and (10) cryostat.

A schematic diagram of the electrochemical cell is shown in Fig. 3.9. The wafer as a working electrode, together with counter and reference electrodes, is incorporated in a custom-built electrochemical etching cell. The electrochemical cell is a part of specialized in-house constructed etching rig that also comprises a computer controlled backside illumination and a heat exchanger with thermostat for temperature control. The front side of the wafer (where macropores will grow) is in contact to the electrolyte, while the wafer backside is illuminated by a 100 W halogen lamp.

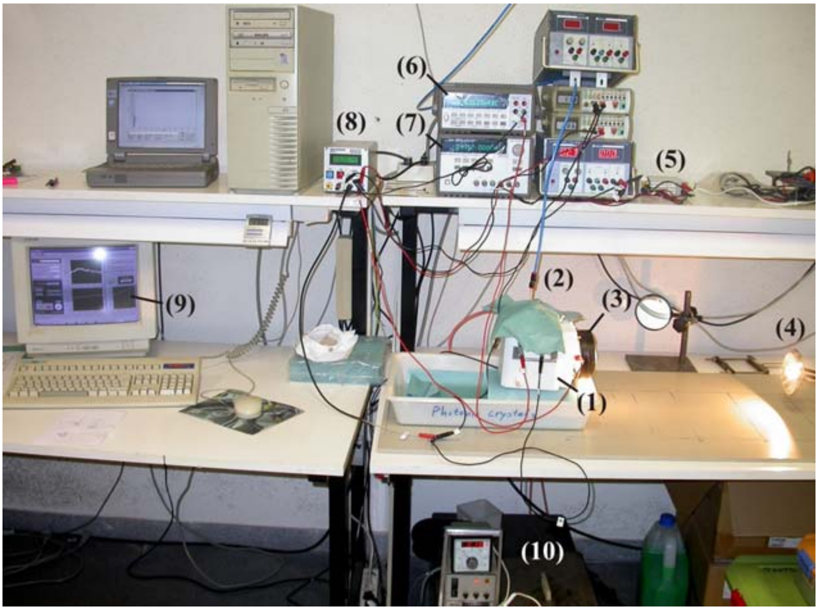

Fig. 3.8. Digital photograph of home-made electrochemical cell and the experimental set-up designed and fabricated for the formation of porous silicon using n-type wafers.

The electrochemical cell is the main part of the experimental set-up. Our cell was made of polytetrafluoroethylene (PTFE or Teflon), because it is resistant to HF even at high concentrations. The total amount of liquid that can be contained is about 800 ml, which is well enough to ensure a constant HF concentration during the etching process. The cell was prepared to support 2-inch wafers or smaller samples with dimensions of about 10×10 mm. In order to seal the cell, the wafer is mechanically pressed by screws against a vinylidene fluoride-hexafluoropropylene (Viton®) O-ring. The O-ring seal defines the sample area which will be exposed to the electrolyte. A standard three-electrode configuration for the electrochemical cell was used: working (the wafer), reference and counter electrodes. The reference and counter electrodes are made of platinum Pt because it is chemically inert in HF. The counter electrode was coiled in order to increase its surface immersed in the electrolyte, while the reference electrode was a simple wire positioned close (about 3 µm) to the wafer. The reference electrode is needed to discount the voltage drop across the electrolyte and the voltage offset introduced by the counter electrode, because these are of no importance in the etching process.

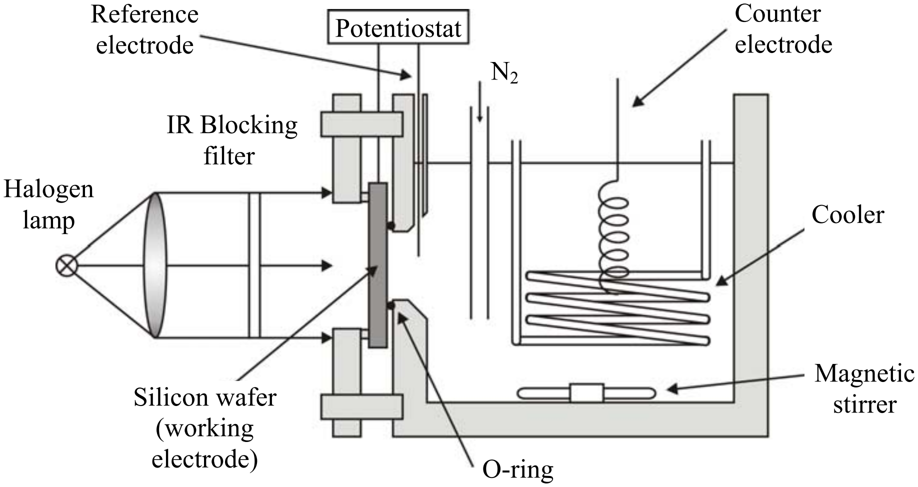

Fig. 3.9. Schematically diagram of the set-up for porous silicon fabrication. The etching cell uses three-electrode configuration: working (wafer), platinum reference and counter electrodes. The wafer backside is illuminated through a 100 W computer-regulated halogen lamp, coupled to an IR cut-off filter.

To achieve a stable pore grow the minority carriers should be generated deep within the bulk or near the backside surface of the wafer. The electronic holes must diffuse through the wafer in order to be focused at the tips of the pores. This imposes special restrictions to the spectral characteristics of the lamp used for the backside illumination. The infrared emission of the used halogen lamp must be blocked, which is achieved by an IR cut-off filter (SIR dielectric heat reflecting mirror, Präzisions Glas & Optik GmbH). The backside illumination intensity is regulated via a computer-controlled power supply (HP E3631A, Agilent Technology). A multimeter connected to a computer is used to measure and record the total current going through the system. The wafer (working electrode) is positively biased through an AMMT (Advanced Micromachining Tools GmbH) MEMS potentiostat, which is also controlled by a computer. A cryostat (Heto, Denmark) was used to establish and maintain a desired constant temperature of the electrolyte during the etching. The electrolyte is continuously stirred by a simple Teflon-covered magnetic stirrer.

To obtain ordered pores, the sample preparation procedure proposed by Lehmann [85, 86] in his first works is adopted, although some modifications were made. The simplified process sequence is given in Fig. 3.10. First, the wafers were oxidized in dry O_2 at 1100 °C for 20-25 min, in order to grow a thin oxide film (Fig. 3.10a). The oxide film only serves as a mask and as a protective layer in the subsequent anisotropic etch of silicon in tetramethyl ammonium hydroxide (TMAH) solution. The oxidation step cannot be avoided because the normal resists used in the lithography are easily dissolved by TMAH.

A standard photolithography, which consisted of resist spinning, soft baking, exposition, developing and hard baking of the resist, was used to pattern the oxide layer (Fig. 3.10b). A positive photoresist HPR504 with a developer HPRD (Arch Chemicals Inc.), and a Karl Suss MA4 mask aligner were used for the photolithography. This step determines the arrangement and period of the resulting pore lattice. It is clear, that if we want to downscale the lattice period below micrometer we should use a high-resolution lithography. The lithographic pattern was then transferred into the oxide layer by etching the silicon oxide in buffered hydrofluoric acid (BHF) (Fig. 3.10c). The used BHF etching mixture (Ammonium fluoride etching mixture HF (6%) and NH_4F (35%), Honeywell Specialty Chemicals Seelze GmbH) has an etching rate of about 680 Å/min. Therefore, a few seconds are needed to etch the oxide which can result in an over-etching if very thin oxide layers are used.

Next, the silicon wafers were immersed in 8% TMAH solutions at 80°C temperature for 7-9 min, in order to make the defect sites onto the wafer surface (Fig. 3.10d). The TMAH etch is an anisotropic process; the resulting structure is a lattice of pyramidal notches that will serve as seeds for the pore growth. It should be noted that the dimensions of these inverted pyramids do not determine the diameter of the pores. The pore diameter is mainly dependent on the applied etching current and to some extent on the wafer resistivity. The pyramids affect neither the pore shape. The pyramids determine only the positions of the pores and thus, the lattice constant of the resulting pore structure. After the TMAH etch, the oxide layer is no longer needed. It was removed in a solution of HF 5%.

The second main step of the sample preparation is the formation of an ohmic contact on the wafer backside (Fig. 3.10e). The Indium Tin Oxide (ITO) layers were deposited by means of an rf-magnetron sputtering system (Edwards ESM100). The ITO sputtering was performed under the following conditions: ITO 99.99% purity target with a diameter 100 mm, 50 mm target-substrate distance, Ar plasma with pressure 0.5 Pa, 50 W forward power, 12 min deposition time at room temperature. The ITO film is transparent to the light and has good conductance properties.

This process could be also employed with p-type silicon in order to obtain ordered pores [82].

Finally, the patterned silicon wafer was electrochemically etched. The electrolyte was prepared by diluting 50 wt.% HF in deionized water up to a desired concentration. Some of the experiments were performed with the addition of surfactants to the electrolyte. A surfactant is usually used as a wetting agent. It reduces the surface tension and thus, the sticking probability of the hydrogen bubbles.

Macroporous membranes can be produced by etching the backside of the sample in TMAH solution.

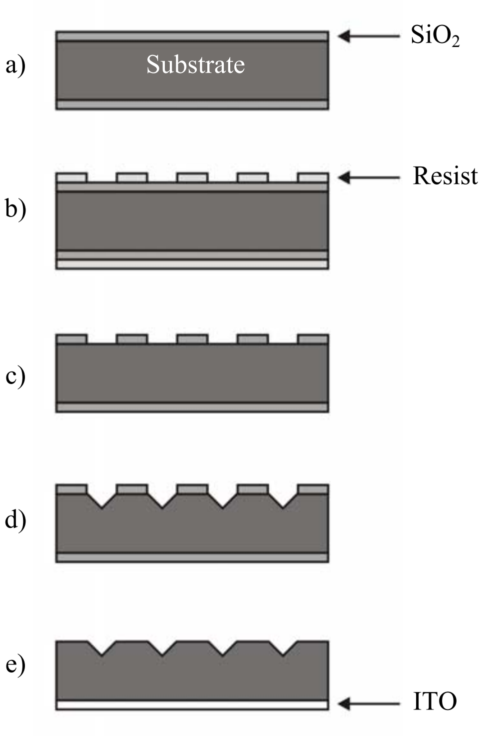

Fig. 3.10. Main process sequence for sample preparation in order to obtain ordered macroporous silicon. (a) Wafer oxidation, (b) photolithography, (c) window opening in the oxide film by BHF etch, (d) TMAH etch of the silicon to form pyramidal notches and (e) ITO sputtering deposition.

3.1.4. Macroporous silicon templates

Disordered macroporous silicon was obtained using p-type silicon in order to be used as template. Fig. 3.11a-b show macroporous silicon prepared from a silicon wafer of 10-20 Ωcm etched at 2 mA/cm^2 for 20 min. Other sample, employed as template, was a silicon wafer of 20-30 Ωcm etched at 10 mA/cm^2 for 20 min, which is shown in Fig. 3.11c-d. Macroporous silicon used as template had at the most 20 μm of pore depth, but deeper macroporous silicon can be prepared, as is shown in Fig. 3.12, using a silicon wafer of 20-30 Ωcm etched at 10 mA/cm^2 for 60 min.

The disordered macropores obtained present dispersion in pore diameter and depth which produces an inhomogeneous template.

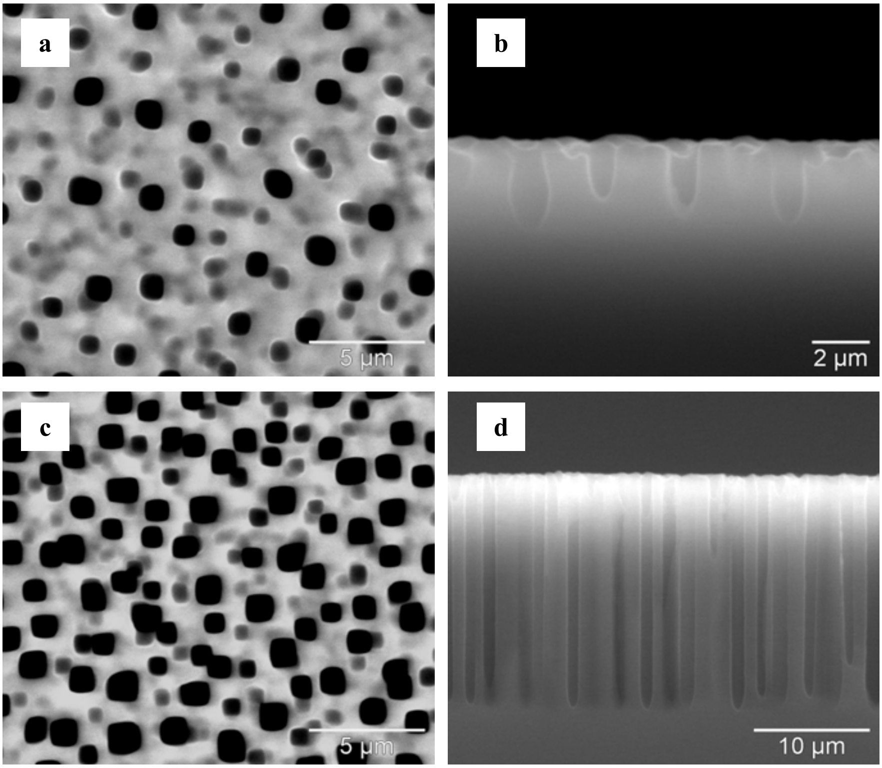

Fig. 3.11. ESEM images of disordered macroporous silicon with about 1 μm of pore diameter and (a-b) about 2 μm and (c-d) 20 μm of pore depth.

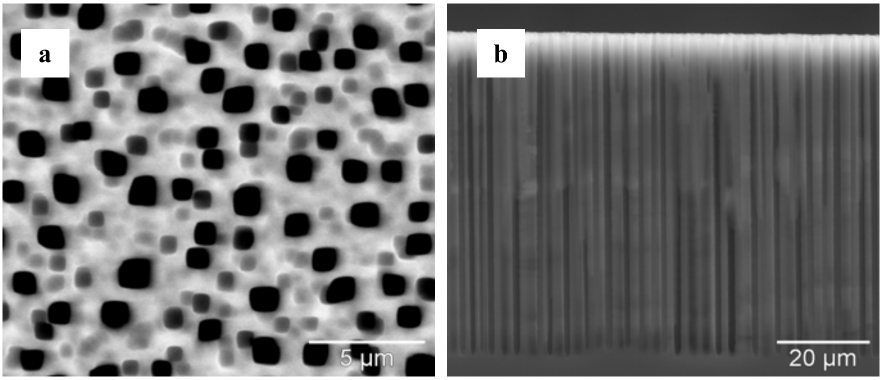

Fig. 3.12. ESEM images of disordered macroporous silicon with 1 µm of pore diameter and about 70 µm of pore depth.

The ordered templates open only at one end were prepared from n-type silicon wafers that were patterned using the process explained before. Fig. 3.13 shows ordered macroporous silicon with a pore diameter determined by the pattern and from 7.5 to 22 µm of pore depth. As well, macroporous silicon membranes were employed with 2 µm of pore diameter and from 40 to 150 µm of pore depth. Some examples of macroporous silicon membranes can be observed in Fig. 3.14. The dimensions of ordered macroporous silicon are homogeneous and the diameter is determined by the pattern of the silicon wafer.

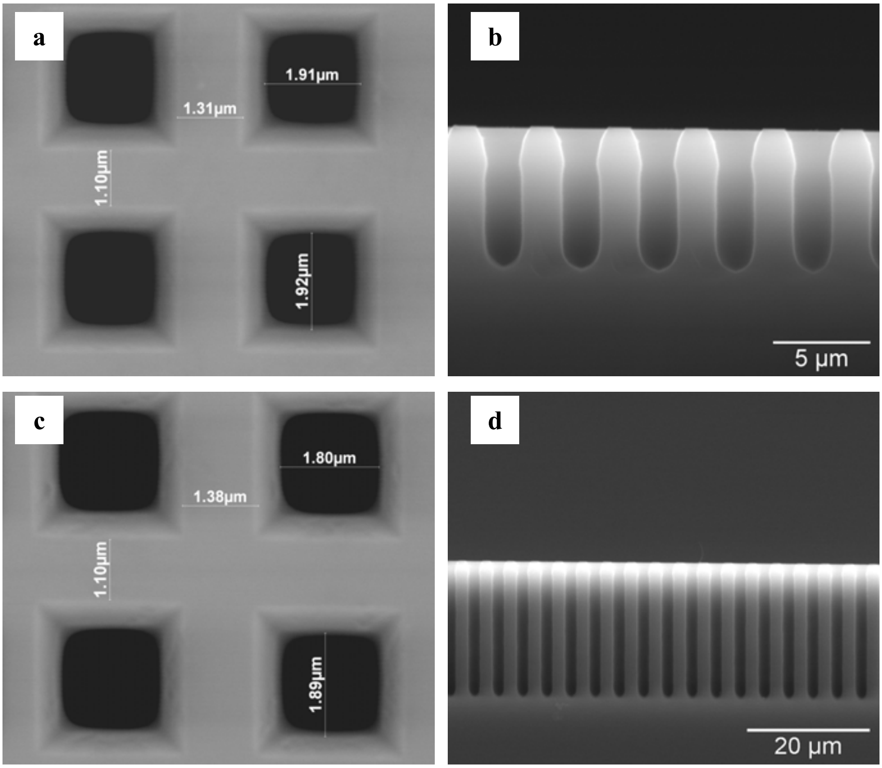

Fig. 3.13. ESEM images of ordered macroporous silicon with 1.9 µm of pore diameter and (a-b) 7.5 µm and (c-d) 22 µm of pore depth.

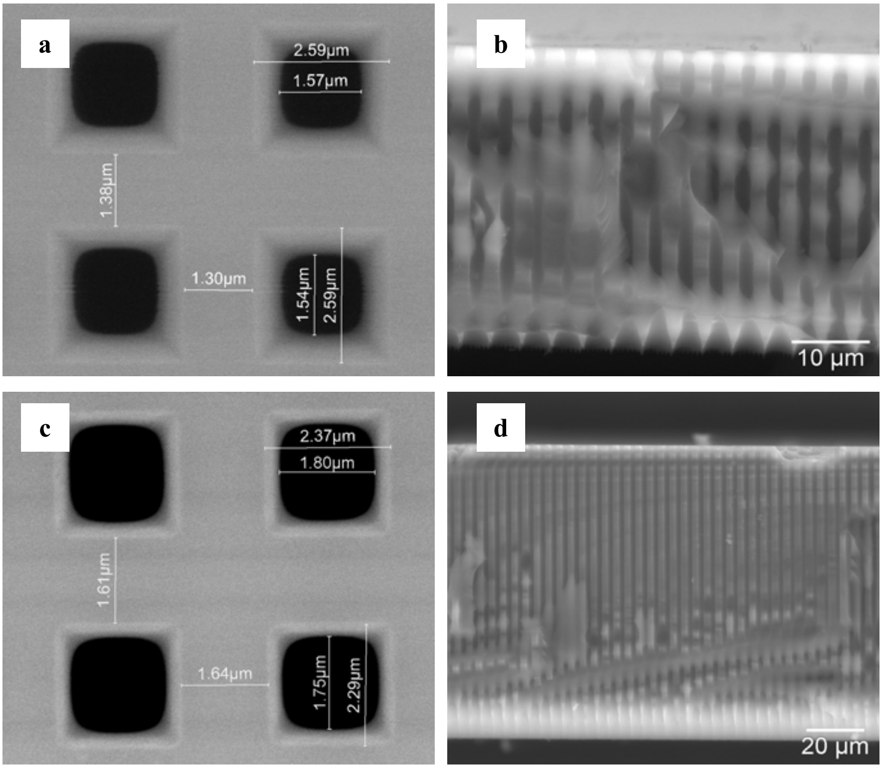

Fig. 3.14. ESEM images of ordered macroporous silicon membranes with (a-b) 40 µm and (c-d) 100 µm of pore depth.

3.2. Self-ordered nanoporous alumina

The anodizing of metals in the industrial area has its origins back in early 1920’s. Thanks to Bengough Stuart anodizing process patented in 1923 and lately in 1927 Gower and O’Brien process, the industrial anodizing can be still widely used for many commercial purposes such as metal passivation or decorative.

The most common anodized metal is aluminium and we can notice its presence everywhere in many things. The anodized aluminium has high corrosion resistance, surface hardness and good ability for colouring [87].

A breakthrough in porous alumina science has become in 1995. That time, Masuda and Fukuda have discovered two-step replication process for fabrication of self-ordered porous alumina structure with highly ordered pores [28]. This essential work has served as fundamental recipe for the following investigation in this field. In addition, it is also one the most cited reference between porous alumina scientific communities.

In order to prepare porous alumina, the oxidized metal anode and inert cathode made of carbon or platinum must be immersed in the electrolyte (acid solution). Both electrodes are connected to power supply, positive pole to anode and negative pole to cathode. During the electrolysis, the redox (reduction/oxidation) reactions are simultaneously in progress on the electrodes. The anode is oxidized by negative electrolyte substances (anions) resulting in the formation of anodic oxide layer on the metal surface. On the other side, the negative cathode supplied with electrons serves to reduce positive substances (cations). Therefore, the redox reactions are characterized by a balance of electron production and consumption.

The electrolyte is an important medium in the anodizing process and it has an essential influence on the property of the final anodic oxide layer. Porous anodic film is produced in slightly soluble, acidic aqueous electrolytes such as sulphuric, oxalic, phosphoric or chromic acid [88].

3.2.1. Chemistry of nanoporous alumina formation

When a metal such as tantalum, zirconium or aluminium is exposed to ambient conditions, the metal surface is covered with a very thin natural oxide film called barrier oxide. Similar reaction occurs also when the metal is employed as anode in the electrochemical system for electrolysis. Compared to the environment, the oxidizing conditions in this case are highly enhanced by means of electrical current and electrolyte. Particularly, the oxidizing process that takes place on the anode surface is called anodizing.

In an idealised model of formation of porous type aluminium oxide, so called porous alumina, the complex of chemical reactions occurs during aluminium anodization proceeds in the electrolyte/oxide (e/o) and oxide/aluminium (o/a) interfaces at the pore tip [89, 90]. The pore growth in the oxide layer is assigned to the equilibrium between the alumina formation at o/a interface and alumina dissolution at e/o interface. Written in the terms of their chemical reactions the oxide formation process can be formulated as follows:

$$2Al(s) + 3O^{-2} = Al_2O_3(s) + 6e^- \qquad \text{(eq. 3.2)}$$

According to (eq. 3.2), the oxygen anions penetrate through the e/o interface to the o/a interface, where they react with aluminium forming oxide layer and some free electrons. Conversely, the cations of aluminium that are withdrawn from the metal bulk under electric field move towards the e/o interface where they are either injected directly to the electrolyte or they also contribute to the oxide formation in the reaction with water. This reaction can be described as follows:

$$2Al^{+3}(aq) + 3H_2O \leftrightarrow Al_2O_3(s) + 6H^+(aq) \qquad \text{(eq. 3.3)}$$

Reversibly, the oxide dissolution continuously takes place at the e/o interface, where protons of H^+ cause alumina decomposition loosing aluminium cations and forming water. Accordingly to (eq. 3.3), it can be assumed that the e/o and o/a interfaces at the pore tips are in constant motion during the anodization process.

The result of (eq. 3.3) is enhancement of oxide layer and production of hydrogen cations that starts to migrate towards the negative electrode.

Simultaneously, on the cathode there is continuous reduction of these hydrogen cations in the reaction with free electrons carried through the electrical circuit from the anode. The formed hydrogen molecules are led away from the electrolyte in the form of bubbles. The previous description of aluminium anodization was intentionally simplified and only basic explanation with principal chemical equations was given. In fact there is a complex of electrochemical processes and reactions involved in the formation process of porous alumina which can be find with description in more detail elsewhere [90-92].

The porous alumina obtained has a geometry and consistency that strongly depends on the anodizing conditions, such as electrolyte, pH, anodizing time, temperature, power supply, and the pre-treatment of the aluminium foils.

The interpore distance has a linear dependence on the applied voltage. As well, the thickness of porous alumina can be obtained by checking the applied voltage and the anodizing time. Generally, low temperatures lead to slower pore growth rates than if ambient conditions are used. The steady current flow always starts to slightly decrease during a long anodizing time and therefore also a variance of pore growth rate should be expected. Porous alumina structures with a broad range of aspect ratios (pore depth/pore diameter) varying from few hundreds to several thousands are feasible using corresponding anodizing parameters.

The electrolyte conditions including acid type, temperature, concentration and pH are all together important parameter that has to be controlled in order to ensure the formation of well-ordered alumina. The use of acid type with a given concentration is somewhat restricted by means of applied voltages values. For example, if the anodization is carried out in the high conductive sulphuric acid solution (10 wt.%), then the low voltages (below 25 V) must be applied. For oxalic acid and phosphoric acid solutions usually moderate voltages in the range of 40 to 60 V and high voltages up to 195 V are applied, respectively.

The temperature stability during the anodization can be provided by vigorous stirring of the electrolyte with external unit for temperature control.

Another necessary condition for the formation of ordered pore arrays is the annealing of the aluminium foils prior to anodizing in order to enhance the grain size and remove the mechanical stress in the metal substrate. The self-ordering process in the non-annealed aluminium substrates can be disturbed by a large number of grain boundaries [89, 93]. Since the well-ordered alumina structure can be obtained only when the pores start to grow from a very smooth and clean aluminium surface, the electrochemical-polishing is necessary before anodizing.

3.2.2. Experimental process

The experimental fabrication process and the detailed characterization of porous alumina structures will be described in this section. The two-step anodization process used takes an advantage of self-ordering phenomenon. A self-controlled system created for the fabrication of porous alumina has been established at the Department of Electronic, Electric and Automatic Engineering at Rovira i Virgili University [94].

A digital photograph of the fabrication system is shown in Fig. 3.15. This system comprises: (1) the electrochemical cell, (2) power supply (Delta Elektronika), (3, 4) two multimeters to measure actual current at voltage, (5) LabVIEW based software, (6) stirrer motor and (7) temperature controller (Polyscience).

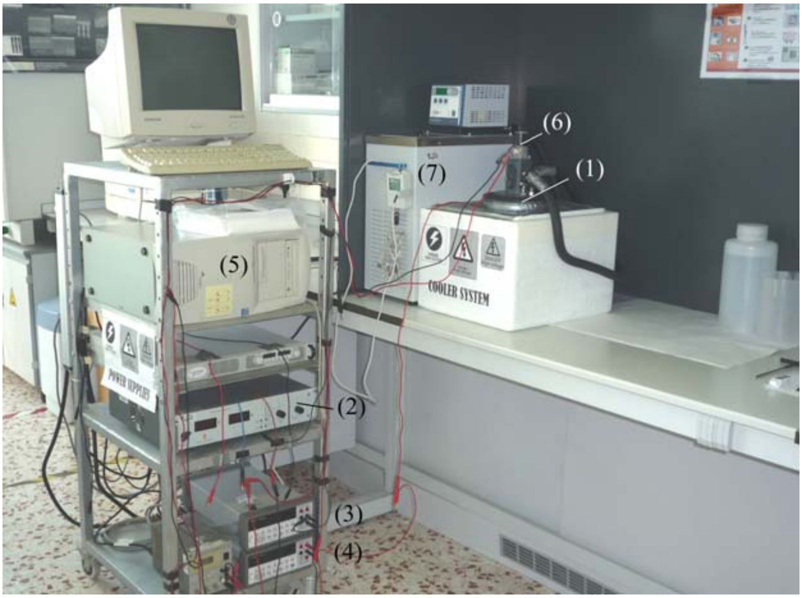

Fig. 3.15. Digital photograph of home-made electrochemical cell and the experimental set-up designed and fabricated for the formation of porous alumina.

In the Fig. 3.16 is a schematic of the developed anodizing system. The anodizing cell is a cylindrical Teflon tank with the sample holder at the bottom. The tank is screwed down to the copper plate and in this way the sample is always sealed with O-ring between the tank and plate. The complete cell stands on the Peltier coolant plate that makes a refrigerating circuit together with a stainless coil. The coolant stainless coil ensures the internal temperature control of electrolyte.

The plastic cell cover has implemented the Teflon propeller driven by a motor to provide the electrolyte stirring, and a platinum wire wounded to a Teflon bar that serves as cathode.

Two multimeters measure the actual value of current and voltage variables.

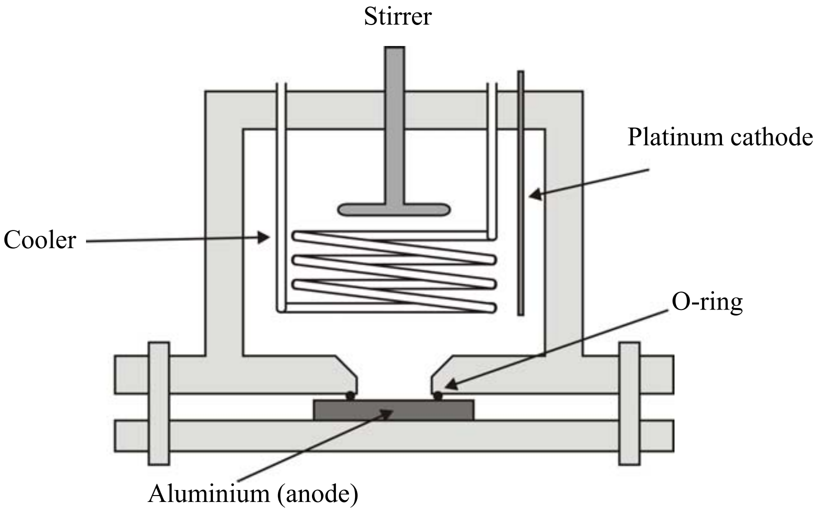

Fig. 3.16. Schematically diagram of the home-made anodizing cell for porous alumina fabrication.

The annealing and electro polishing processes are inherent pre anodizing treatments of aluminium foils in order to obtain porous alumina with satisfactory geometrical properties.

First, an ultra pure (99.999 %) aluminium foils (Goodfellow) with thickness of 250 µm were thoroughly cleaned in the ultrasonic bath with acetone and then rinsed in deionised water. Then, the dried foils were put in the annealing furnace with a nitrogen inlet to avoid the oxidation process at high temperatures. The annealing temperature was controlled by a programmable profile, where the final annealing temperature was usually preset just below the aluminium melting point (660 ºC) in the range of 400-500 ºC with slowly increasing initial ramp of 10 ºC/min. Once the heat treatment was completed, the 5 cm^2 foils were equally cut into desired dimensions.

The annealed aluminium sheets were employed as anode in the electro-polishing system with 0.5 l double wall coolant vessel filled ethanol mixture of perchloric acid (4:1) [89, 93, 95, 96]. The mixture temperature must be kept below 5 ºC and one has to follow working precautions due to the explosiveness of perchloric acid. In order to achieve a good electro-polishing effect on the aluminium surface, the current density should be over 100 mA/cm^2 during the process [97-99]. In this work, the applied constant voltage of 20 V turned out to be sufficient for obtaining a proper polishing current. Also a vigorous electrolyte stirring is necessary to remove bubbles and heat formation on the aluminium surface produced by a high rate of electrochemical reactions. After electro polishing period of 2 minutes, the aluminium foils were rinsed in deionised water and dried with air flow.

In 1995, Masuda and Fukuda have reported on a novel technique for aluminium anodization in two steps that is based on naturally occurring phenomenon of pore self-ordering [28]. Since then, the self-ordered nanoporous alumina has attracted a great interest among the scientists all over the world. This technically modest and relatively low cost fabrication process was also used in this work.

Fig. 3.17 illustrates the step-by-step experimental preparation of porous alumina based on two-step anodization. In this figure, each fabrication step is represented by a schematic drawing. In the next phase, the ready polished aluminium samples were mounted in the electrochemical cell that is filled with one of the electrolyte types prepared from sulphuric (H_2SO_4), oxalic ($(COOH)_2$) or phosphoric (H_3PO_4) acid. The first anodization step (c) was conducted under an appropriate voltage in the potenciostatic mode. The applied voltage is highly electrolyte dependent and usually low voltages in the range of 20-25 V are used with high conductive 10 wt.% H_2SO_4, medium voltages between 40 V and 60 V are applied for 0.3 M $(COOH)_2$, high voltages of 160- 180 V are used for 0.3 M H_3PO_4 electrolyte (21). After the first step, the porous alumina grown on the aluminium surface was removed by a wet chemical etching (d) in a mixture of 0.4 M phosphoric acid and 0.2 M chromic acid (1:1 volume ratio) at 60-80 ºC

[100, 101]. The second anodization step (e) is performed under the same experimental conditions as they were used in the first step in order to obtain ordered porous alumina. The structure obtained by this process consists in a well-ordered matrix of hexagonal cells with a central pore, but ordered pores are arranged in several domains with uneven shapes and areas.

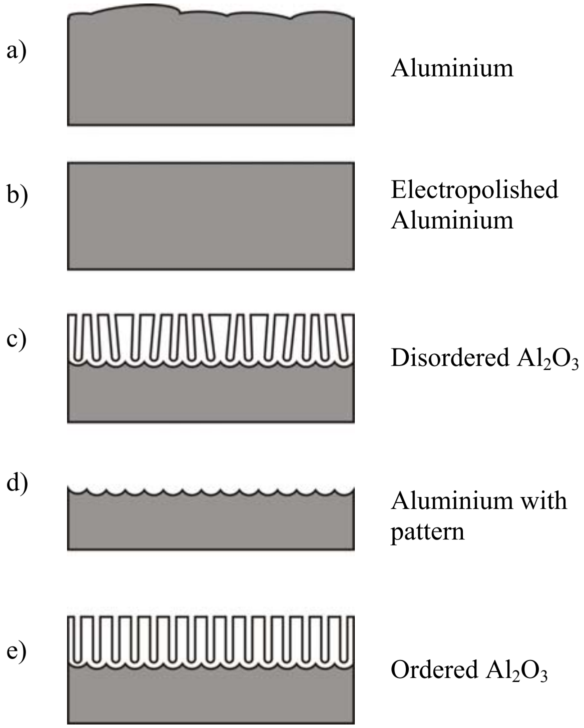

Fig. 3.17. A scheme of step-by-step fabrication process of porous alumina based on two-step anodization.

The pore diameter of the as-made porous alumina can be easily tuned to desired dimensions using a simple wet chemical etching, so-called pore widening, in 5 wt.% H_3PO_4 at 30-40 ºC [102]. Fig. 3.18 summarized the ESEM results of the experimental set that was carried out in order to study the pore widening effect on the pore diameter. The as-made samples were produced using standard conditions for sulphuric acid, oxalic acid and phosphoric acid with the applied voltage: 20, 40 and 170 V, respectively. The anodizing period in the second step for all the samples was 3 hours that gives the final alumina thickness of approximately 30 μm. After the primary ESEM analysis of the as-made samples, the samples were etched in two successive pore widening steps using 5 wt.% H_3PO_4 at 35 ºC. The etching time of each step for sample prepared in sulphuric acid, oxalic acid and phosphoric acid was 5, 10 and 20 min, respectively. Between the etching steps ESEM analysis was carried out for all the samples in order to study the pore widening effect.

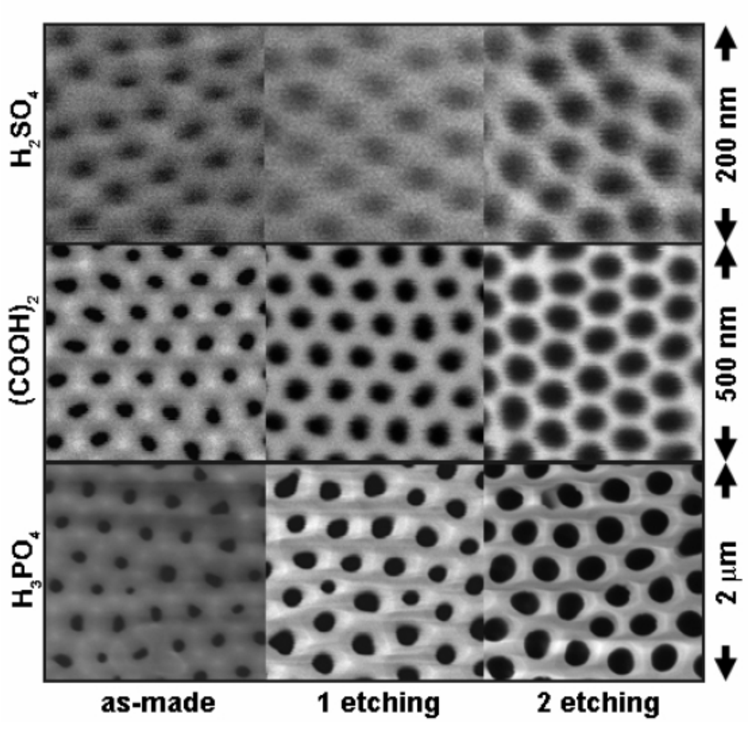

Fig. 3.18. The acid solution and pore widening effect represented by ESEM top surface insets of porous alumina samples obtained. The as-made samples in the first column were etched in two consecutive cycles (1 and 2 etching) in 5 wt.% H_3PO_4 at 30 ºC for 5 min (H_2SO_4), 10 min ($(COOH)_2$) and 20 min (H_3PO_4) as shown in second and third column [94].

3.2.3. Nanoporous alumina templates

Ordered nanoporous alumina with different dimensions was prepared in order to be used as template. An example of the domains of hexagonal arrays of pores obtained is shown in Fig. 3.19a prepared in oxalic acid at 50 V, which is compared with Fig. 3.19b prepared in phosphoric acid at 160 V. The alumina prepared in oxalic acid was anodizated for 2 h with a second step of 1 min and a pore widening of 8 min at 30 ºC. The sample prepared in phosphoric acid was anodizated for 30 min with a second anodization of 5 min and a pore widening of 30 min at 30 ºC. The different interpore distance is mainly due to the acid selected and the applied voltage. Templates obtained using oxalic acid presents pores with pore diameter from 50 to 80 nm, depending of the pore widening time. In templates prepared in phosphoric acid, nanopores with pore diameter between 200 to 300 nm were obtained.

Fig. 3.20 shows two templates with different pore dept employed in the following chapters. Both samples were prepared in phosphoric acid at 160 V for 30 min, then the second step was at 160 V for 5 min (Fig. 3.20a-b) and 2 min and 30 s (Fig. 3.20c-d) with a final pore widening of 30 min at 35 ºC.

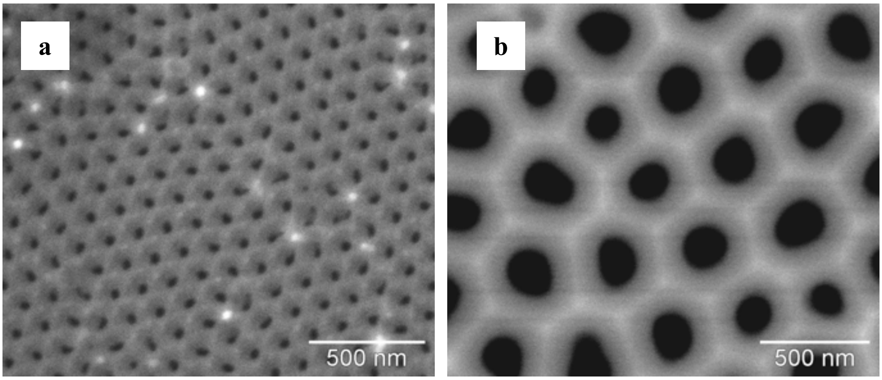

Fig. 3.19. ESEM images of self-ordered nanoporous alumina prepared (a) in oxalic acid at 50 V, with 55 nm of pore diameter, and (b) in phosphoric acid at 160 V, with 250 nm of pore diameter.

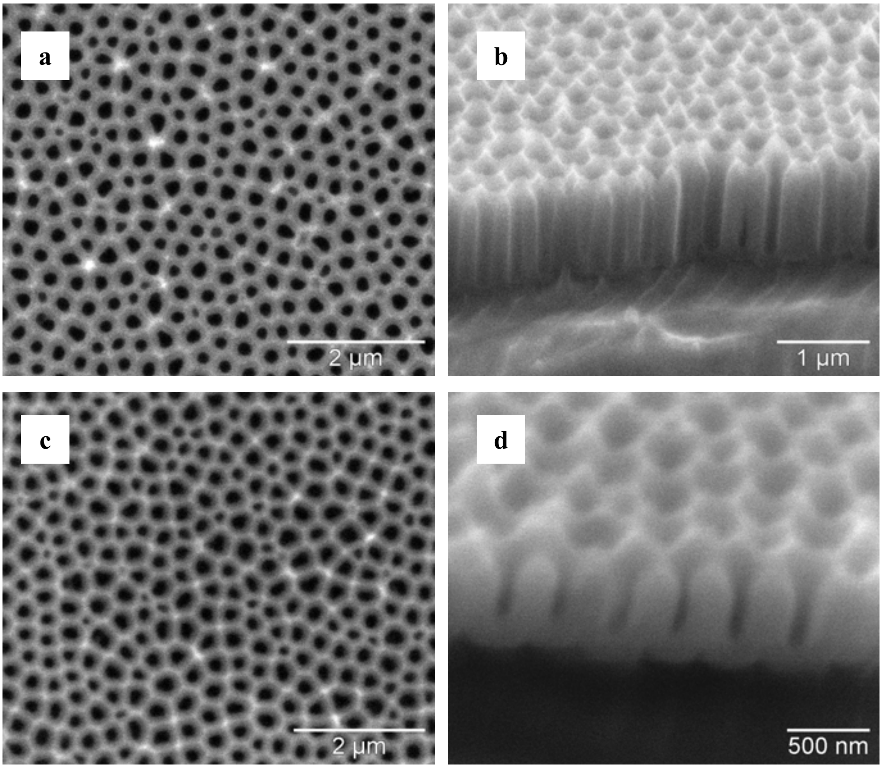

Fig. 3.20. ESEM images of self-ordered nanoporous alumina prepared in phosphoric acid at 160 V.

3.3. Conclusions

In this chapter, we have demonstrated that porous materials of different dimensions, disordered or ordered, in a large scale can be prepared. The desired pore diameter and depth can be adjusted by the experimental processes presented in the micrometer scale for silicon and in the nanometer scale for alumina.

The ordered macroporous silicon entails the pattern of the silicon surface before the electrochemical etching in HF solution, whereas the ordered alumina in hexagonal array is obtained by two-step anodization in acid solution. These processes produce porous structures with high homogeneity in depth. Disordered macroporous silicon has a high dispersion in diameter and depth due to the pore growth starts randomly.

These experimental processes were performed to prepare the porous templates employed in the following chapters. In general, in this thesis macroporous silicon with pore depth from 2 to 150 μm and pore diameter from 1 to 2 μm were employed as template. Self-ordered nanoporous alumina templates, prepared using oxalic or phosphoric acid, were obtained with pore depth from 150 nm to 3 μm and pore diameter from 55 to 250 nm. The suitable template dimensions depend on polymer used and the application developed.

Chapter 4

Preparation of polymer micro- and nanostructures

In this chapter, the preparation of 1D polymer micro- and nanostructures is presented. These polymer structures have attracted and increasing interest due to their properties which can be tuned for potential applications in many fields [31, 32, 58-60, 67-71]. They can be generally classified in two large families depending on the aspect ratio (length/diameter): fibres and tubes with high aspect ratio, and pillars of lower aspect ratio. Depending on the aspect ratio, these structures are susceptible to deformation by adhesive and capillary surface forces, particularly those made from soft polymers. In these cases the structures appear aggregated [103].

Several strategies have been developed in order to prepare polymer structures. One of the most successful fabrication methods is the template-assisted technique [14, 17, 20, 21]. This technique has the advantage of being able to create large areas and arrays of structures with control over structural parameters. As well, it is applicable to a wide range of products, such as polymers, metals and semiconductors, and using solution-based or molten material it does not required specialized equipment. By this technique, the experimental process depends on the polymer involved and the desired structure, as is shown below.

In order to develop some applications, the structures prepared must be fabricated with the suitable shape, dimensions and periodicity. Macroporous silicon is an attractive candidate as macro-template because it can be fabricated with high precision and uniformity in a large scale and because the porosity and average pore size and pore depth can be tuned by adjusting the electrochemical preparation conditions. As well, self-ordered nanoporous alumina has become one of the most common nano-templates for the preparation of different nanometer-sized structures. Under appropriate anodization conditions, long-range-ordered porous alumina with an ideally uniform arrangement of nanopores in a hexagonal array can be obtained.

As templates, macroporous silicon membranes and closed-end-pore silicon were selected to prepare microstructures, and self-ordered nanoporous alumina to obtain nanostructures. Porous silicon was fabricated as was explained in section 3.1, using n-type silicon to obtain ordered macropores and p-type silicon for disordered macropores. Nanoporous alumina template was prepared by two-step anodization process of aluminium metal in an acidic solution, as was explained in section 3.2.

In this work, we have selected different experimental processes which were developed in order to prepare structures of different aspect ratio with interesting polymers from various chemical families well known for applications in a wide range of fields [104].

The first experimental method, in order to prepare micro- and nanostructures, was the infiltration of a polymer solution into the template under vacuum. For this process, PMMA was selected as acrylic polymer. Due to its versatility, this polymer has been used in a wide range of fields and applications.

The experimental process, which involves the wetting of the template by a polymer without solvent, was also developed. PDMS was selected because it can be cured by heating and, then, a solvent is not required. Moreover, it is a soft model which is issued in a variety of products, partly because of its unique properties but also it is a relatively cheap material.

Furthermore, one-dimensional structures fabricated from conjugated polymers have attracted increasing interest due to their potential applications for various kinds of functional devices. The electrical conductance of conjugated polymers depends on the doping level and the molecular structure, which can be modified by synthesis method. For these polymers, three infiltration processes were developed: by melting-based infiltration, wetting-based method and spin-coating process. The study of the structures obtained from each method were performed due to the interest of the potential applications due to their optical and electrical properties

In this chapter, the infiltration of conjugated polymer from polyfluorenes (PFO, F8BT and F8T2), PPV derivatives (MDMO-PPV) and polythiophenes (P3HT) is studied.

After the infiltration process, in order to obtain the polymer structures, the template removal was carried out. Silicon templates were removed by an immersion into 40 wt.% KOH (aq) at 40 °C. When porous alumina was used as template, samples were immersed into a solution containing 6.8 g of copper (II) chloride ($CuCl_2$), 200 ml of 37% hydrochloric acid (HCl) and 200 ml of deionised water, in order to remove the remaining aluminium. Nanostructures were obtained by the selective dissolution of the alumina template in a 1 M sodium hydroxide (NaOH) aqueous solution at room temperature for 10-30 min.

All samples were inspected by environmental scanning electron microscopy (ESEM), at low vacuum, in order to characterize morphologically the samples. A gold thin layer was deposited on polymer nanostructures in order to avoid deformations upon heating during ESEM observation. In the ESEM images structures might appear shorter than they are due to the tilt of the samples. More detailed information about ESEM is presented in Appendix A.

4.1. Materials

Silicon wafers were purchased from WRS Materials. High purity 99.999% aluminium foils was obtained from Goodfellow Cambrigde Ltd. All the solvents used (toluene, tetrahydrofurane, chloroform and chlorobenzene) were purchased by Sigma-Aldrich.

Poly(dimethylsiloxane) (PDMS) was obtained from Sylgard 184, Dow Corning. Poly(methyl)methacrylate (PMMA, M_w = 120,000), poly(9,9-dioctylfluorene) (PFO, M_n = 15,834), poly(9,9-di-n-octylfluorene-alt-benzothiadiazole) (F8BT, M_n = 5,000-8,000), poly[(9,9-dioctylfluorenyl-2,7-diyl)-co-bithiophene] (F8T2, M_n > 20,000) and poly(2-methoxy-5-(3’,7’-dimethyloctyloxy)-1,4-phenylenevinylene) (MDMO-PPV, M_n ~ 23,000) were purchased from Sigma-Aldrich. Poly(3-hexylthiophene-2,5-diyl) (P3HT) was obtained from Sigma-Aldrich (M_n = 15,000-45,000) and Rieke Metals (M_w = 50,000). Fig. 4.1 shows the chemical structure of these polymers.

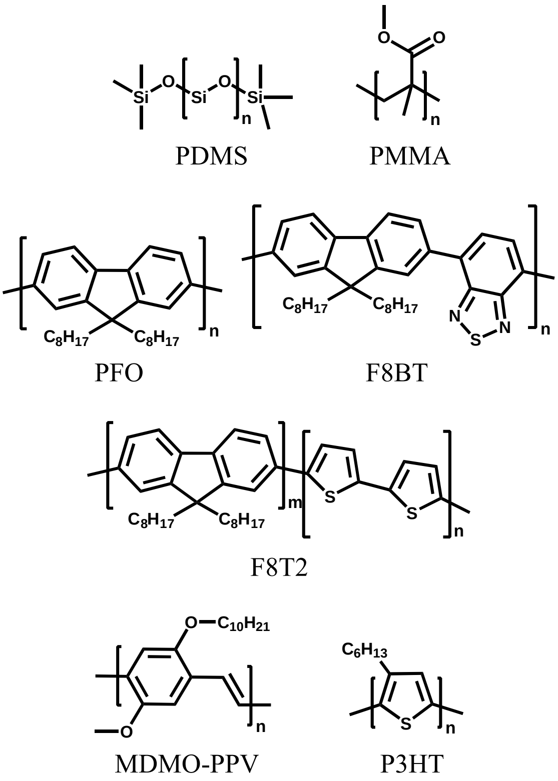

Fig. 4.1. Chemical structures of PDMS, PMMA, PFO, F8BT, F8T2, MDMO-PPV and P3HT.

4.2. Vacuum-based infiltration

The fabrication of PMMA structures was developed by a template-assisted method that entails the vacuum infiltration of a solution into the template.

This experimental process consists in the infiltration by putting a drop of the PMMA solution in toluene on top of the sample located under vacuum, as is shown in Fig. 4.2, followed by heating the sample in order to evaporate the remaining solvent.

PMMA microtubes and micropillars using silicon membranes and close-end-pore silicon were fabricated by this experimental process. PMMA nanopillars were also obtained using self-ordered nanoporous alumina as template.

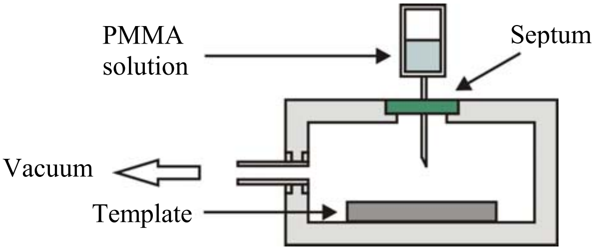

Fig. 4.2. Schematic diagram of the vacuum chamber used to infiltrate the PMMA solution**.**

4.2.1. PMMA micro- and nanostructures

PMMA microtubes were obtained by the infiltration of 30 wt.% PMMA solution in toluene, employing macroporous silicon membrane as template. Fig. 4.3a-b shows the obtained microtubes with a length of 150 µm (aspect ratio of 75). The image shows the uniform high aspect ratio and the tubular shape of these polymeric structures because of the template employed. However, when the infiltration was at ambient atmosphere the filling of the pore is similar but the microtubes walls are thicker, as is shown in Fig. 4.3c-d, probably due to the rate of solvent evaporation under vacuum. In other hand, when the PMMA sample is heated at 60 ºC over night, the microtubes walls have similar thickness than heated at 100 ºC during 3 h. The results indicate that the experimental conditions modify the thickness of the tube walls, but the tube dimensions, length and diameter, are fitted by the template used.

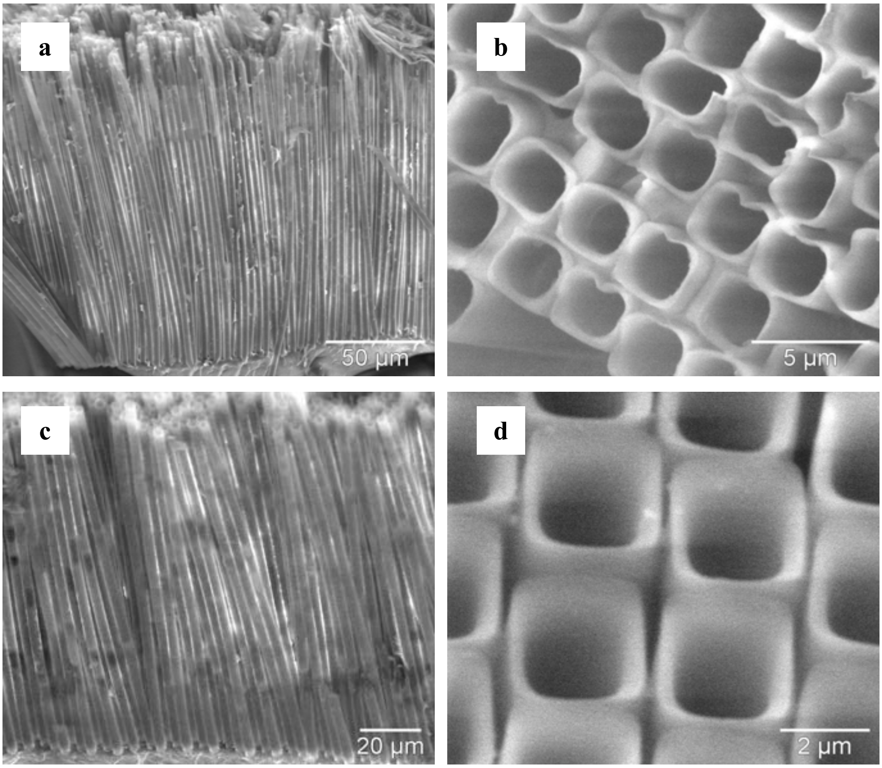

Fig. 4.3. ESEM images of cross-section and top view of PMMA microtubes prepared (a-b) at vacuum or (c-d) at ambient conditions.

In order to study the effect of the pore opened only at one end, silicon templates with different pore depths were employed. PMMA micropillars with aspect ratios between 4.2 and 12 were obtained using the same experimental process as before with a 15 wt.% polymer solution.

As is shown in Fig. 4.4 and 4.5, the PMMA micropillars released from the template possess caps with hemispherical shape, indicating that the micropillars are replicas of the pore bottoms.

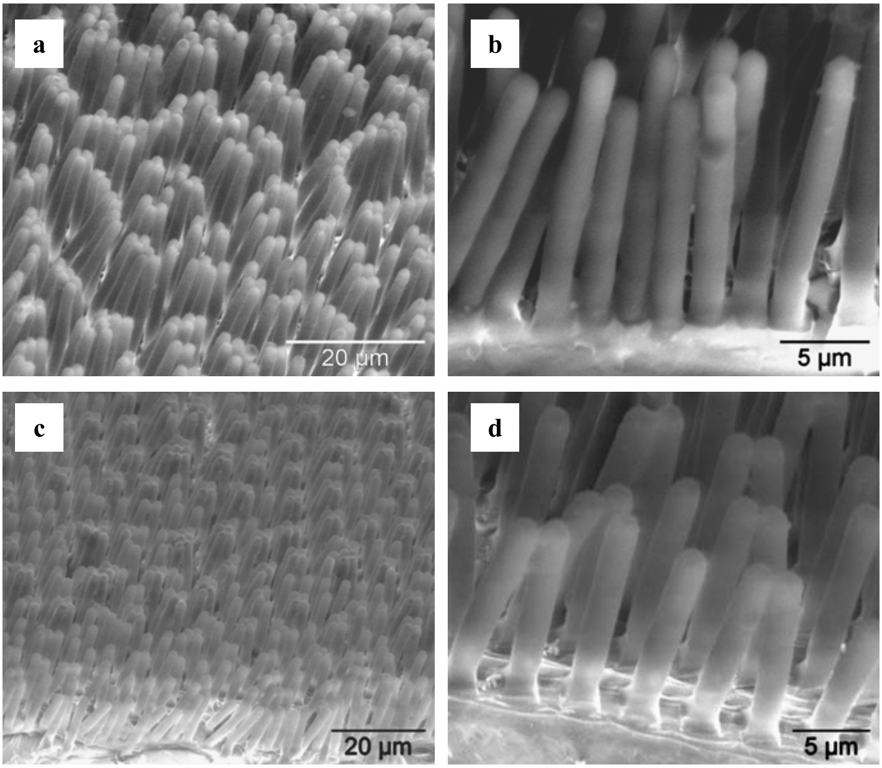

Fig. 4.4. ESEM images of PMMA micropillars with 1.8 µm of diameter and (a-b) 22 µm and (c-d) 17.5 µm of height.

Free-standing micropillars can be produced by using silicon templates with a pore depth less than 12 µm, which means an aspect ratio of 7. PMMA pillars start to be congregated into disordered domains when the pore depth value is higher than 15 µm and this problem increase when the template pores present a depth of 22 µm, which means an aspect ratio of 12.

In order to investigate the formation of the micropillars, different concentrations of the PMMA solution have been studied. The results show that the amount of the polymer does not affect the preparation of the micropillars. Experiments with 5 wt.% and 30 wt.% PMMA solution were carried out and similar morphology to the samples prepared with 15 wt.% polymer solution were obtained.

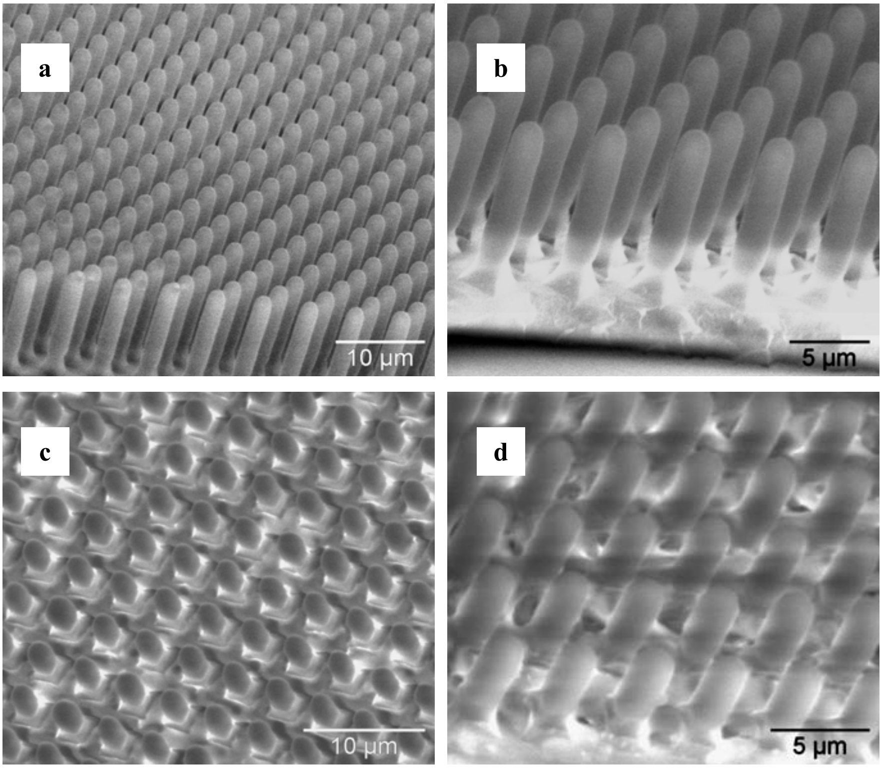

Fig. 4.5. ESEM images of PMMA micropillars with 1.8 µm of diameter and (a-b) 12 µm and (c-d) 7.5 µm of height.

The experimental process without vacuum was also carried out. In this case, the micropillars obtained were worst formed. The results indicate that in order to prepare PMMA pillars the vacuum is a necessary condition.

Polymer nanostructures were also prepared using self-ordered nanoporous alumina as template. Nanoporous alumina with pore depths between 200 nm and 1.3 µm and pore diameters between 50 and 65 nm were employed in order to prepare PMMA nanopillars with aspect ratios between 3 and 25.

In this case, the concentration of the PMMA solution in toluene was 20 wt.% and the alumina template was removed by a 1 M sodium hydroxide (NaOH) aqueous solution at room temperature for 20 min.

Fig. 4.6 shows ESEM images of PMMA nanopillars with an aspect ratio of 25 (1.3 μm/50 nm) after remove the nanoporous alumina template. The image shows that nanopillars are aggregated for this aspect ratio.

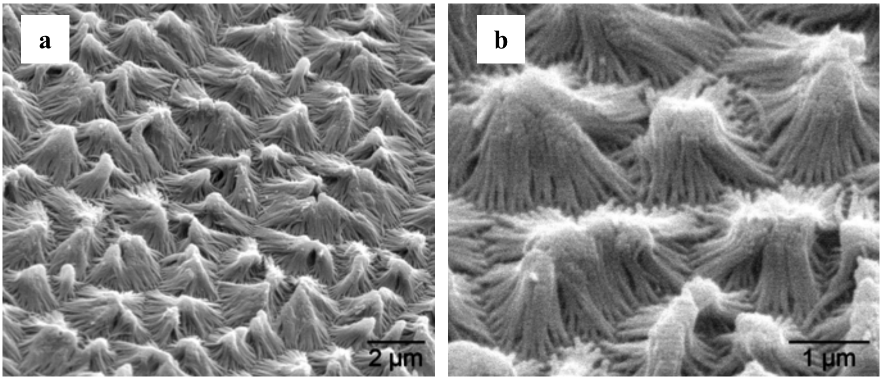

Fig. 4.6. ESEM images of PMMA nanopillars with 50 nm of diameter and 1.3 μm of height.

After these first results, the pore diameter was increased and the pore depth was decreased to obtain a structure with an aspect ratio that allows free-standing nanopillars. As Fig. 4.7a-b shows, the resulting nanopillars were close and wide with an aspect ratio of 3 (200 nm/65 nm). However, when we decreased the diameter to 55 nm, free-standing PMMA nanopillars are obtained with a aspect ratio of 3.6 (Fig. 4.7c-d).

In order to improve the formation of nanopillars with a higher aspect ratio, the same experiment was carried out with an increasing of the template pore depth. As is shown in Fig. 4.8, ESEM images demonstrate nanopillars were aggregated into disordered domains.

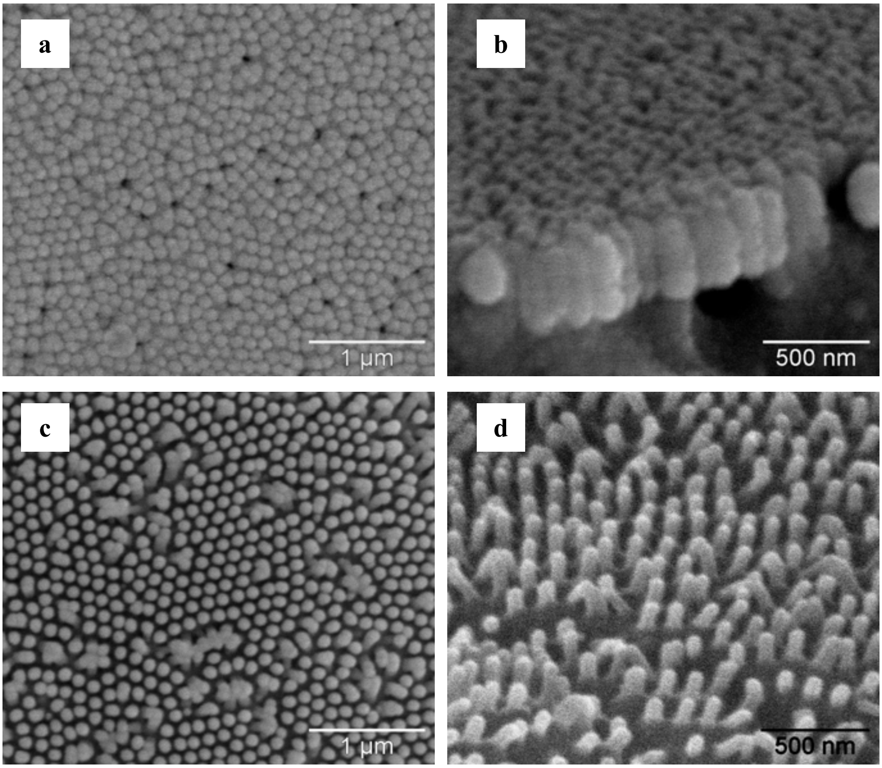

Fig. 4.7. ESEM images of PMMA nanopillars with aspect ratio of (a-b) 3 and (c-d) 3.6.

The results show that free-standing nanopillars can be produce using alumina template with a pore depth of 200 nm and pore diameter of 55 nm (aspect ratio of 3.6). When the aspect ratio is higher than 5, the nanopillars start to be aggregated into disordered domains using this vacuum infiltration method and employing porous alumina as template.

In the literature is reported a method for fabrication of free-standing PMMA nanopillars using H_3PO_4 (instead of NaOH) for etching the nanoporous alumina template [3, 31] which is based in photopolymerisation. We have employed a different method to prepare polymeric nanostructures, but we have also tried to remove the template using H_3PO_4 in order to obtain free-standing nanopillars. The results were similar to the etching with NaOH.

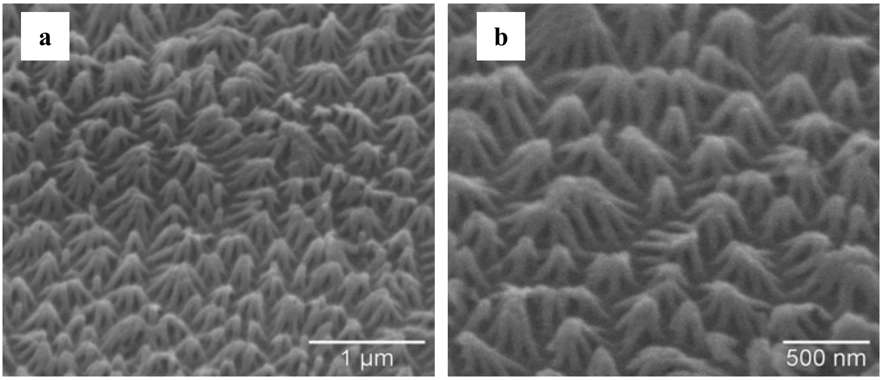

Fig. 4.8. ESEM images of PMMA nanopillars with about 300 nm of height (aspect ratio of 5.5).

4.3. Melt-assisted technique

Structures made from P3HT were prepared employing the experimental process of melt-assisted template wetting. This process entails the annealing of the polymer at a temperature above the melting point (mp) of the polymer. The experimental steps were carried out as is explained below.

Firstly, a 20 mg ml^{-1} solution of P3HT in tetrahydrofurane (THF) was dropped cast on a glass coverslip and left to dry in order to form a thick P3HT layer. Secondly, this layer was soaked in a 3 M aqueous solution of sodium hydroxide (NaOH) for 10 s, rinsed with deionised water. It was peeled off the glass support and placed onto the template. Finally, the sample was placed at 250 °C (P3HT mp: 238 ºC) for 30 min, in order to melt inject the polymer into the porous template, and, then, was slowly cooled to room temperature followed by the removal of the template.

Macroporous silicon membrane, close-end-pore silicon and self-ordered nanoporous alumina were employed in order to obtain PMMA microtubes, micro- and nanopillars. In addition, this process was checked using disordered macroporous silicon as template.

4.3.1. P3HT micro- and nanostructures

Fig. 4.9 shows an array of P3HT microtubes after removing the silicon template with pore depth values of 40 μm and 100 μm (aspect ratio of 20 and 50, respectively). The image demonstrates the tubular shape of these polymeric structures due to the membrane template and the efficiency of the melt-assisted wetting process for preparation microtubes with different lengths.

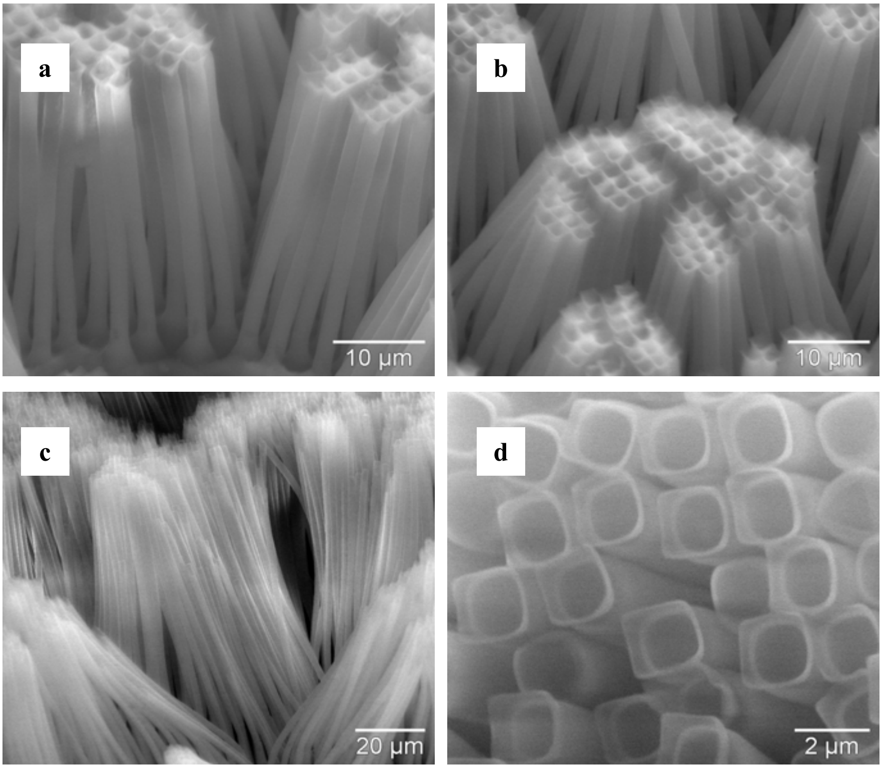

Fig. 4.9. ESEM images of P3HT microtubes with 2 μm of diameter and (a-b) 40 and (c-d) 100 μm of length.

In order to study the influence of the template on the microstructures fabrication, close-end-pore silicon with different pore depths were employed. Fig. 4.10 shows the obtained P3HT micropillars with a height of 22 µm (aspect ratio of 12). The images demonstrate that some of these pillars were aggregated into disordered domains probably due to the flexibility of P3HT and the aspect ratio of the pillars.

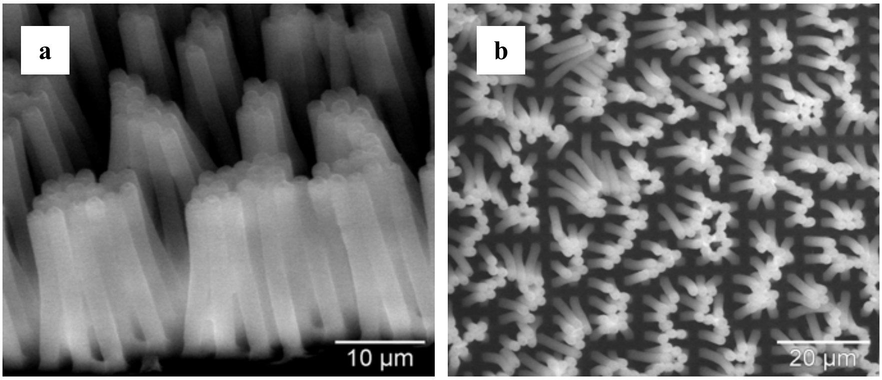

Fig. 4.10. ESEM images of P3HT micropillars with 1.8 µm of diameter and 22 µm of height.

Fig. 4.11 shows P3HT micropillars with spherical shape in the tip, indicating that the pillars are replicas of the pore bottom of the templates, with a pore depth of 17.5 µm and 7.5 µm (aspect ratio of 10 and 4 respectively). Free-standing P3HT micropillars can be obtained from a template with an aspect ratio of about 7.

The same experimental process could be carried out using disordered macroporous silicon as template. Fig. 4.12 shows P3HT micropillars disordered and aggregated, where the inhomogeneity of the micropillars shape is due to the template employed. These results indicate that the close-end-pore silicon used as template only influences the micropillars shape.

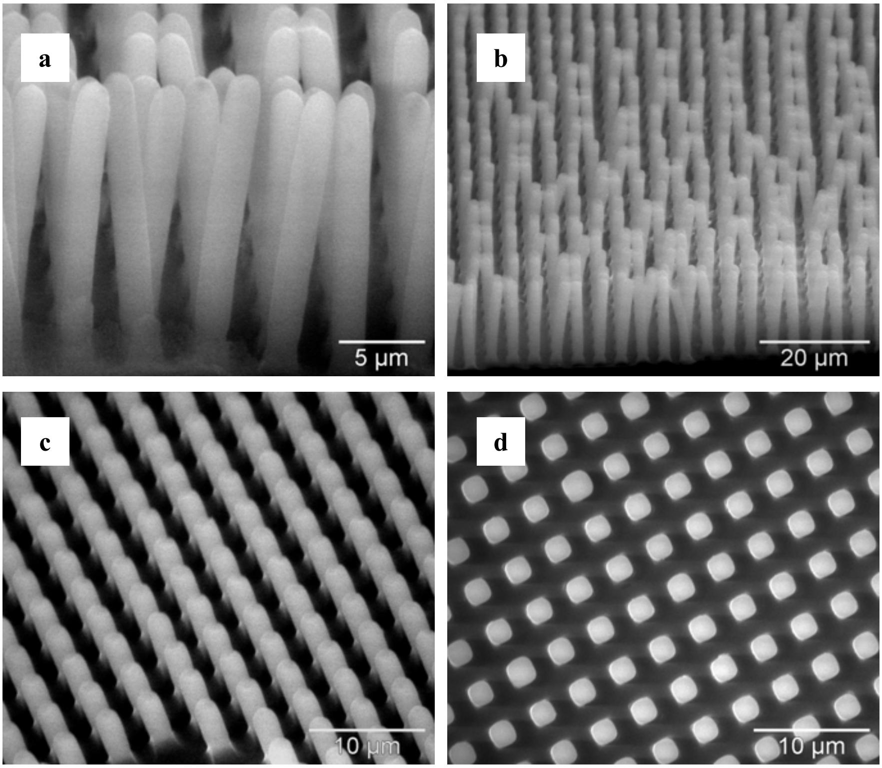

Fig. 4.11. ESEM images of P3HT micropillars with 1.8 µm of diameter and (a-b) 17.5 µm and (c-d) 7.5 µm of height.

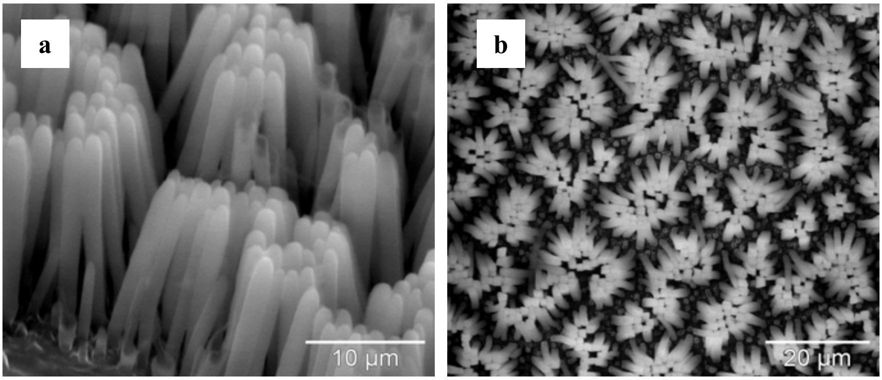

Fig. 4.12. ESEM images of P3HT micropillars with about 1 µm of diameter and 17 µm of average height, prepared from disordered macroporous silicon.

Then, the preparation of polymer nanopillars by melt-assisted technique was studied. In this case, nanoporous alumina with pore diameter of 225 nm and pore depths of 3.5 µm, 1.5 µm, 1 µm and 600 nm (aspect ratio from 16 to 2.7) prepared in phosphoric acid at 160 V was employed as template.

The P3HT nanopillars obtained are shown in Fig. 4.13. Even nanopillars with aspect ratio of 2.7 seem to be partially aggregated, as is shown in Fig. 4.13d, but this effect could be increased due to the defects on the nanoporous alumina template prepared from phosphoric acid. The homogeneity in length of these nanopillars is due to the nanoporous alumina used as template.

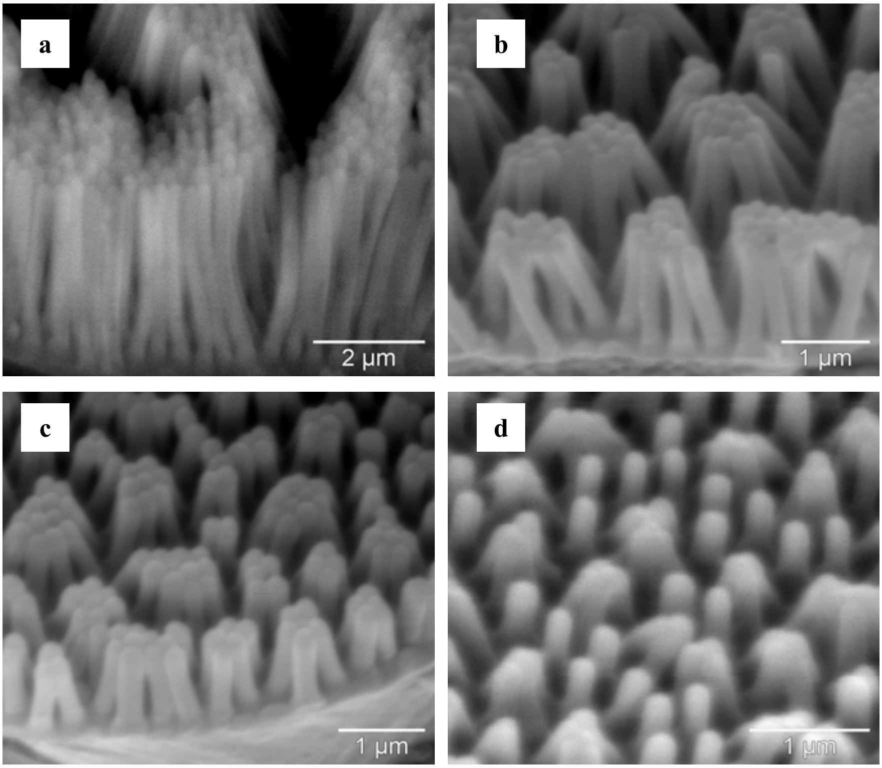

Fig. 4.13. ESEM images of P3HT nanopillars with 225 nm of diameter and (a) 3.5 µm, (b) 1.5 µm, (c) 1 µm and (d) 600 nm of height.

4.4. Wetting-based infiltration

In this section, polymer micro- and nanostructures were obtained by wetting the template in order to fill the pores and obtain the inverse replica. This experimental process can be developed without solvent or using a polymer solution in a suitable solvent. PDMS was infiltrated into macroporous silicon and cured inside the pores to obtain PDMS structures. Using conjugated polymer solutions, micro- and nanostructures were prepared from macroporous silicon and nanoporous alumina.

4.4.1. PDMS microstructures

The wetting-based infiltration process was used in samples prepared from PDMS, which must be cured at 110ºC to obtain the solid state. Then, it is not necessary diluted in a solvent because the polymer is cured after the infiltration process.

PDMS was prepared by thoroughly mixing and degassing a 10:1 ratio of liquid silicon base and a curing agent. The resulting mixture was dropped on top of the template at room temperature and, then, cured at 110 ºC during 3 h.

Macroporous silicon membranes and closed-end-pore macroporous silicon was used as template in order to obtain microfibres and micropillars.

Fig. 4.14 shows PDMS microfibres obtained after removing the silicon membrane by a basic solution. The image shows the softness of the polymer. The microfibres with 150 µm of length and 2 µm of diameter (aspect ratio of 75) are apparently solid, even though the template employed was a membrane, probably due to the properties of the PDMS.

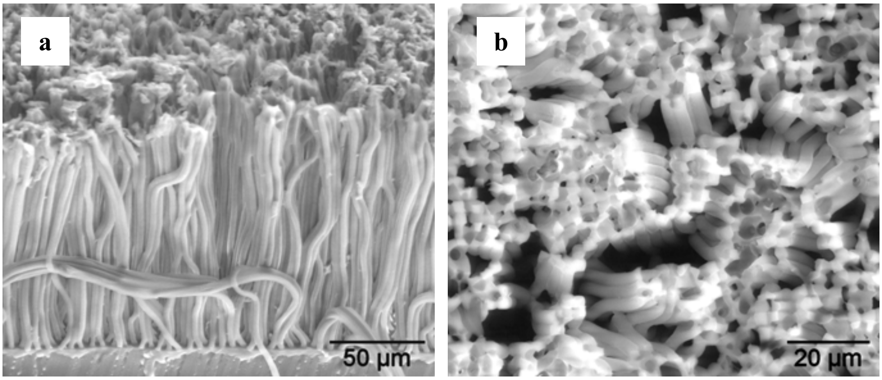

Fig. 4.14. ESEM images of cross-section and top view of PDMS microfibres after removing the macroporous silicon membrane.

When the polymer sample is peeled off the macroporous silicon membrane, instead of the chemical removal of the template, a PDMS microlens-shaped structure is obtained. Fig. 4.15 shows the ESEM images of a PDMS microlens prepared by this method and a digital photograph of the same sample. The variation of the colour means that the sample is not completely homogeneous.

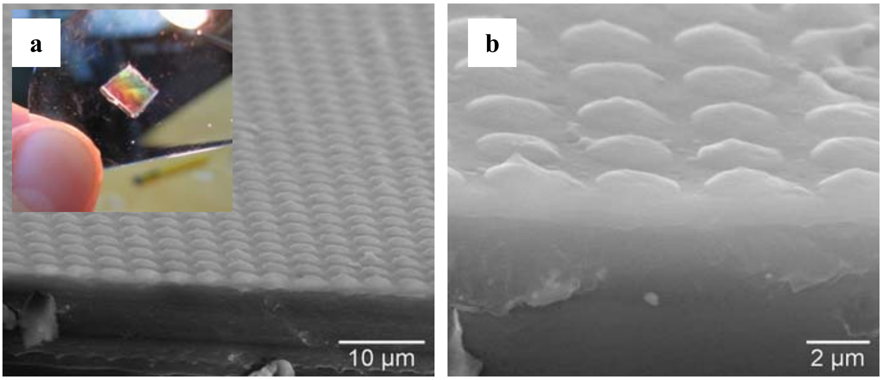

Fig. 4.15. ESEM images of cross-section of PDMS microlens after removing the silicon template by peeling off. The inset shows a digital photograph of the same sample.

Close-end-pore silicon template was infiltrated with PDMS as well, using different pore depths. In this case, we could not eliminate by chemical dissolution the template without damaging the polymer. Although PDMS is compatible with some inorganic bases [32], it is melted when the silicon is removed by KOH (aq) at 40 °C. The micropillars are formed but they cannot stay standing, they tend to bend due to the polymer softness. Following these results, we can conclude that the PDMS is not a good material to obtain structures with our conditions for removing silicon templates, it would be better to use other polymer with wider range of possible structures. Only solid PDMS microfibres, which tend to bend due to the polymer softness, were obtained.

4.4.2. Conjugated polymer micro- and nanostructures

Structures of conjugated polymer were prepared by wetting-based method at ambient conditions. This experimental process entails the infiltration by putting a drop of a polymer solution on top of the template in order to fill the pores.

Polymer micropillars were obtained using disordered macroporous silicon as template. F8BT, F8T2, MDMO-PPV and P3HT solution were prepared in tetrahydrofurane (THF), but PFO was diluted in chloroform ($CHCl_3$), due to the low solubility of PFO in THF.

Using nanoporous alumina as template, we have also study the influence of solvents with different boiling points (bp) in the fabrication of polymer nanopillars. As the solvents used previously, THF, and $CHCl_3$ for PFO, have a low bp (65-67 ºC and 60.5-61.5 ºC, respectively), chlorobenzene (CB) was selected as a solvent with higher bp (132 ºC). Then, THF, or $CHCl_3$, and CB were used in order to prepare the polymer solutions employed for the infiltration process.

The summarize of the concentrations used for each solvent is presented in Table 4.1. As is shown, F8T2 solution in CB was not prepared, because it is not soluble, and MDMO-PPV was diluted at a lower concentration due to its low solubility in CB.

	Concentration (mg ml^{-1})		
Polymer	**THF**	**CHCl$_3$**	**CB**
PFO	–	60	60
F8BT	30	–	60
F8T2	30	–	–
MDMO-PPV	30	–	30
P3HT	30	–	60

Table 4.1. Concentrations of the polymer solutions used with each solvent.

Fig. 4.16 shows some of the polymer micropillars obtained, with height from an average of 2 to 9 µm and about 1 µm of diameter (aspect ratio from 2 to 9). The micropillars started to be aggregated depending on the aspect ratio of the sample and the softness of the polymer. The spherical shape in the tips is also observed which means that the pillars are replicas of the pore bottom of the templates, although MDMO-PPV micropillars with an aspect ratio of 6 were not completely formed, as can be seen in Fig. 4.16c.

In some cases, micropillars with 20 µm of height could also be obtained and, as could be expected, the structure was completely aggregated (Fig. 4.17).

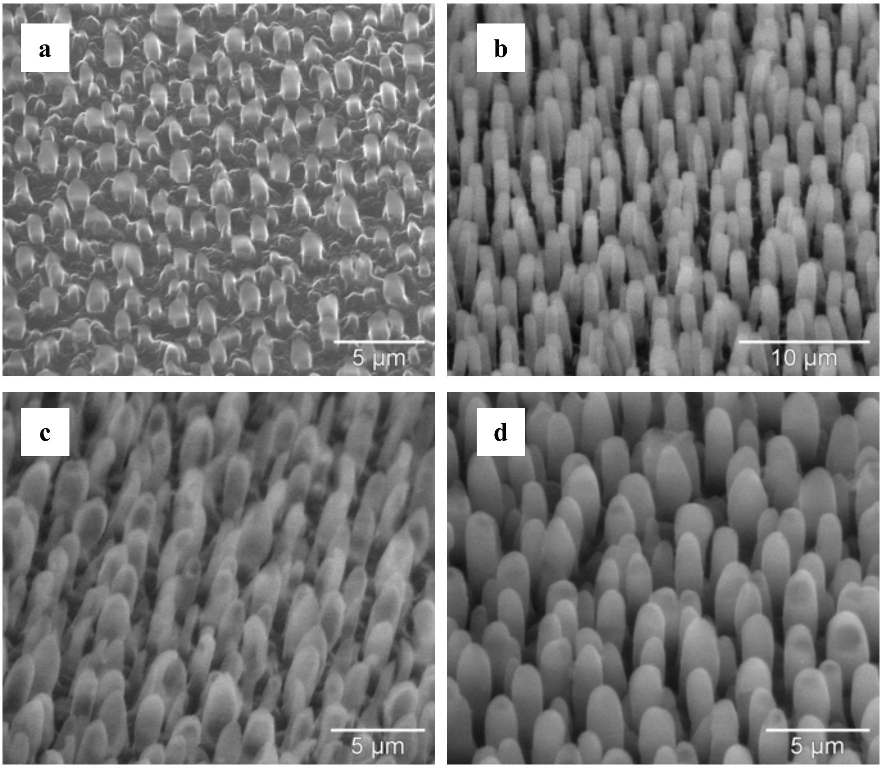

Fig. 4.16. ESEM images of (a) PFO, (b) F8T2, (c) MDMO-PPV and (d) P3HT micropillars (aspect ratios of 3, 20, 6 and 6, respectively).

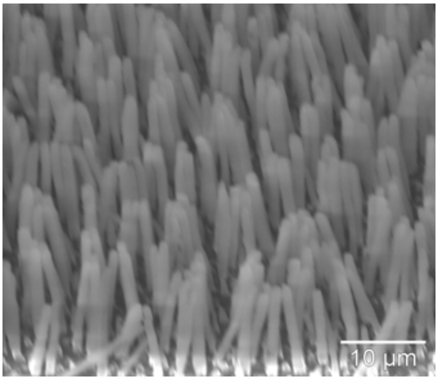

Fig. 4.17. ESEM images of F8T2 micropillars with 20 µm of height (aspect ratio of 20).

Nanoporous alumina with 225 nm of pore diameter and 500 nm and 1 µm of pore depths were used as template. Polymer nanopillars were prepared using solutions in THF, or $CHCl_3$, and CB in order to study the influence of solvents with different boiling points.

Fig. 4.18 shows some polymer nanopillars with diameters of 225 nm and height from 500 nm to 1 µm (aspect ratio of 2 and 4, respectively) prepared using THF or $CHCl_3$ by the infiltration of nanoporous alumina template. Free-standing nanopillars with aspect ratio of 2 were obtained in contrast with the higher aspect ratio nanopillars.

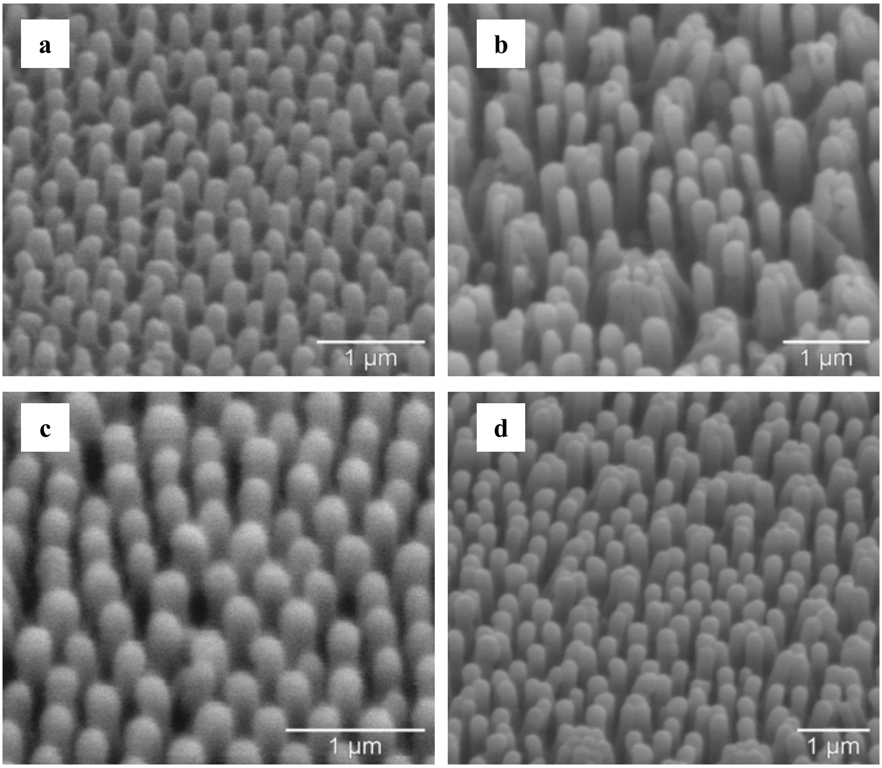

Fig. 4.18. ESEM images of (a) F8BT, (b) F8T2, (c) MDMO-PPV and (d) P3HT nanopillars (aspect ratio of 2, 4, 2 and 4 respectively), prepared using THF as solvent.

Fig. 4.19 shows the free-standing polymer nanopillars, with an aspect ratio of 2, obtained using CB as solvent.

Finally, nanoporous alumina with pore diameter of 80 nm and pore depth of 150 nm (aspect ratio of 2) was also employed as template. In these conditions, some polymer structures were not obtained probably due to the high solution concentration. Fig. 4.20 shows the F8BT polymer nanopillars obtained from CB solution, which was more successfully infiltrated.

The results mean that the polymer nanopillars obtained from the same template are better formed when CB is employed as solvent probably due to the boiling point.

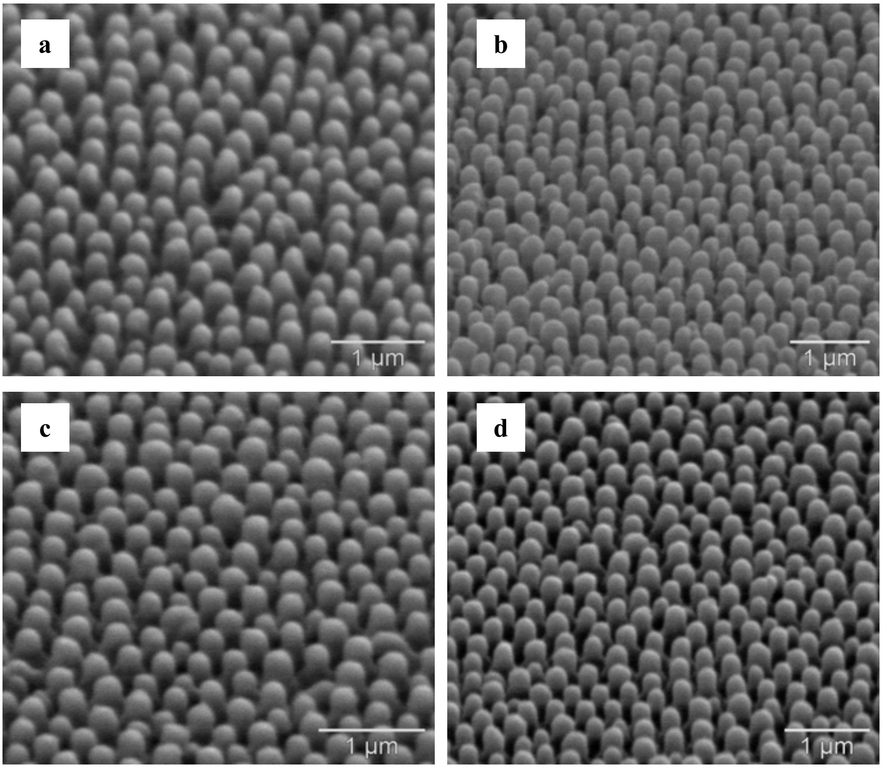

Fig. 4.19. ESEM images of a) PFO, b) F8BT, c) MDMO-PPV and d) P3HT nanopillars (aspect ratio of 2), prepared using CB as solvent.

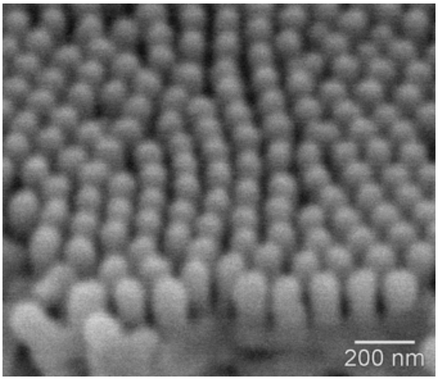

Fig. 4.20. ESEM image of F8BT nanopillars with 80 nm of diameter and 150 nm of height (aspect ratio of 2).

4.5. Spin-coating process

Spin-coating is probably one of the most used experimental process employed in the preparation of layers in applications such as solar cells which require structures in the nanometer range. This process can produce uniform thin films, of some nanometers, with high reproducibility [105, 106]. Then, the fabrication of nanopillars by this method could have a wide range of potential applications. By this reasons, polymer nanopillars was prepared using self-ordered nanoporous alumina as template.

The high evaporation rates of tetrahydrofurane (THF) and chloroform ($CHCl_3$) during spin-coating forbid the utilization of these solvent for this process. In order to decrease the evaporation ratio during the spin-coating process, chlorobenzene (CB) was used for all polymer solutions.

In this case, the experimental process entails the polymer infiltration by spin-coating at 1000 rpm for 30 seconds from a solution in CB and, then, the heating of the samples at 30 ºC for 3 hours.

As in the previous section, the concentration of PFO, F8BT and P3HT solutions was 60 mg ml^{-1}, and in MDMO-PPV samples the concentration was 30 mg ml^{-1} due to the low solubility of MDMO-PPV in CB.

4.5.1. Conjugated polymer nanopillars

Fig. 4.21 shows the polymer nanopillars obtained by this experimental process. As the dimensions of the template were adjusted, the free-standing nanopillars were obtained with about 225 nm of diameter and 500 nm of height (aspect ratio about 2).

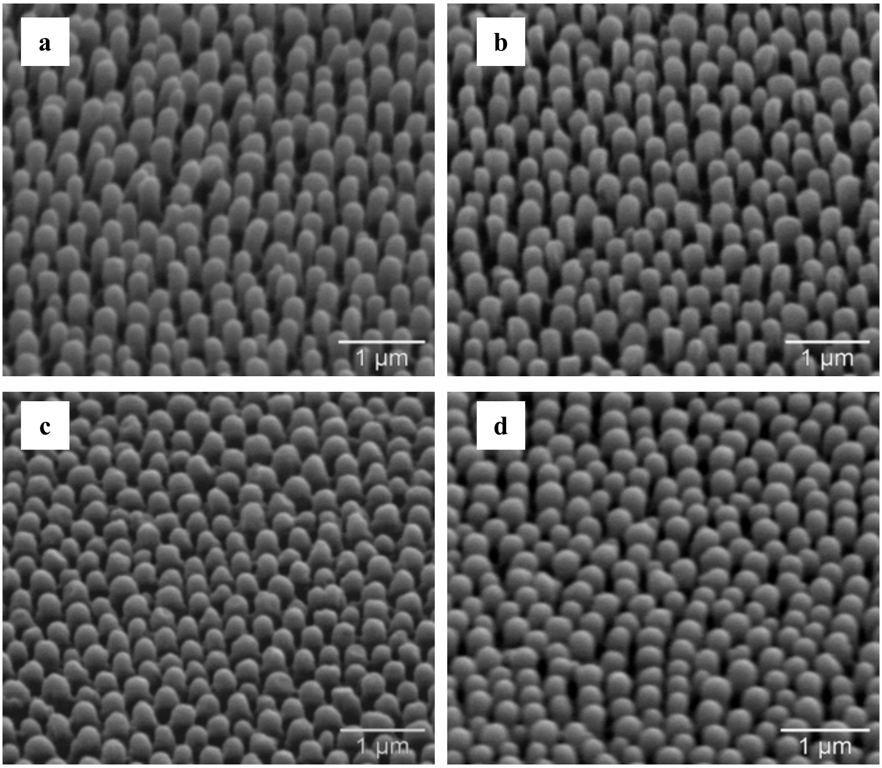

Fig. 4.21. ESEM images of (a) PFO, (b) F8BT, (c) MDMO-PPV and (d) P3HT nanopillars (aspect ratio of 2).

As Fig. 4.22 shows, the polymer structures obtained are supported on a thin film, with a height less than 500 nm, due to the spin-coating process, in contrast with the thick films which were produced in the other experimental processes. This property of the polymer structures prepared by this process increases the amount of potential applications for these nanopillars.

As well, nanoporous alumina with a pore diameter of 80 nm and pore depth of 150 nm was used as template. In this case, the polymers were not successfully infiltrated, probably due to the higher ratio of solvent evaporation in the spin-coating process.

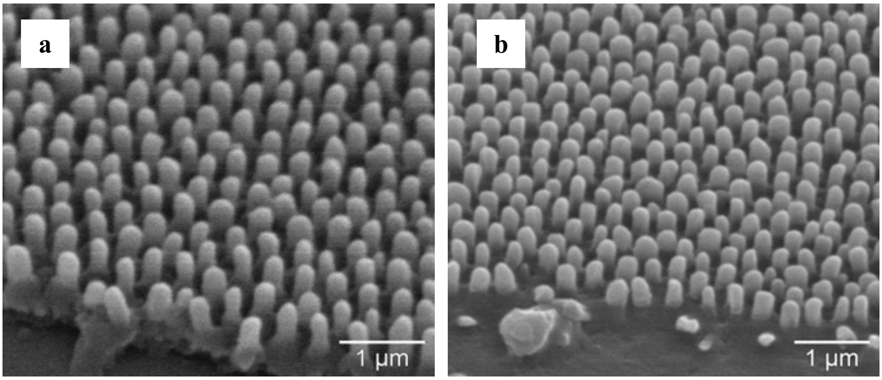

Fig. 4.22. ESEM images of (a) PFO, (b) F8BT nanopillars (aspect ratio of 2) supported on a film.

4.6. Conclusions

In this chapter, we have presented the polymer structures prepared by the template-assisted technique using different experimental process. The polymer micro- and nanostructures obtained present many potential applications in different fields. The template-assisted technique does not require specialize equipment and can be easily adapted to different polymers. The templates used were macroporous silicon, membranes and closed-end-pore, for microstructures and self-ordered nanoporous alumina, for nanostructures, which are well-studied porous materials. For each experimental process, at least one polymer was selected to be infiltrated. As well, polymers from different chemical families were employed.

In order to study the vacuum-based method, polymer solution was infiltrated into macroporous silicon and self-ordered alumina. PMMA micro- and nanostructures with a wide range of dimension were obtained by this method. Without vacuum, PMMA structures were not well formed, but other polymer can be infiltrated from solutions at ambient conditions, as was demonstrated below.

Other experimental process studied was the melt-assisted method. This process has been demonstrated suitable in order to prepare a wide range of polymer micro- and nanostructures by infiltrating P3HT. Then, this process appears as a potential method to develop different applications. But melting a polymer entails the annealing of the polymer at a temperature above its melting point. For these reasons, the wetting-based method appears as the easiest experimental process in order to prepare polymer structures.

The wetting-based method consists in infiltrating a polymer solution at ambient conditions, in contrast with the experimental process employed for PMMA structures. To develop this method without solvent, PDMS was selected due to it can be cured at 110 ºC. Then, PDMS microfibres were prepared, but the fabrication of micropillars was not possible due to the properties of PDMS. Furthermore, PFO, F8BT, F8T2, MDMO-PPV and P3HT micro- and nanopillars were obtained using THF or $CHCl_3$ as solvents. Due to the wide range of potential application of nanostructures, free-standing nanopillars were also prepared using CB, a solvent with higher boiling point, in order to be compared by photophysical characterization. F8T2 nanopillars were not prepared because F8T2 in not soluble in CB, but F8T2 samples prepared from THF were synthesized to be studied. In general, structures prepared from CB seem to be better formed, probably due to the higher boiling point.

Finally, polymer nanopillars were obtained by the template-assisted technique using the spin-coating process because this method is well known for preparing nanodevices in different areas. The solvent used was CB because its evaporation ratio during the spin-coating process allows the infiltration of the polymer solution into the template. PFO, F8BT, MDMO-PPV and P3HT nanopillars were prepared in order to be compared with the nanopillars prepared by wetting-based infiltration.

To conclude, different kinds of polymer micro- and nanostructures can be prepared by template-assisted technique. The obtained polymer structures present potential application in devices of different areas. Depending on the desire structure and the polymer required, the experimental process should be selected or improved for the particular application.

Chapter 5

UV-Vis absorbance and photoluminescence

UV-Vis absorbance and photoluminescence are well-known techniques to study the optical properties of a material. Both of them are non-destructive and samples do not require any special preparation or any contact. UV-Vis absorption spectrum provides the wavelength and intensity of absorption of near-ultraviolet and visible light by a sample. Photoluminescence provides the wavelength and intensity of emission of the sample due to a previous excitation.

Absorption spectra were measured by a double beam UV-Vis Shimadzu spectrophotometer (UV-1700). Luminescence spectrofluorimeter (Aminco-Bowman Series 2) was used for measuring the emission spectrum of polymer samples. More detailed information is presented in Appendix A.

Conjugated polymers described in the previous chapter (PFO, F8BT, F8T2, MDMO-PPV and P3HT) are photoluminescents. Because that, they can be characterized by these techniques and, then, the optical properties of polymer solutions, films and structures can be studied and compared.

Absorption spectra of polymer solutions and films were obtained, but the pillars spectra were not measured due to the high concentration of the solution that was used in order to fabricate polymer structures. Photoluminescence (PL) spectra of polymer solutions, films and an array of polymer pillars supported on a film were measured. Absorption and PL intensities were normalized by the maximum intensities in order to be compared.

5.1. Polymer solution and film characterization

The UV-Vis absorbance and photoluminescence (PL) spectra of PFO, F8BT, F8T2, MDMO-PPV and P3HT solution, and film prepared in two solvents with different boiling point were recorded. The solvent used were tetrahydrofurane (THF, bp: 65-67 ºC), which was substituted in PFO samples for chloroform ($CHCl_3$, bp: 60.5-61.5 ºC), and chlorobenzene (CB, bp: 132 ºC). Due to the insolubility of F8T2 in CB, the corresponding samples were not obtained. The concentrations for solution and films were 0.02-0.05 mg ml^{-1} and 1 mg ml^{-1}, respectively.

Absorption and PL spectra of polymer films are red-shifted compared to the corresponding spectra of polymer solution, as Fig. 5.1-5.5 show. This effect is attributed to the increasing of molecular interactions between neighbouring molecules in the film state compared to the solution, as is described in the literature [39, 48].

The spectra obtained were fitted by Gaussian functions in order to obtain the peak wavelengths. Absorption peaks of these polymer solutions and films are summarized in Table 5.1 and emission peaks of them are presented in Table 5.2. Detailed Gaussian functions are presented in Appendix B.

Fig. 5.1 shows the absorption and PL spectra of PFO solution and films prepared from $CHCl_3$ and CB. In Fig. 5.1a with $CHCl_3$ as solvent, the PFO solution absorption spectrum is described by a peak at 377 nm and other peak at 397 nm which is assigned to the $S_0 \rightarrow S_1$ 0-0 transition of PFO. The film spectrum is broader with peaks at 380 and 403 nm, and a low energy shoulder at 434 nm characteristic of β-phase PFO [40-43]. When CB is selected as solvent, the absorption peaks of PFO film appear at similar wavelengths than using $CHCl_3$, but the shoulder at 434 nm is more intense. This means that there is a higher fraction of β-phase in the film obtained from CB solution than prepared from $CHCl_3$. With both solvents, the solution PL spectra exhibit a characteristic vibronic progression with peaks located at about 418, 438 and 460 nm due to $S_0 \rightarrow S_1$ 0-0 singlet exciton transition of solution PFO with 0-1, 0-2 and 0-3 vibronic replicas. As well for both solvents, the PFO film spectra exhibit the emission peaks at 439, 465 and 496 nm, which are agree with the PL spectrum of β-phase PFO film described in the literature [41, 42].

Fig. 5.2 shows F8BT absorption and PL spectra prepared from the both solvents, which exhibit one peak but they were better fitted by three Gaussian functions. Using THF and CB as solvent, F8BT solution absorbance spectra present the maximum at 448 nm but the solution prepared from THF is broader than prepared from CB. The film prepared from THF presents an absorption spectrum with the maximum at 443 nm and the film prepared from CB presents an absorption spectrum with the maximum at 463 nm. The Gaussian functions indicate that the F8BT solution PL presents the maximum at 524 nm in THF and at 520 nm in CB. The F8BT film PL spectrum, prepared from THF, is red-shifted about 30 nm compared to film PL spectrum prepared using CB solution. This effect means that the optical properties of the polymer film can be modified by the solvent used [46].

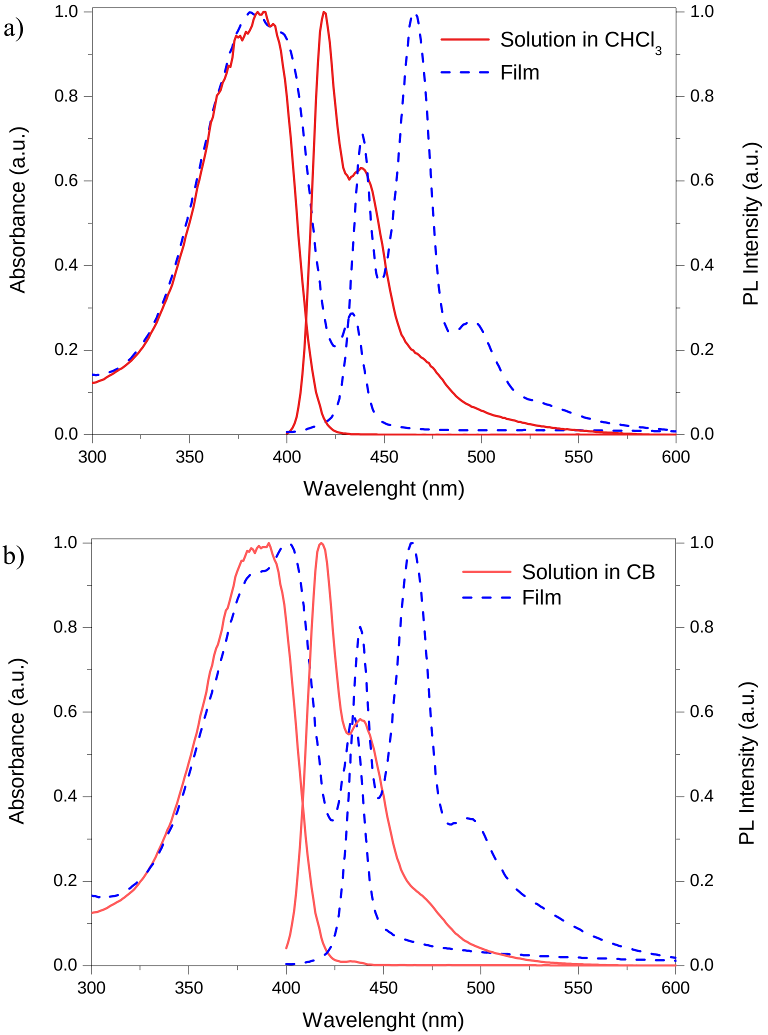

Fig. 5.1. UV-Vis absorbance and photoluminescence spectra of PFO solutions and films prepared from a) chloroform solution and b) chlorobenzene solution.

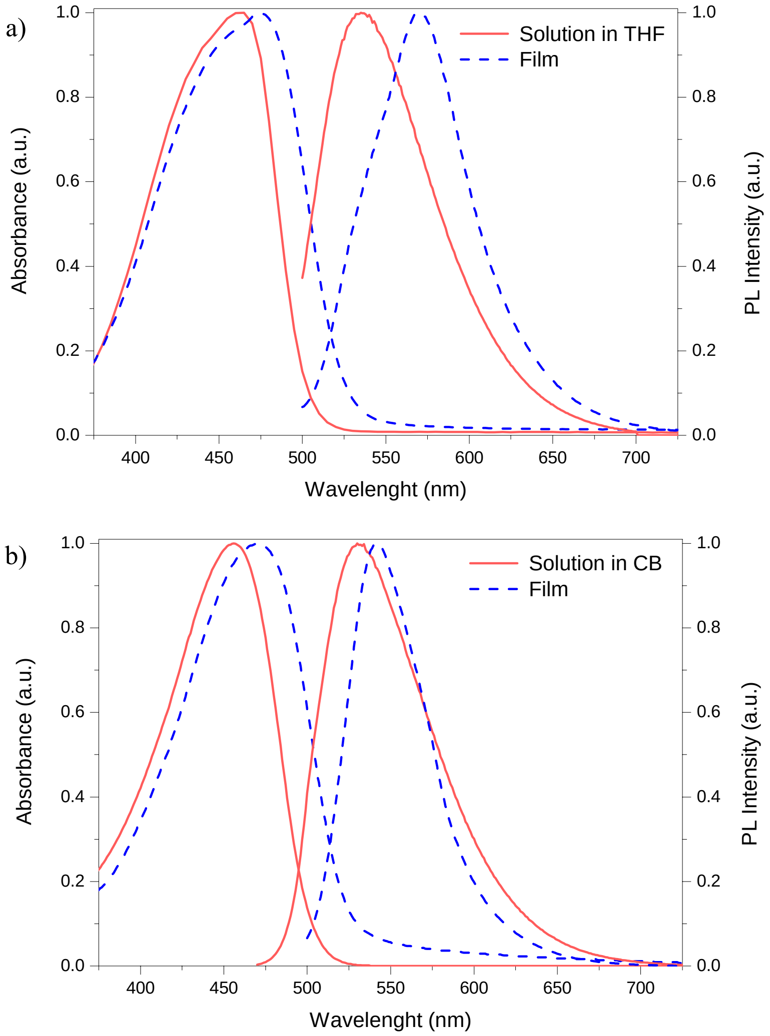

Fig. 5.2. UV-Vis absorbance and photoluminescence spectra of F8BT solutions and films prepared from a) tetrahydrofurane solution and b) chlorobenzene solution.

Fig. 5.3 shows the absorption and PL spectra of F8T2 solution in THF and F8T2 film prepared from a THF solution. The absorption spectra exhibit peaks at 456 and 480 nm for solution and at 441, 475 and 501 nm for film. The PL peaks appear at 497 and 527 nm for solution and at 542 nm with shoulders at 514 and 578 nm for film [48, 107]. These results cannot be compared with any results using CB because F8T2 is not soluble in CB.

As Fig. 5.4 shows, the MDMO-PPV solution absorption spectra are analogues in THF and CB with the maximum about 493 nm. For both solvents, the film absorption spectra are broader than the corresponding solution absorption spectra. The film prepared from CB presents the maximum at similar wavelength than the solution in CB, whereas the film prepared from THF exhibits an absorption spectrum with a red-shift of 15 nm compared to the corresponding solution spectrum. The MDMO-PPV PL solution spectra present the maximum at 547 nm in THF and at 558 nm in CB. The film obtained from both solvents exhibit comparable emission intensities with peaks at 581, 634 and 650 nm [108-110].

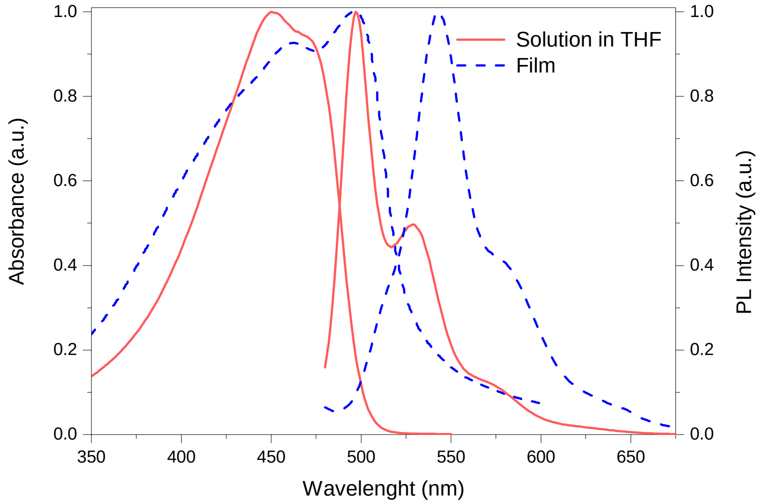

Fig. 5.3. UV-Vis absorbance and photoluminescence spectra of F8T2 solution and film prepared from tetrahydrofurane solution.

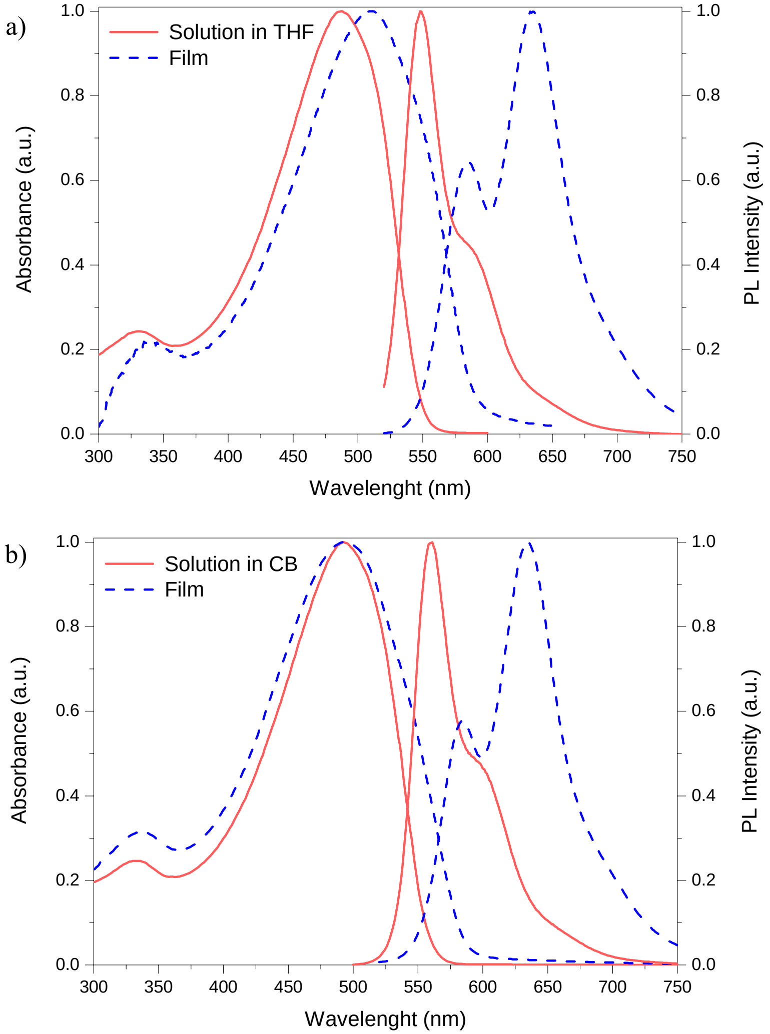

Fig. 5.4. UV-Vis absorbance and photoluminescence spectra of MDMO-PPV solutions and films prepared from a) tetrahydrofurane solution and b) chlorobenzene solution.

Fig. 5.5 shows the P3HT solution and film absorption spectra obtained from THF and CB solutions. The absorption maximum of the solution appears at 492 nm in THF and at 432 nm in CB. The film absorption spectra are red-shifted to 534 nm for THF and 524 nm for CB. With both solvents, the film absorption spectra exhibit a shoulder at about 606 nm. The increasing of this absorption shoulder can be linked to an increasing in the crystallization of the polymer film prepared using CB compared to the film obtained using THF, probably due to the boiling point of the solvents [111, 112]. The solution PL spectra present the maximum at 566 nm in THF and at 572 nm in CB. The film PL spectra obtained using THF and CB exhibit a peak at 639 nm, which presents higher intensity when the solvent used is CB.

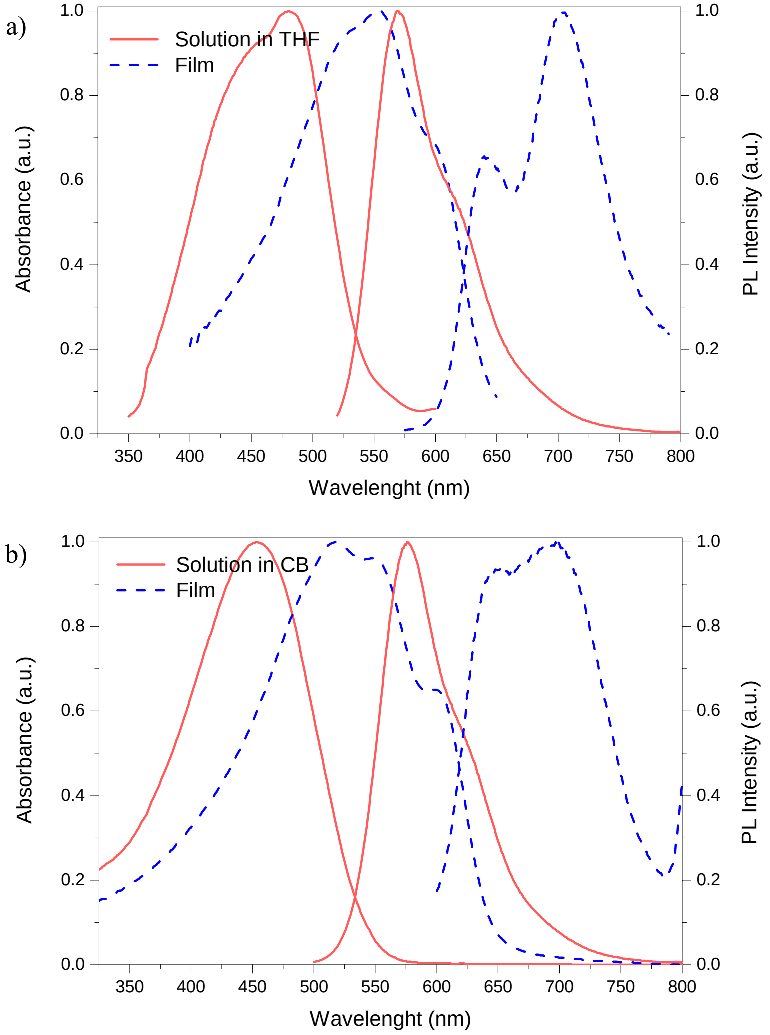

Fig. 5.5. UV-Vis absorbance and photoluminescence spectra of P3HT solutions and films prepared from a) tetrahydrofurane solution and b) chlorobenzene solution.

	THF or Chloroform		**Chlorobenzene**	
Polymer	**Solution (nm)**	**Film (nm)**	**Solution (nm)**	**Film (nm)**
PFO	*377*, 397	*380*, 403, 434	*380*, 397	*387*, 405, 435
F8BT	*448*, 473	*443*, 486	*448*, 472	*463*, 487
F8T2	421, *456*, 480	441, 475, *501*	–	–
MDMO-PPV	329, *490*	339, *516*	329, *496*	330, *508*
P3HT	404, 446, *492*	*534*, 565, 605	*432*, 476	*524*, 563, 607

Table 5.1. Wavelengths of the absorption peaks of polymer solutions and films. Wavelengths in italics are the maxima.

	THF or Chloroform		**Chlorobenzene**	
Polymer	**Solution (nm)**	**Film (nm)**	**Solution (nm)**	**Film (nm)**
PFO	*418*, 437, 469	439, *465*, 496	*417*, 438, 456	438, *464*, 495
F8BT	*524*, 553	533, *570*, 590	*520*, 548, 582	538, *559*, 607
F8T2	*497*, 527, 572	514, *542*, 578	–	–
MDMO-PPV	*547*, 582, 596	581, *634*, 650	*558*, 592, 617	581, *633*, 650
P3HT	*566*, 609	639, *702*	*572*, 677	639, *688*

Table 5.2. Wavelengths of the emission peaks of polymer solutions and films. Wavelengths in italics are the maxima.

5.2. Polymer structures characterization

The study of the photoluminescent properties of the micro-, nanopillars and the corresponding films is carried out in this section. Micropillars with a diameter of about 1 μm and 3 μm of height (aspect ratio of 3), and nanopillars, with 225 nm of diameter and 500 nm of height (aspect ratio of 2) are studied.

The experimental processes of sample preparation by template-assisted technique were explained in Chapter 4.

The absorption spectra of the pillars and the corresponding films were not measured due to the high concentration of the solution that was used in order to prepare the samples.

5.2.1. Polymer micropillars

F8BT, F8T2, MDMO-PPV and P3HT samples were obtained by wetting-based method using a THF solution (30 mg ml^{-1}), but PFO samples were prepared using a $CHCl_3$ solution (60 mg ml^{-1}), due to its low solubility in THF.

Fig. 5.6 shows ESEM images of the polymer micropillars studied by PL, which were obtained from disordered macroporous silicon of about 1 μm of pore diameter and 3 μm of pore depth. The inhomogeneity of the pillars is due to the morphology of the template, as was shown in section 3.1.

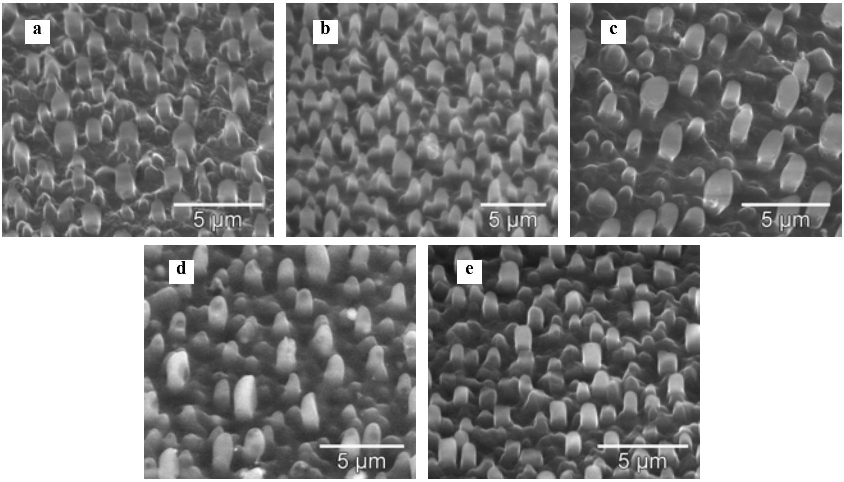

Fig. 5.6. ESEM images of the a) PFO, b) F8BT, c) F8T2, d) MDMO-PPV and e) P3HT micropillars prepared by wetting-based process.

Fig. 5.7-5.11 show the comparison between the PL spectra of films and the corresponding micropillars prepared using THF, or $CHCl_3$ for PFO, as solvent. The PL spectra of these samples were fitted by Gaussian functions and the peaks obtained are summarized in Table 5.3. Detailed Gaussian functions are presented in Appendix B.

In Fig. 5.7, PFO PL spectra exhibited two main peaks: at about 440 and 465 nm. The maximum for both film and micropillars are at 465 nm. The shape of the PL spectra is similar, although the relative intensity of the peak at 440 nm is higher in the film compared to the solution.

Fig. 5.8 shows the F8BT PL spectra which present one maximum and a shoulder. The PL maximum appears at 568 nm for film and at 565 nm for micropillars. These results mean that a slightly blue-shift of 2-3 nm appears in the micropillars emission compared to the film emission.

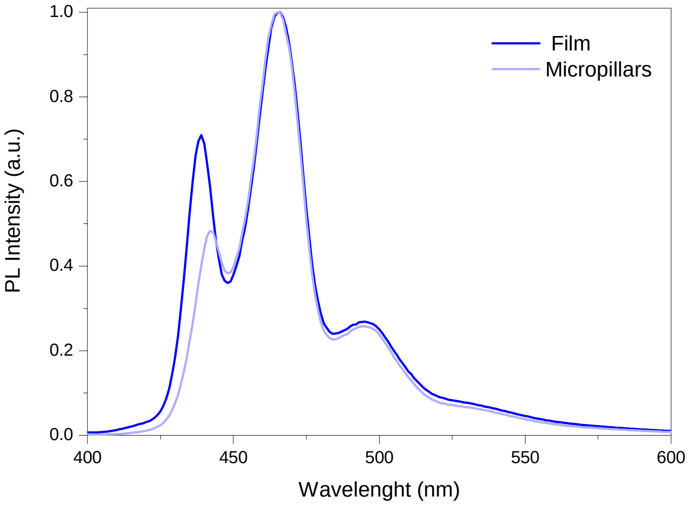

Fig. 5.7. Photoluminescence spectra of PFO film and the corresponding micropillars.

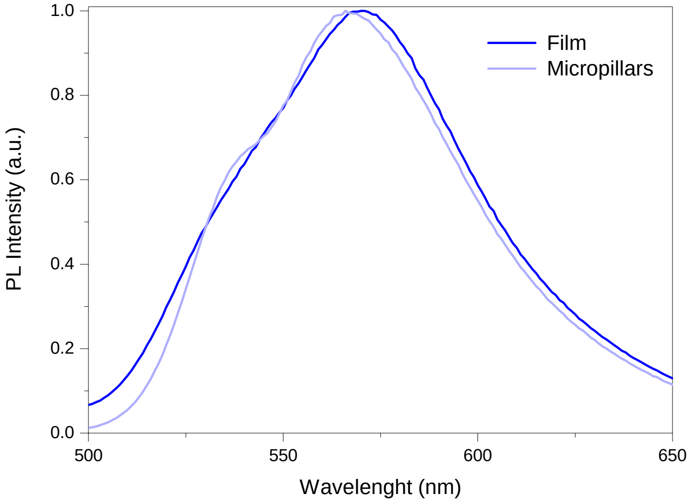

Fig. 5.8. Photoluminescence spectra of F8BT film and the corresponding micropillars.

The F8T2 PL spectra exhibit three peaks as is shown in Fig. 5.9. The maximum for both film and micropillars are at about 542 nm. The shape of the PL spectra only differs in the peak at 517 nm, where the relative intensity of the film spectra increases compared to the corresponding micropillars.

In Fig. 5.10, the MDMO-PPV PL spectra exhibit two peaks. The maxima for film and micropillars are at 633 and 626 nm, respectively. The shoulder appears at 581 nm for film and 586 nm for micropillars, and the relative intensity between the maxima and the shoulder is modified by the structure. The shifts in both peaks indicate that the microstructure influences the optical properties of the polymer.

As Fig. 5.11 shows, the P3HT PL spectra exhibit two peaks. For the film and the micropillars, the maximum appears at about 701 nm. Other peak appears at 639 nm for film and at 643 nm for micropillars, and the relative intensity of this peak increases in nanopillars compared to the film.

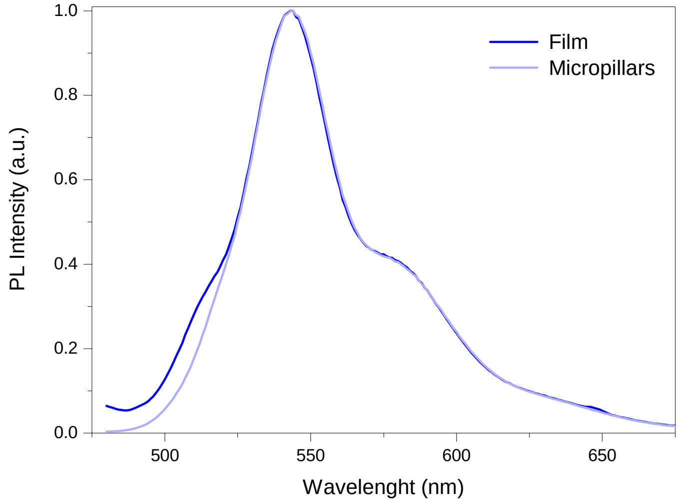

Fig. 5.9. Photoluminescence spectra of F8T2 film and the corresponding micropillars.

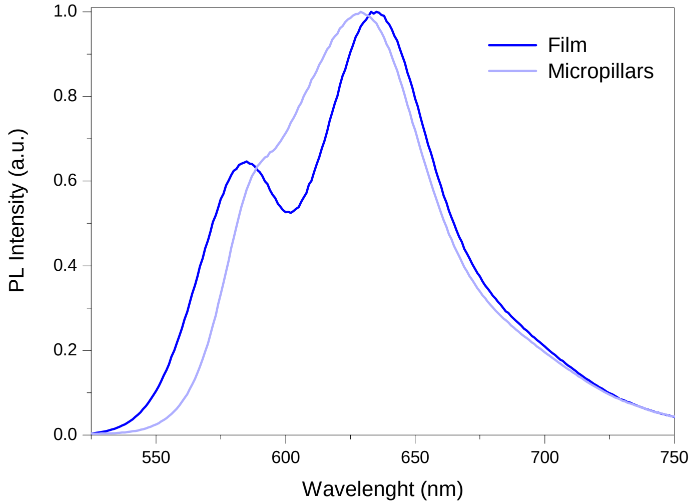

Fig. 5.10. Photoluminescence spectra of MDMO-PPV film and the corresponding micropillars.

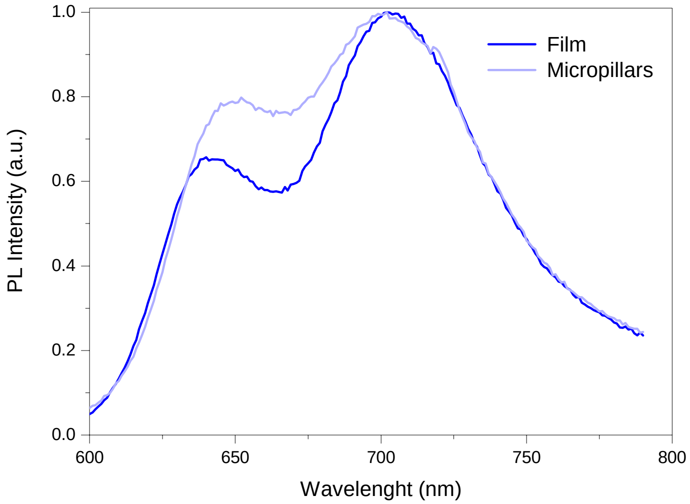

Fig. 5.11. Photoluminescence spectra of P3HT film and the corresponding micropillars.

Polymer	**Film (nm)**	**Micropillars (nm)**
PFO	439, *465*, 496	442, *465*, 495
F8BT	531, *568*, 589	533, *565*, 600
F8T2	516, *542*, 576	518, *543*, 578
MDMO-PPV	581, *633*, 655	586, *626*, 659
P3HT	639, *702*	643, *700*

Table 5.3. Wavelengths of the emission peaks of polymer films and micropillars. Wavelengths in italics are the maxima.

The results indicate that the PL spectra of the polymer micropillars present slightly differences compared to the corresponding film. To conclude, the structure of the micropillars produces some influence in the optical properties of the polymers, but this modification could be increased with templates with lower pore diameter where the polymer chains conformation could be considerably modified.

5.2.2. Polymer nanopillars

The polymer nanostructures have received an increasing attention due to the possibility of tuning the photophysical properties of the polymer with the nanostructure in order to develop a wide range of their potential applications

In this section, measures of the polymer films and nanopillars are performed in order to study the influence in the photoluminescent properties of three parameters: nanostructured sample in contrast with the corresponding film, solvent used and experimental process.

As is summarized in Table 5.4, film and nanopillars **A** were obtained by dropping a tetrahydrofurane (THF) or chloroform ($CHCl_3$) solution on top of the template at room temperature. THF and $CHCl_3$ are solvents with a low boiling point (65-67 ºC and 60.5-61.5 ºC, respectively). When we selected a solvent with higher boiling point, as chlorobenzene (CB) (132 Cº), samples **B** were prepared. Using as well CB as solvent, samples **C** were prepared by spin-coating at 1000 rpm for 30 seconds and heating at 30 ºC for 3 hours. These processes are detailed in Chapter 4.

	Process	**Solvent**	**After deposition**
A	Dropped	THF or Chloroform	Room temperature
B	Dropped	Chlorobenzene	Room temperature
C	Spin-coated	Chlorobenzene	3 hours at 30 ºC

Table 5.4. Experimental conditions of the samples prepared.

The polymer solutions employed to fabricate the samples were prepared at the concentrations presented in Table 5.5. The solution concentrations were selected in order to improve the samples obtained. The lower concentration of MDMO-PPV samples **C** is due to its low solubility in chlorobenzene. F8T2 is not soluble in CB, so no sample was fabricated in order to be compared.

Environmental scanning electron microscopy (ESEM) images of polymer nanopillars obtained from the different experimental processes are compared in Table 5.6. The homogeneity of the nanopillars is due to the morphology of the self-ordered nanoporous alumina used as template.

	Polymer concentration (mg ml^{-1})			
Polymer	**A** (CHCl$_3$)	**A** (THF)	**B**	**C**
PFO	60	–	60	60
F8BT	–	30	30	60
F8T2	–	30	–	–
MDMO-PPV	–	30	30	30
P3HT	–	30	30	60

Table 5.5. Concentrations of the polymer solutions used for preparation the polymer samples.

Fig. 5.12-5.16 show the comparison between the PL spectra of films and the corresponding nanopillars prepared from different experimental processes.

Table 5.7 presents the wavelengths of the peaks fitted by Gaussians functions in order to be compared. Detailed Gaussian functions are presented in Appendix B. The increasing of the peak intensities at lower wavelengths is shown when using CB compared to THF, or CHCl$_3$ for PFO. Furthermore, the spin-coated method also produces this effect.

	A	**B**	**C**
PFO	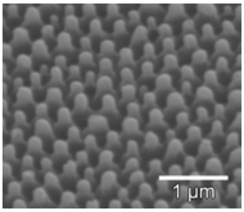	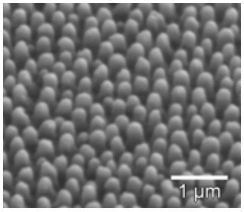	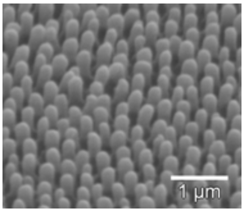
F8BT	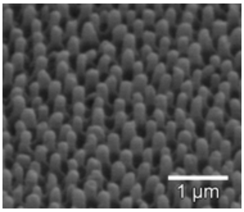	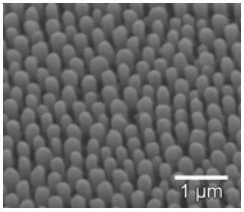	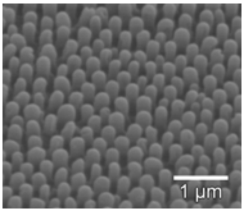
F8T2	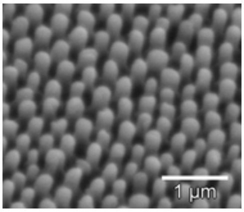	–	–
MDMO-PPV	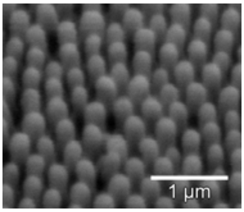	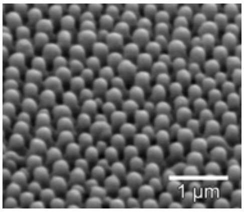	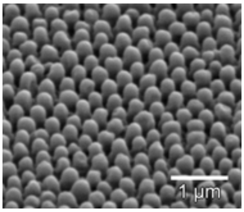
P3HT	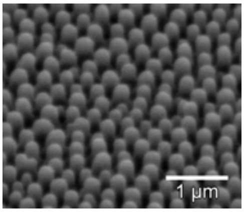	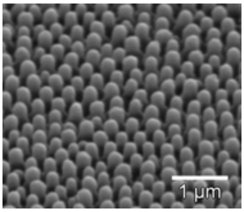	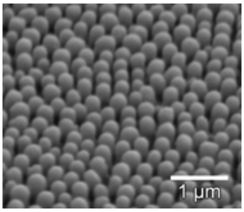

Table 5.6. ESEM images of the polymer nanopillars prepared by three experimental processes (**A**, **B** and **C**).

Fig. 5.12 shows the PL spectra of films and nanopillars **A**, **B** and **C**. For all of them, the spectra exhibit two main peaks, at 439 and 464 nm, but they differ in the relative intensity of the peaks. In nanopillars and film **A**, the maximum is at 464 nm. The maximum appears also at 464 nm for the film **B** but nanopillars **B** presents the maximum at 438 nm. This effect due to the solvent and the nanostructure increases when the samples were prepared by spin-coating. In experimental **C**, both film and nanopillars exhibited the maximum at 438 nm, but the relative intensity of the peak at 463 nm is slightly higher in nanopillars **C** compared to film **C**.

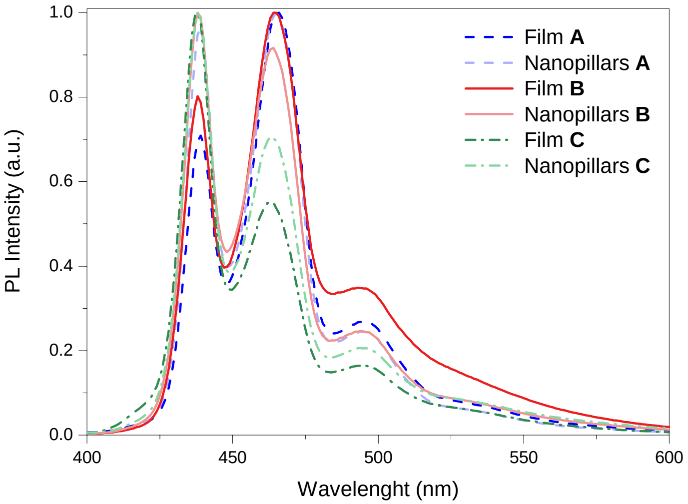

Fig. 5.12. Photoluminescence spectra of PFO films and nanopillars prepared from different experimental processes (**A**, **B** and **C**).

In the F8BT samples (Fig. 5.13), the PL spectra were fitted by 3 Gaussian functions although one peak appears in the PL spectra measured. The PL spectra can be shifted by modifying the relative intensities of the Gaussian functions. Using the Gaussian functions, all the PL spectra present peaks at about 540 and 565 nm. The relative intensity of lower wavelength peaks increases when CB is used as solvent (samples **B**) compared to samples **A** prepared with THF, which produces a blue-shift of the film **B** compared to film **A**. The film **C** is also blue-shifted compared to the film **B** due to the different experimental process. The nanostructure also increases the relative intensity of the peak at 540 nm, which blue-shifts the nanopillars **A**, **B** and **C** compared to the corresponding films **A**, **B** and **C**.

Fig. 5.14 shows the PL spectra of F8T2 samples **A**. The emission spectra of the F8T2 film and nanopillars present peaks at 515, 543 and 579 nm. The relative intensity of the peak at 515 nm increases slightly in nanopillars spectrum compared to the film. These results indicate that the structure does not modify considerably the PL properties of F8T2 using THF as solvent. The comparison of these measurements with spectra of samples prepared using CB as solvent could not be carried out due to the insolubility of F8T2 in CB.

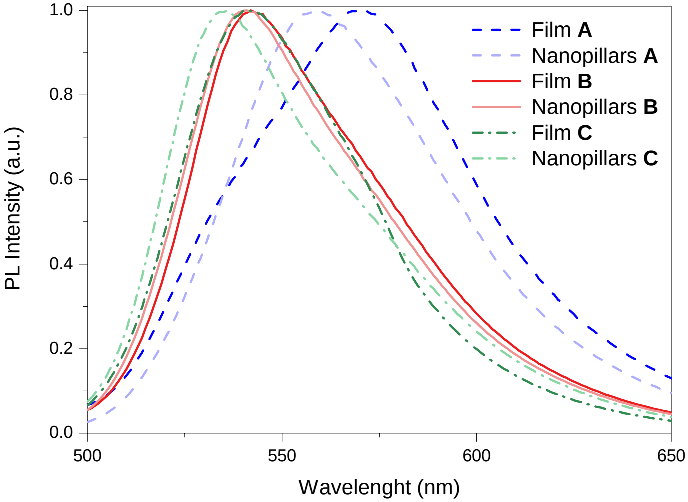

Fig. 5.13. Photoluminescence spectra of F8BT films and nanopillars prepared from different experimental processes (**A**, **B** and **C**).

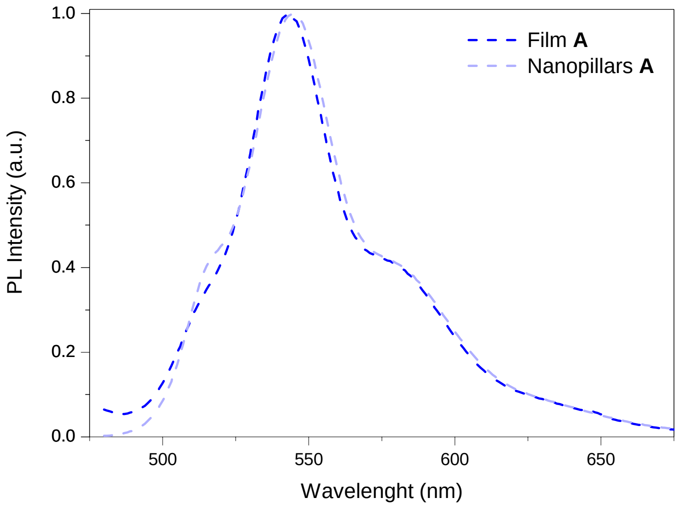

Fig. 5.14. Photoluminescence spectra of F8T2 film and nanopillars prepared from experimental processes **A**.

Fig. 5.15 shows the PL MDMO-PPV samples spectra. Films **A** and **B** emissions present similar shape with the maximum at 634 nm and other peak at 581 nm. In contrast, PL nanopillars **A** and **B** maxima are at about 582 nm with a peak at 625 nm. Nanopillars and film **C** emissions exhibit the maximum at 585 nm, but the relative intensity of the peak at 625 nm is lower in the nanopillars compared to the film. This results means that the peak at 625 nm has less importance in the nanopillars than in the corresponding film. This result shows the experimental process and the nanostructure affects the MDMO-PPV emission with an increasing of the relative intensity of lower wavelength peaks.

Finally, Fig. 5.16 illustrates the PL spectra of P3HT samples **A**, **B** and **C**. Films **A** and **B** spectra exhibit the maximum at about 702 and 688 nm, respectively. In contrast, nanopillars **A** and **B** emissions present the maximum at 637 nm. This result shows the influence of the polymer nanopillars on the PL properties of P3HT. In both nanopillars and film **C**, PL maximum is at 648 nm, which means that the spin-coating increases the intensity of the peaks at lower wavelengths.

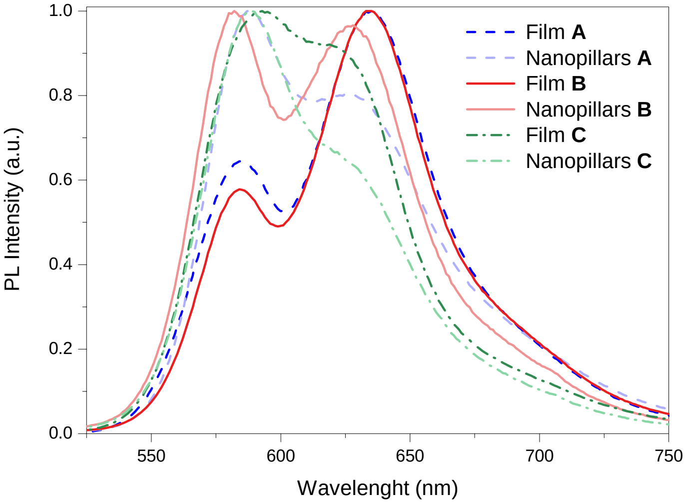

Fig. 5.15. Photoluminescence spectra of MDMO-PPV films and nanopillars prepared from different experimental processes (**A**, **B** and **C**).

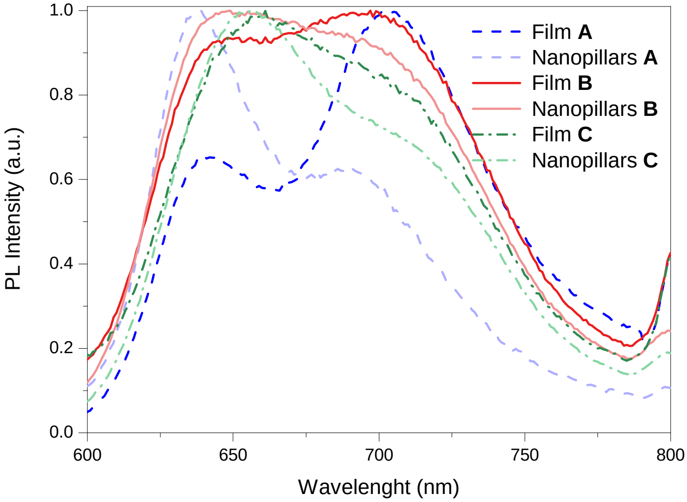

Fig. 5.16. Photoluminescence spectra of P3HT films and nanopillars prepared from different experimental processes (**A**, **B** and **C**).

The results illustrate the influence of the nanostructure in the increasing of the relative intensity of the lower wavelength peaks compared to the corresponding film. Although the optical properties are influenced by the solvent and the experimental process, the results indicate that the nanostructure also influences the PL spectrum of these polymers. Unfortunately, these conclusions cannot be studied for F8T2 samples. It is worth to mention that the influence of the nanostructure is less important in samples prepared by spin-coating.

The polymer samples of the literature present different experimental process, solvent and/or structure than the samples prepared in this thesis [25, 43, 107, 113-115]. But in all reports the optical properties are affected by the nanostructure due to the polymer chain interactions as occurs in the results obtained in this section. The blue-shift in the PL spectra could be attributed to the isolation of molecules in the nanopores, suppressing the intermolecular interactions. Furthermore, in aromatic solvents, such as CB, organic conjugated molecules could adopt a planar conformation while in non-aromatic ones, such as THF, their conformation is twisted [115]. These effects could increase the intensity of lower wavelength peaks, as the obtained measurements indicate.

	PFO	**F8BT**	**F8T2**
Film A	439, *465*, 496	533, *570*, 590	514, *542*, 578
Nanopillars A	439, *464*, 496	550, *570*, 604	515, *543*, 580
Film B	438, *464*, 495	538, *559*, 607	–
Nanopillars B	*438*, 463, 495	*538*, 568, 577	–
Film C	*437*, 462, 496	*536*, 562, 571	–
Nanopillars C	*438*, 463, 495	*532*, 558, 579	–

	MDMO-PPV	**P3HT**
Film A	581, *634*, 650	639, *702*
Nanopillars A	*584*, 624, 656	*636*, 685
Film B	581, *633*, 650	639, *688*
Nanopillars B	*580*, 626, 640	*638*, 687
Film C	*585*, 625, 653	*648*, 699
Nanopillars C	*586*, 626, 637	*649*, 703

Table 5.7. Wavelengths of the emission peaks of films and nanopillars (**A**, **B** and **C**). Wavelengths in italics are the maxima.

5.3. Conclusions

Polymer solutions and films have been studied by UV-Vis absorbance and photoluminescence (PL). The results indicate that polymer films are red-shifted compared to the corresponding spectra of polymer solution, which is attributed to the increasing of molecular interactions between neighbouring molecules in the film state compared to the solution. The absorption and emission spectrums obtained for PFO, F8BT, F8T2, MDMO-PPV and P3HT using THF, or $CHCl_3$ for PFO, and CB as solvent, correspond with the features of the literature about them.

The influence observed in the PL spectra of the micropillars, compared to the corresponding film, is not very significant. But in nanopillars, the effect of the structure starts to be increased.

Polymer nanopillars prepared by different experimental process and solvents of different boiling points were compared, although F8T2 was only studied using THF.

Using THF or $CHCl_3$ as solvents, the increasing of relative intensity of lower wavelength peaks appears in PFO, F8BT, MDMO-PPV and P3HT polymer nanopillars compared to the corresponding film. Similar effect was observed in nanopillars prepared from CB.

In F8BT, MDMO-PPV and P3HT samples prepared by spin-coating, the effect of the nanostructure has less importance, due to the great influence of the experimental process on the photoluminescence spectrum. In contrast, PFO nanopillars increase slightly the intensity of the higher wavelength peak compared to the film. In all cases, the spin-coating process also increases the relative intensity of lower wavelength peaks compared to samples prepared by wetting-based method.

The results indicate that the nanostructure influences the PL spectrum of PFO, F8BT, MDMO-PPV and P3HT, but the effect in the PL spectra also depends on the solvent and the experimental process, specially when the experimental process is the spin-coating method.

The increasing of the relative intensity of lower wavelength peaks could be related with the reduction of interaction between the polymer chains. This produces an increase of the energy gap, leading to a blue-shift of the PL spectrum. This could mean that the degree of isolation of the polymer chains increases in the nanopores compared to the corresponding film.

Chapter 6

X-Ray diffraction and Raman spectroscopy

In Chapter 5, the UV-Vis absorbance and photoluminescence characterization of polymer structures has been performed. Other techniques can be interesting depending on the properties involved in some applications.

Herein, we developed the X-ray diffraction (XRD) technique to study the crystallographic state of the samples. XRD measurements were performed for polymer micro- and nanopillars, prepared by wetting-assisted method using THF, or $CHCl_3$ for PFO, as solvent, in order to compare the crystallographic structure of the film and micro- and nanostructures.

X-ray experiments can characterize the molecular alignment but they are typically conduced on fibres or thick films. These studies add an ambiguity when the results are to be utilized to interpret thin-films properties. Polarized

Raman measurements have been demonstrated to be well suited to this task [116, 117].

Polarized Raman spectroscopy is a powerful technique to investigate the conformation of the polymer chains in nanostructures. By this reasons, all polymer nanopillars prepared by wetting-assisted method, using solvents of different boiling points, and by spin-coating process were measured and compared.

6.1. X-Ray diffraction

The X-ray diffraction (XRD) is a well-known and non-destructive technique that provides information about the crystallographic structure of the studied samples [118]. In the XRD patters, the lattice constant (*d*) corresponding to a peak at 2θ can be calculated using the Bragg's law:

$$2d \sin\theta = n\lambda \qquad \text{(eq. 6.1)}$$

where λ is the wavelength of the incident beam, 2θ is the angle between the incident beam and the scattered X-ray wavevector, and n is the interference order.

In this work, these measurements have been preformed by out-of-plane incidence that means that the detector rotates horizontally with respect to the sample, as is shown in Fig. 6.1. Grazing incident X-ray diffraction (GIXRD) measurements were made using a Bruker-AXS D8-Discover diffractometer. More detailed information is presented in Appendix A.

UNIVERSITAT ROVIRA I VIRGILI
FABRICATION AND CHARACTERIZATION OF POLYMER MICRO- AND NANOSTRUCTURES
BY TEMPLATE-BASED METHOD
Raquel Palacios Higueras
ISBN:978-84-693-9440-3/DL:T.63-2011

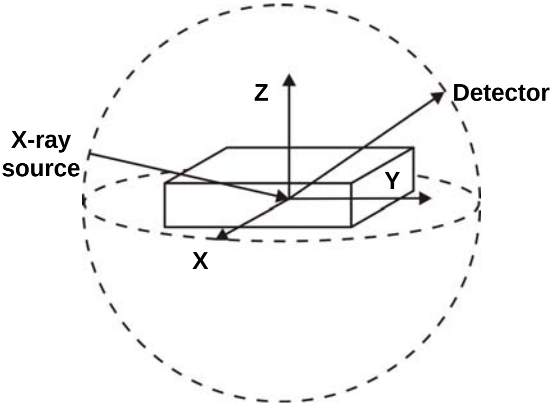

Fig. 6.1. Schematic of grazing incident X-ray diffraction setup for out-of-plane measurements.

6.1.1. Polymer micro- and nanopillars characterization

The samples studied by XRD technique were micro- and nanopillars obtained by wetting-assisted method using THF, or $CHCl_3$ for PFO, as solvent. These polymer structures were also characterized by photoluminescence in Chapter 5.

Fig. 6.2-6.4 show XRD measurement performed for PFO, P3HT and F8BT film, micro- and nanopillars.

The XRD pattern of PFO film and structures are shown in Fig. 6.2. The peaks appeared at 2θ of 7° and at about 21.15° for PFO film and micropillars, and at 2θ of 7.00° and 21.10° for PFO nanopillars. The peak at 7.0 degrees corresponds to (200) plane, which is in agreement with the XRD peak of the β-phase PFO [41, 42, 119].

For P3HT, different peaks appeared at 2θ of 16.9º, 23.2º and 24.1º which correspond to plane separations of 5.2 Å, 3.8 Å and 3.7 Å, respectively (Fig. 6.3). These plane separations agree with the literature about P3HT which correspond to (300) and (101) planes. As well, a broader peak appeared at 5º, which could be due to (100) plane [24, 118].

F8BT, F8T2 and MDMO-PPV seem amorphous materials due to no narrow peaks appeared in their XRD patterns [51, 120]. As example of an amorphous polymer, the result of the F8BT film, micro- and nanopillars is shown in Fig. 6.4. A broad feature appears at about 5º in the nanopillars that could means that the nanostructure had induced some degree of crystallinity

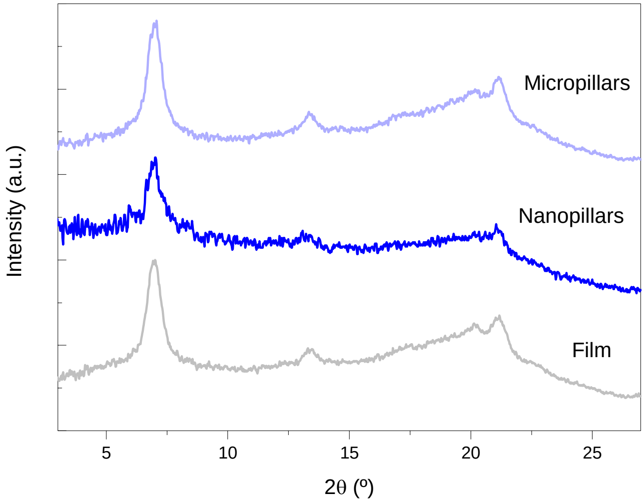

Fig. 6.2. X-ray diffraction patterns of PFO film, micro- and nanopillars (curves are offset for clarity).

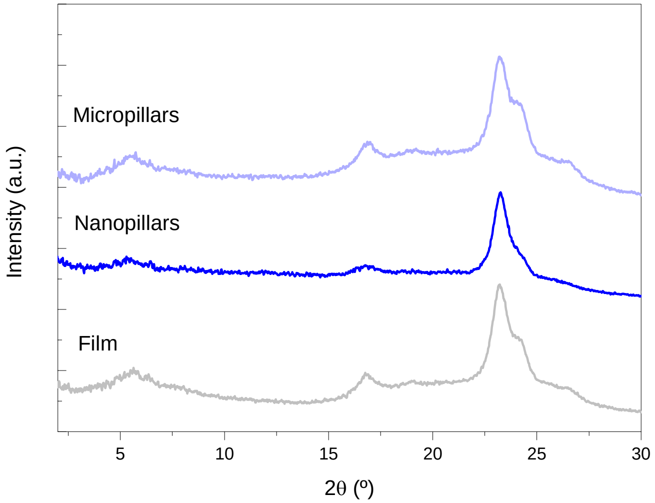

Fig. 6.3. X-ray diffraction patterns of P3HT film, micro- and nanopillars (curves are offset for clarity).

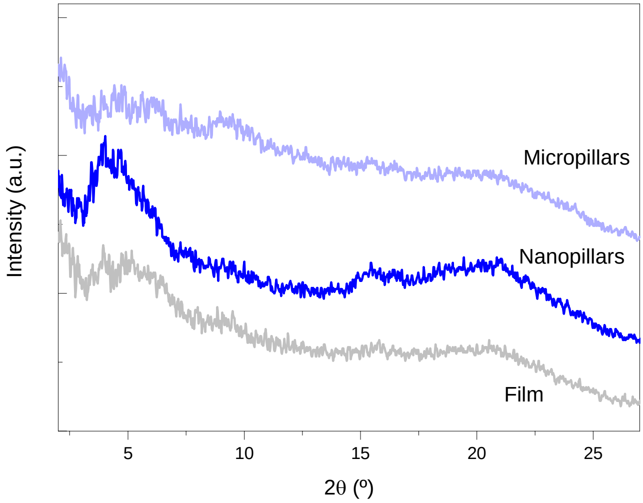

Fig. 6.4. X-ray diffraction patterns of F8BT film, micro- and nanopillars (curves are offset for clarity).

The results indicate that the structure does not modify the crystallinity degree of the samples. P3HT and PFO samples present some peaks due to the crystallographic planes in their structure. PFO patterns provide additional evidence about the presence of PFO β-phase in the samples prepared.

The wetting-based infiltration does not involve any melting of the polymers. For this reason, the crystallographic structure of the sample could not be modified considerably.

6.2. Raman spectroscopy

In recent years, polarized Raman spectroscopy has been considered a powerful technique in order to investigate the vibrational modes of samples, such as the conformation of conjugated polymer nanostructures. Polarized Raman measurements have been demonstrated to be well suited to study the chain conformation and, as the Raman spectra are recorded in reflection geometry, the technique can also allow direct analysis of the alignment in non-transparent device structures. This technique is not destructive and samples do not require any special preparation in order to study their polymer chains conformation which is directly relevant to opto-electronic devices [116, 121]. Raman studies can provide structural information on conjugated polymers, necessary for understanding of optical and electronic properties and the development of devices in which they are used as active layers.

A study of Raman scattering in polyfluorenes, such as PFO, F8BT and F8T2, is particularly useful in resolving ambiguities regarding chain conformations and crystalline phases. Both the vibrational frequencies and intensities determined by Raman spectroscopy are strongly influenced by variations in the backbone as well as side-chain conformations [122]. Raman spectrum of polyfluorenes is characterized by numerous intramolecular C−C/C−H stretch and bend modes spanning from 100 cm^{-1} to 1600 cm^{-1}.

In this work, all the polarized Raman spectra of the polymer samples have been recorded with a Renishaw Raman Imaging Microscope. More detailed information is shown in Appendix A.

6.2.1. Polymer nanopillars characterization

We studied on the Raman spectrum the effect of the polymer chain conformation of the film and nanostructures studied in section 5.2.2., using the same nomenclature **A**, **B** and **C**. Then, the influence of the nanostructure compared to the corresponding film, the solvent used and the experimental process was investigated. Polarized Raman measurements were obtained using excitation laser wavelengths 514 nm for P3HT and 785 nm for PFO, F8BT, F8T2 and MDMO-PPV. The excitation laser beam was polarised parallel to the nanopillars or, in other words, perpendicular to the film. Raman signal was measured polarised parallel and perpendicular to the nanopillars. Fig. 6.5 presents a scheme of polarizations in the experimental measurements.

The ratio between the parallel ($I_{\parallel}$) and perpendicular ($I_{\perp}$) Raman contribution was also studied in order to obtain a quantification of the relative intensities.

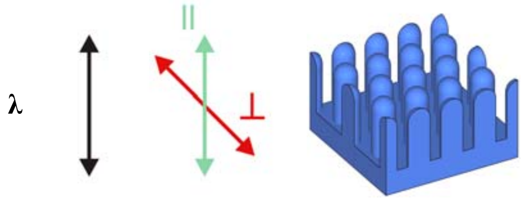

Fig. 6.5. Scheme of the polarized Raman spectroscopy measurements. The incident laser beam (black arrow), with λ wavelength, was polarised parallel to the nanopillars, and, in reflection geometry, detections were polarised parallel (green arrow) and perpendicular (red arrow) to the laser beam.

Fig. 6.6 shows the Raman intensities measured from PFO samples **A**, **B** and **C**. PFO spectrum is dominated by a strong peak at 1603 cm^{-1}, which is assigned to the phenyl intra-ring C−C stretch mode [43, 123]. We observed that the intensity of the signal polarized parallel to the excitation is higher than that polarized perpendicular when the spectra is acquired for PFO nanopillars **A** ($I_\perp/I_\parallel \sim 0.1$) whereas, in film **A**, the perpendicular Raman intensity is higher than the parallel one ($I_\parallel/I_\perp \sim 0.7$). In film **B**, the parallel Raman signal is slightly higher than the parallel one ($I_\perp/I_\parallel \sim 0.9$). In nanopillars **B**, the difference between the parallel and perpendicular contribution increases with a more intense perpendicular Raman signal ($I_\parallel/I_\perp \sim 0.6$). In addition, nanopillars and film **C** exhibit a higher perpendicular Raman intensity than parallel one ($I_\parallel/I_\perp \sim$ 0.8-05). These Raman spectra indicate that the chains of the polymer are mainly parallel to the pillars in the nanostructure **A**, but in the film **A** the chains are not aligned with respect to the nanopillars. When CB is used as solvent, the Raman measurements illustrate that the polymer chains present a preferential direction perpendicular to the pillars. The results mean that the direction of the polymer chains is affected by the spin-coating process.

As Fig. 6.7 shows, F8BT spectrum exhibits two strong peaks at 1608 cm^{-1}, which corresponds to the F8 ring stretching mode, and at 1545 cm^{-1} corresponding to the BT ring stretching mode, as well as the mode at 1357 cm^{-1} which corresponds to the two carbon atoms in the thiadiazole unit [121]. Similar parallel and perpendicular Raman intensities were measured for F8BT film and nanopillars **A** ($I_\perp/I_\parallel \sim 0.9$), which reveals that no preferential direction appears due to the polymer chains contributions. In film **B**, perpendicular Raman intensity is higher than the parallel Raman intensity ($I_\parallel/I_\perp \sim 0.4$) and, in nanopillars **B**, the difference between the Raman signal parallel and perpendicular increases slightly ($I_\parallel/I_\perp \sim 0.3$). These results can be due to the higher boiling point of CB (132 ºC) compared to the boiling point of THF (65-

67 ºC), which can influence in the conformation of the polymer chains. In addition, perpendicular Raman spectra of film and nanopillars **C** ($I_{\parallel}/I_{\perp} \sim 0.6$ and 0.3, respectively) present higher intensity than parallel Raman spectra, which means that spin-coating process increases the polymer chains in the perpendicular direction.

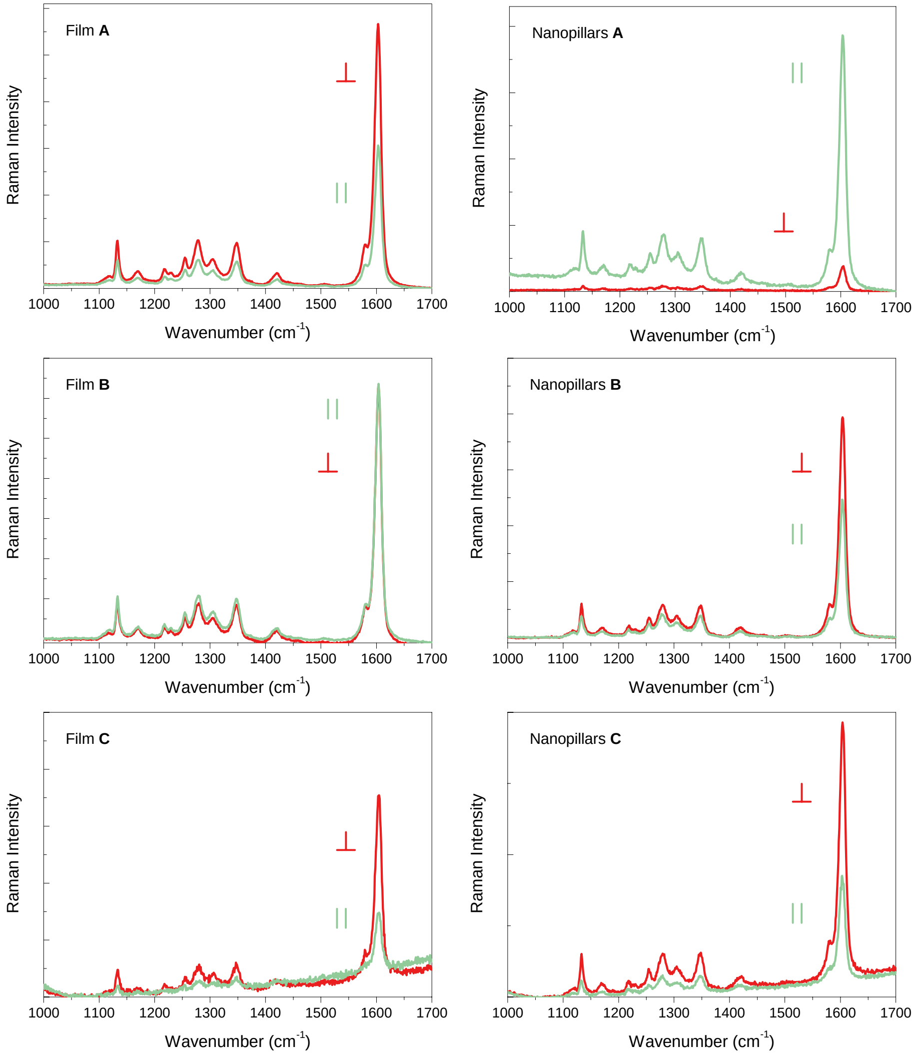

Fig. 6.6. Parallel (green line) and perpendicular (red line) Raman intensity of PFO films and nanopillars prepared from different experimental processes (**A**, **B** and **C**).

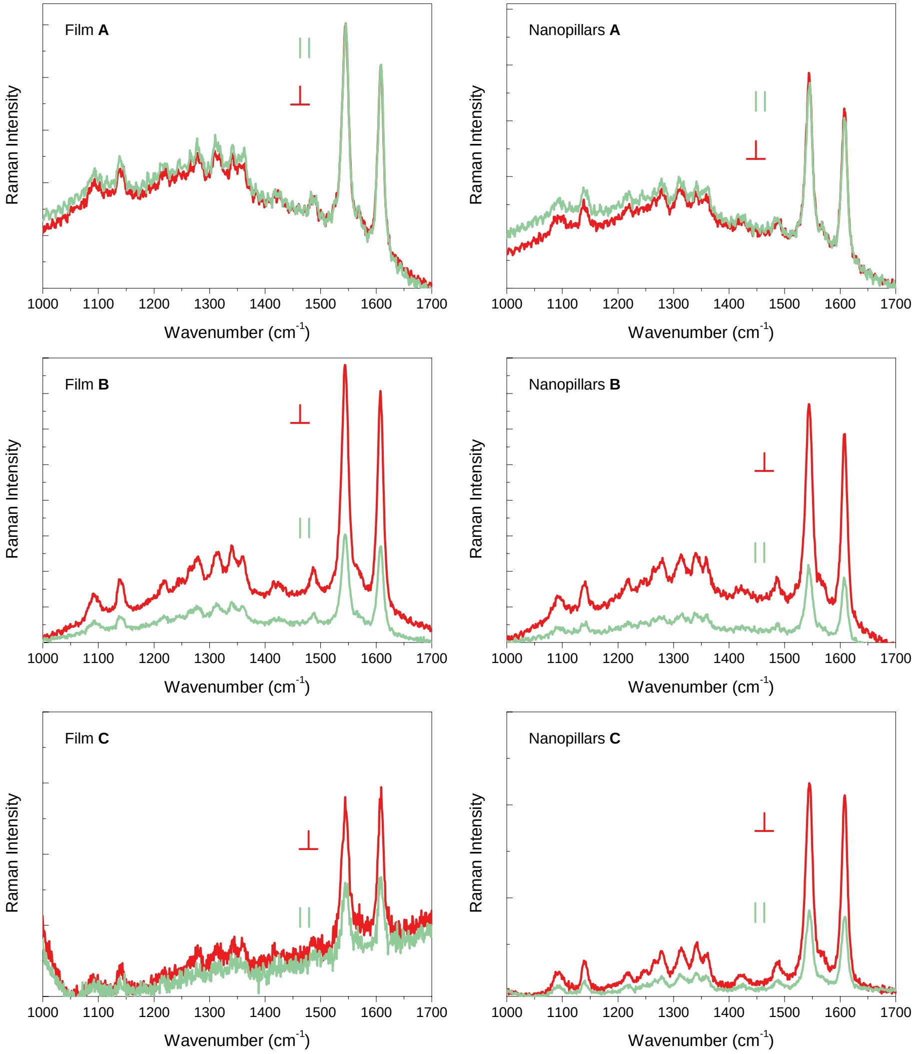

Fig. 6.7. Parallel (green line) and perpendicular (red line) Raman intensity of F8BT films and nanopillars prepared from different experimental processes (**A**, **B** and **C**).

Raman measurements of F8T2 were only carried out for film and nanopillars **A**, due to F8T2 is not soluble in CB. As is shown in Fig. 6.8, Raman spectrum of F8T2 exhibit two strong peaks at 1457 and 1495 cm^{-1}, which are attributed to stretching modes involving the thiophene rings, and other peak at

1604 cm^{-1} corresponding to the in-plane stretching mode of the fluorene moiety [116]. In film and nanopillars, the perpendicular Raman contribution is more intense than the parallel contribution. However, the relative intensity between parallel and perpendicular contributions indicates that the parallel signal is more important in the nanopillars ($I_{\parallel}/I_{\perp} \sim 0.6$) than in the film ($I_{\parallel}/I_{\perp} \sim 0.4$). These results mean that the nanostructure modifies the preferential direction of the polymer chains.

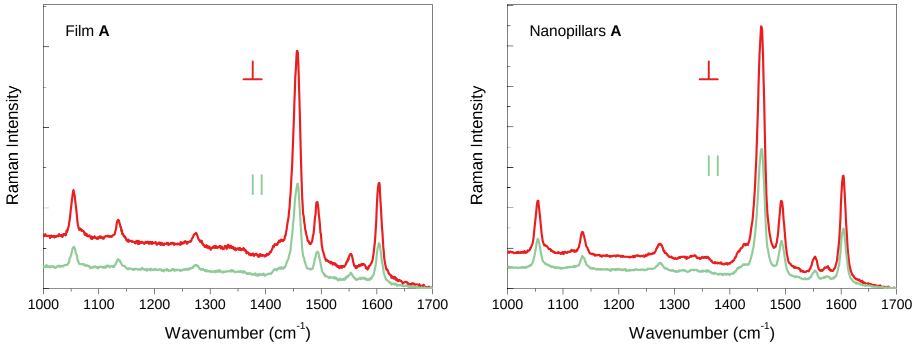

Fig. 6.8. Parallel (green line) and perpendicular (red line) Raman intensity of F8T2 films and nanopillars prepared from experimental processes **A**.

Fig. 6.9 shows the Raman intensities measured from MDMO-PPV samples **A**, **B** and **C**. MDMO-PPV spectrum exhibits peaks at 1582 cm^{-1} and 1282 cm^{-1}, which are assigned to the C=C stretching band of benzene ring, and a peak at 1112 cm^{-1}, which correspond to mixtures of C−C stretching and C−H in plane-bending vibration and C−C. Also, a peak at 1623 cm^{-1} appears due to the C=C stretching band of vinyl group [124]. Raman spectra of MDMO-PPV film **A** exhibit similar parallel and perpendicular intensities ($I_{\parallel}/I_{\perp} \sim 1$), whereas in nanopillars **A** the parallel Raman intensity is a bit higher than the perpendicular one ($I_{\perp}/I_{\parallel} \sim 0.8$). In film **B**, the perpendicular Raman intensity is higher than the parallel one ($I_{\parallel}/I_{\perp} \sim 0.7$) whereas, in nanopillars **B**, the parallel Raman spectrum has higher intensity than perpendicular one ($I_{\perp}/I_{\parallel} \sim 0.7$). Film and nanopillars **C** Raman spectra are modified by the spin-coating process, which increases the perpendicular Raman intensity in both film and nanopillars **C** ($I_{\parallel}/I_{\perp}$ ~ 0.4 and 0.2, respectively). In samples **A** and **B**, the results mean that the nanostructure increases the polymer chains parallels to the nanopillars and spin-coating process increases the polymer chains in the perpendicular direction.

Fig. 6.10 shows the Raman intensities measured from P3HT film and nanopillars **A**, **B** and **C**. P3HT spectrum is dominated by a strong peak at 1450 cm^{-1}, which can be attributed to the symmetric C=C stretching deformation. In addition, a peak at 1375 cm^{-1} appears due to the C−C stretching deformations in the aromatic thiophene ring [56]. In films **A** and **B**, parallel Raman intensities are higher than perpendicular ones ($I_{\perp}/I_{\parallel}$ ~ 0.8), which means that the solvent does not influence considerably the Raman spectra. In nanopillars **A** and **B**, the parallel Raman signal is also more intense than the perpendicular one with a ratio similar to the film ($I_{\perp}/I_{\parallel}$ ~ 0.8). In film and nanopillars **C**, parallel Raman intensities are also higher than the perpendicular Raman intensities, but the perpendicular Raman signals are vaguely increased ($I_{\perp}/I_{\parallel}$ ~ 0.9). These results mean that the solvent and the nanostructure do not modify considerably the polymer chain conformation, and the spin-coating process increases slightly the perpendicular Raman intensity.

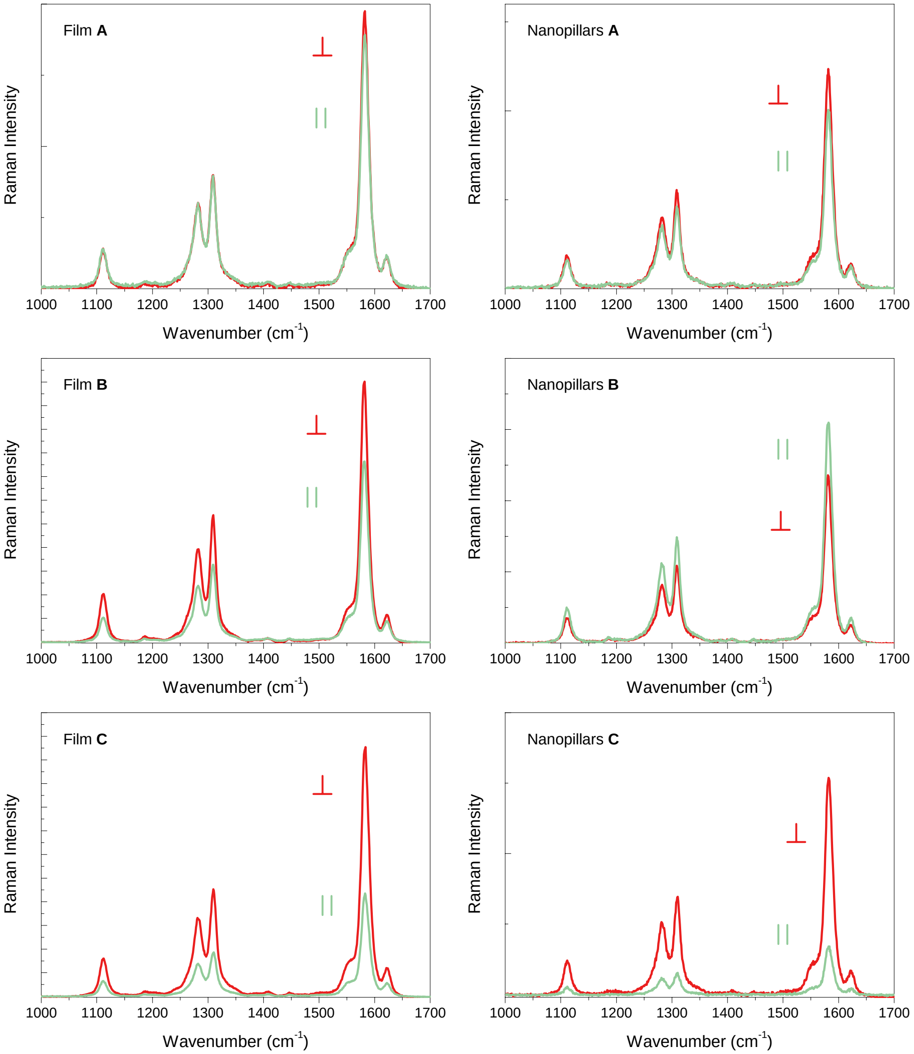

Fig. 6.9. Parallel (green line) and perpendicular (red line) Raman intensity of MDMO-PPV films and nanopillars prepared from different experimental processes (**A**, **B** and **C**).

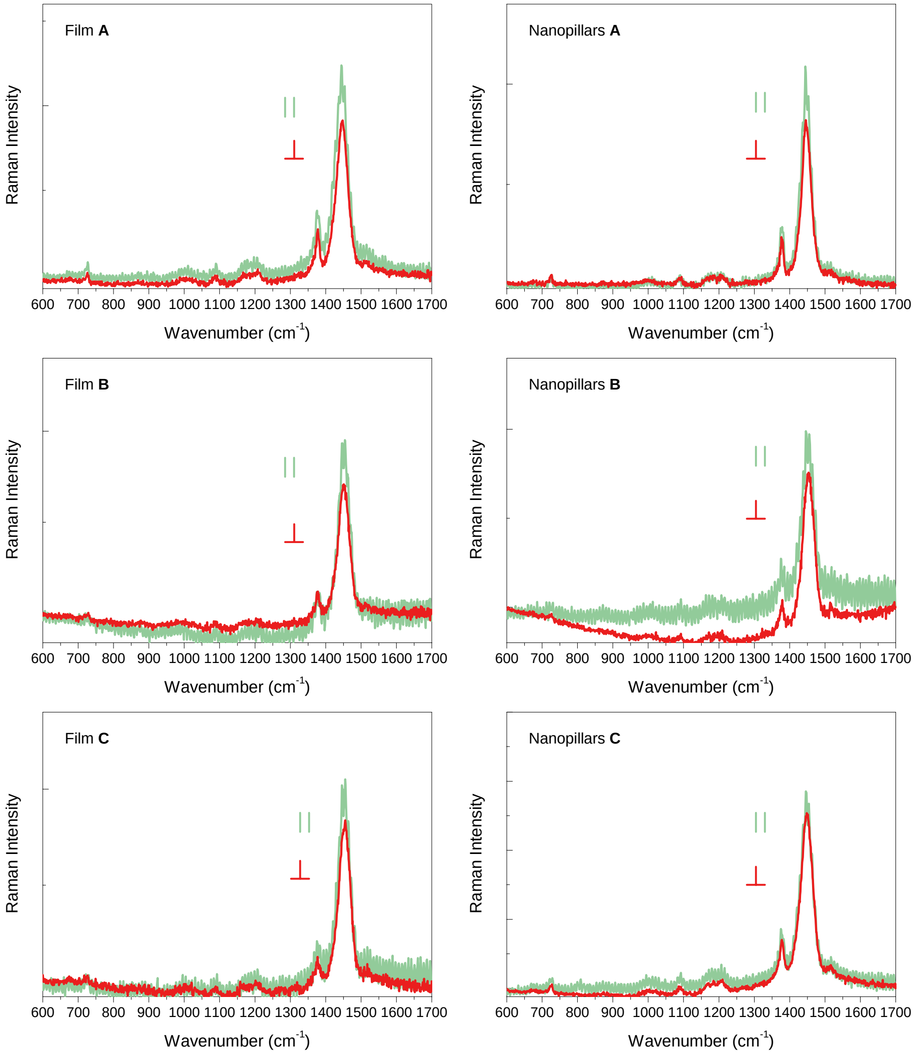

Fig. 6.10. Parallel (green line) and perpendicular (red line) Raman intensity of P3HT films and nanopillars prepared from different experimental processes (**A**, **B** and **C**).

The study of the polymer chains conformation by polarized Raman spectroscopy reveals that the influence of the solvent and the nanostructure is higher in some polymers and the Raman measurements can be non-affected by these conditions.

In PFO nanopillars, Raman intensities are dependents of the nanostructure prepared from $CHCl_3$ solution. In this conditions, the measurements reveals that the parallel Raman intensity is higher than the perpendicular Raman intensity whereas, in the film prepared from $CHCl_3$ solution, the perpendicular Raman signal is more intense than the parallel one. An increasing of the parallel Raman signal compared to the perpendicular one also occurs in F8BT nanopillars prepared from CB solution, in F8T2 prepared from THF solution and in MDMO-PPV nanopillars prepared from both THF and CB solutions, all of them compared to the corresponding film. These results indicate that in these polymers the nanostructure increases the polymer chains parallel to the nanopillars. In contrast, PFO nanopillars, prepared from CB solution, present a higher perpendicular Raman signal than the film, which means that, in the nanostructure, the preferential direction perpendicular to the nanopillars is increased. Furthermore, the Raman measurements of F8BT samples, prepared from THF solution, and P3HT samples, prepared from both THF and CB, are not modified by the nanostructure.

Finally, the experimental process can influence considerably the polymer chain conformation the both film and nanopillars. When PFO, F8BT and MDMO-PPV samples were prepared by spin-coating, the perpendicular Raman contribution is more intense than the parallel one, which means that this experimental process modifies the polymer chain conformation. In contrast, for P3HT samples parallel Raman intensity is higher than the perpendicular one, but the perpendicular Raman contribution increases slightly due to the spin-coating process.

6.3. Conclusions

In this chapter, we have developed different techniques for the characterization of the polymer structures. The X-ray diffraction (XRD) provided the study of the crystallinity degree of the samples. Polarized Raman spectroscopy investigated the conformation of the polymer chains, especially for nanopillars.

In order to compare the crystallinity degree of the polymer film, micro- and nanopillars, XRD patterns of polymer samples, prepared by wetting-based method using THF, or $CHCl_3$ for PFO, as solvent were recorded. The results indicate that the experimental process and the structure do not influence the crystallinity degree of the polymer. F8BT, F8T2 and MDMO-PPV samples presented an amorphous nature. In contrast, the peaks at P3HT and PFO XRD patterns indicate the presence of some degree of crystallinity. As well, PFO patterns with a peak at 7º demonstrate the presence of PFO β-phase in the samples prepared.

As Raman spectroscopy is a powerful technique to study nanostructures, polymer nanopillars prepared by wetting-based method, using two different solvents, and by spin-coating process were characterized. These measurements revealed that the influence of the solvent and the nanostructure is higher in some polymers whereas, in some cases, Raman measurements are not affected by these conditions.

In PFO nanopillars prepared from $CHCl_3$ solution, the polymer chains present a preferential direction parallel to the nanopillars due to the nanostructure.

Using THF as solvent, F8BT sample is not affected by the nanostructure. In F8T2 and MDMO-PPV nanopillars, the polymer chains with a preferential direction parallel to the nanopillars increase compared to the corresponding film.

Using CB as solvent, PFO nanopillars present an increasing of polymer chains perpendicular to the nanopillars compared to the PFO film. In F8BT nanostructure, polymer chains parallel to the nanopillars increases compared to the film, although the preferential direction in both film and nanostructure is perpendicular to the nanopillars. In MDMO-PPV, polymer chains in the nanostructure are preferentially aligned in the direction of the nanopillars, whereas in the film the preferential direction is perpendicular to the nanopillars.

In addition, PFO, F8BT and MDMO-PPV samples prepared by spin-coating present a perpendicular Raman contribution more intense than the parallel one, which means that this experimental process modifies the polymer chains conformation in the direction perpendicular to the nanopillars.

P3HT samples are slightly affected by the nanostructure, solvent and the spin-coating process. In all cases, the P3HT polymer chains do not have a clear preferential direction.

These effects in the polymer chain conformation should be taken into account in order to develop applications.

Chapter 7

Summary and conclusions

The work presented in this thesis concerns the following subjects: fabrication of porous materials in order to be employed as templates, the preparation of polymer micro- and nanostructures by template-assisted technique using different experimental processes and polymers, and the characterization of the obtained structures.

Since the potential applications of the polymer structures are related to their dimensions, the study of the template fabrication with the desired dimensions should be taken into account in order to develop polymer structures by template-assisted technique. Porous materials of different dimensions and disordered or ordered in a large scale have been prepared. The desired pore diameter and depth can be adjusted in the corresponding scale by the processes explained.

The process to prepare macroporous silicon by the electrochemical etching of silicon in HF solution has been detailed. Disordered macroporous silicon has a high dispersion in pore diameter and depth due to the pore growth starts randomly. Ordered macroporous silicon entails the pattern of the silicon surface before the electrochemical etching. The fabrication of porous silicon has been demonstrated useful to obtain micro-templates. Macroporous silicon with pore depth from 2 to 150 µm and pore diameter from 1 to 2 µm has been employed as template.

Furthermore, in the nanoscale, self-ordered porous alumina has been presented as candidate for nano-template. The self-order effect can be obtained by two-step anodization in acid solution. The obtained structure has a hexagonal array of pores. Self-ordered nanoporous alumina templates, prepared using oxalic or phosphoric acid, have been obtained with pore depth from 150 nm to 3 µm and pore diameter from 55 to 250 nm.

Using these porous templates, we have presented the template-assisted technique using different experimental process in order to obtain polymer micro- and nanostructures. First, the vacuum-based method was developed infiltrating a polymer solution into the template. Second, the melt-assisted process, which entails the annealing of the polymer at a temperature above its melting point, has been studied. Then, the wetting-based method appears as the easiest experimental process in order to prepare polymer structures. This method entails the infiltration of a polymer solution at ambient conditions. Finally, as the spin-coating process is well known to prepare nanodevices in different areas, polymer nanopillars were also obtained by this process. Using these processes, polymers from different chemical families have been infiltrated.

PMMA micro- and nanostructures were obtained under vacuum and P3HT micro- and nanostructures were prepared by melting the polymer. To develop the wetting-based method without solvent, PDMS microfibres were prepared but the fabrication of micropillars was not possible due to the properties of PDMS. By this method, using PFO, F8BT, F8T2, MDMO-PPV and P3HT solutions, polymer micro- and nanostructures were obtained. The free-standing nanopillars prepared from chlorobenzene (CB) solution were better formed than the nanopillars prepared from tetrahydrofurane (THF) or chloroform ($CHCl_3$) in the case of PFO. Finally, due to the evaporation ratio during the process, the solvent used for the spin-coating process was CB. By this method, PFO, F8BT, MDMO-PPV and P3HT nanopillars were obtained. F8T2 nanopillars were not prepared because F8T2 in not soluble in CB.

The obtained polymer micro- and nanostructures have many potential applications in devices of different areas. Depending on particular application, polymer, structure and experimental process should be selected and improved.

The photoluminescent polymers (PFO, F8BT, F8T2, MDMO-PPV and P3HT) employed to prepare micro- and nanostructures can be optically characterized. Polymer solutions and film, prepared from the different solvents, were studied by the UV-Vis absorbance and photoluminescence (PL). The results indicate that polymer films are red-shifted compared to the corresponding spectra of polymer solution which is attributed to the increasing of molecular interactions between neighbouring molecules in the film state compared to the solution. As well, the absorbance of the PFO film demonstrates the presence of the PFO β-phase.

Microstructures prepared by wetting-based method were also characterized. The influence measured in the PL spectra of the micropillars, compared to the corresponding films, is not very significant. In contrast, in polymer nanostructures, the influence in the optical properties of the polymers has been demonstrated. Polymer nanopillars prepared by different experimental process and solvents of different boiling points were compared, although F8T2 was only studied using THF.

By wetting-based method using THF or $CHCl_3$, the lower wavelength peak intensities increase in PFO, F8BT, MDMO-PPV and P3HT nanopillars compared to the corresponding film. This effect was also observed in the samples prepared using CB. Furthermore, in samples prepared by spin-coating, the effect of the nanostructure has less importance, due to the great influence of the experimental process on the photoluminescence spectrum. In all cases, the spin-coating process also increases the relative intensity of lower wavelength peaks compared to samples prepared by wetting-based method. The results indicate that the PL spectra of PFO, F8BT, MDMO-PPV and P3HT are influenced by the nanostructure, but the shifted in the PL spectra also depends on the solvent and experimental process.

The relative intensity of lower wavelength peaks could increase due to the reduction of interaction between the polymer chains. This could means that the degree of isolation of the polymer chains increases in the nanopores compared to the corresponding film.

Furthermore, X-ray diffraction and polarized Raman spectroscopy were employed to characterize the polymer structures. X-ray diffraction (XRD) patterns of polymer samples, prepared by wetting-based method using THF, or $CHCl_3$ for PFO, as solvent, were recorded in order to compare the crystallinity degree of the polymer film, micro- and nanopillars. The results indicate that the experimental process and the structure do not influence the nature of the polymer. The peaks at their XRD patterns indicate that P3HT and PFO present some degree of crystallinity. As well, PFO patterns with a peak at 7º demonstrate the presence of PFO β-phase in the samples prepared.

As polarized Raman spectroscopy is a powerful technique to study nanostructures, polymer nanopillars prepared by wetting-based method, using two different solvents, and by spin-coating process were characterized. These measurements revealed that the influence of the solvent and the nanostructure is higher in some polymers.

From $CHCl_3$ solution, PFO nanopillars present polymer chains with a considerably preferential direction parallel to the nanopillars due to the nanostructure, which does not appear in the corresponding film. When THF is used as solvent, F8BT samples are not affected by the nanostructure and the polymer chain preferential direction is not clear. In F8T2 and MDMO-PPV nanopillars, the polymer chains with a preferential direction parallel to the nanopillars increase compared to the corresponding film.

From CB solution, PFO nanopillars present more polymer chains perpendicular to the nanopillars than the PFO film. Although the preferential direction in both F8BT film and nanostructure is perpendicular to the nanopillars, in nanostructure, polymer chains parallel to the nanopillars increases compared to the film. In MDMO-PPV film, the preferential direction of the polymer chains is perpendicular to the nanopillars, whereas, in the nanostructure, the preferentially direction is parallel to the nanopillars.

In all PFO, F8BT, and MDMO-PPV nanopillars prepared by spin-coating, the polymer chains have preferentially the direction perpendicular to the nanopillars. These results indicate that this experimental process modifies the polymer chains conformation in the perpendicular direction.

In all P3HT samples, polymer chains have not a clear preferential direction. The measurements of samples prepared by spin-coating process indicate that the polymer chains perpendicular to the nanopillars are slightly increased by this process.

To conclude, micro- and nanostructures, prepared from polymers of different chemical families, have been obtained by template-assisted technique with suitable experimental processes. The polymer structures obtained have been characterized. The template-assisted technique does not required specialized equipment and is applicable to a wide range of materials. The results obtained show that this technique is powerful and provides structures with many potential applications. For each application, the desired dimensions and morphology, such as the order or free-standing, of the polymer structure can be prepared selecting the adequate template. The results show that depending on the desire structure and the polymer selected, the experimental process should be selected or improved for the particular application. Further work is needed to develop polymer micro- and nanostructures for applications using the conditions studied in this work. These polymer micro- and nanostructures have many potential applications in different areas, such as PLEDs, sensors and opto-electronic devices.

Appendixes

Appendix A. Characterization techniques

The techniques employed for studying the templates and the polymer structures prepared in this thesis are presented in this appendix. Scanning electron microscopy was carried out for morphology studies, UV-Vis absorbance and photoluminescence for optical characterization, X-ray diffraction for crystallinity studies and polarized Raman spectroscopy for polymer chains conformation [125].

Scanning electron microscopy

Briefly, the scanning electron microscope (SEM) images the electrons that are reflected from a sample. These images are useful for studying surface morphology or measuring sizes. The SEM produces the images by detecting secondary electrons that are emitted from the surface due to the excitation by the primary electron beam. The SEM has great depth of field, so can produce images that are a good representation of the 3D structure of the sample.

All the samples were inspected in environmental scanning electron microscopy (ESEM-FEI Quanta 600) at low vacuum. A gold thin layer was deposited on polymer nanostructures in order to avoid deformations upon heating during ESEM observation. Fig. A. 1 shows a digital photograph of the ESEM employed.

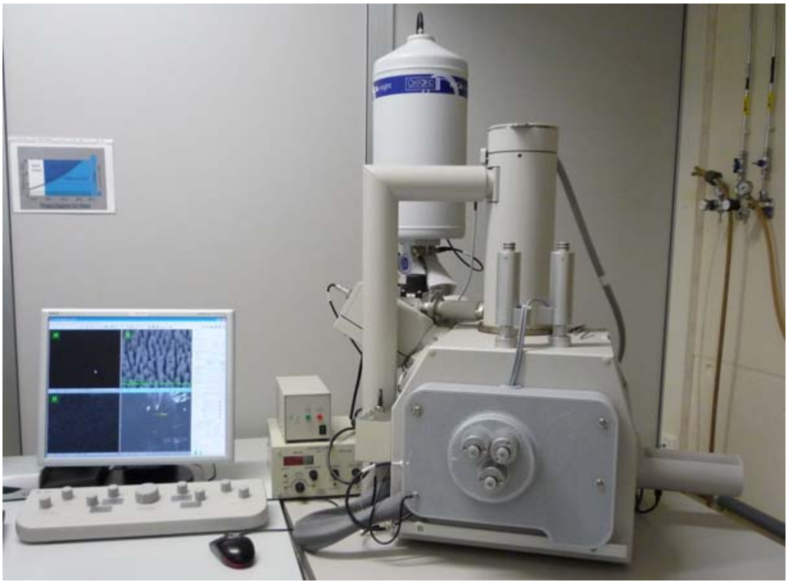

Fig. A. 1. Digital photograph of the environmental scanning electron microscopy (ESEM).

UV-Vis absorbance and photoluminescence

At room temperature, most compounds are in their lowest energy or ground state. Upon interaction with the appropriate type of electromagnetic radiation, characteristic electronic, vibrational and rotational transitions can occur. Excited states thus formed usually decay back to the ground state very quickly, either by the emitting the energy absorbed with the same or lower frequency or by ‘radiationless’ relaxation through heat loss. Infrared radiation causes the vibrations in molecules to increase in amplitude and absorption of visible and ultraviolet radiation cause electrons to move to higher electron orbitals. Molecular spectra can be obtained by measuring the radiation absorbed or emitted by the sample. These phenomena are exploited by spectrometric instruments.

Many molecules absorb ultraviolet (UV) or visible (Vis) radiation. In terms of electromagnetic spectrum, UV radiation covers the region from 190-

350 nm and visible radiation covers the region 350-800 nm. Absorption of UV-Vis radiation corresponds to the excitation of outer electrons in the molecule.

In this thesis, absorption spectra were measured by a double beam UV-Vis Shimadzu spectrophotometer (UV-1700), with a spectral range from 190 to 1100 nm and 1 nm fixed slit. A digital photograph of the spectrophotometer employed is presented in Fig. A. 2.

Luminescence spectrofluorimeter (Aminco-Bowman Series 2), with a system composed by xenon lamps, cuvette and solid sample holder, and a wavelength range from 250 to 850 nm, was employed for measuring the emission spectrum of polymer samples. Fig. A. 3 shows a digital photograph of the spectrofluorimeter used.

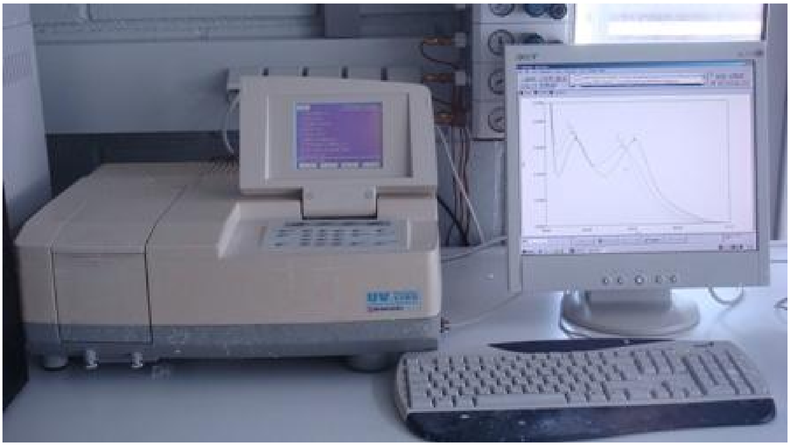

Fig. A. 2. Digital photograph of the UV-Vis spectrophotometer.

UNIVERSITAT ROVIRA I VIRGILI
FABRICATION AND CHARACTERIZATION OF POLYMER MICRO- AND NANOSTRUCTURES
BY TEMPLATE-BASED METHOD
Raquel Palacios Higueras
ISBN:978-84-693-9440-3/DL:T.63-2011

Fig. A. 3. Digital photograph of the luminescence spectrofluorimeter.

X-Ray diffraction

X-Ray diffraction (XRD) is a non-destructive technique that operates on the nanometer scale based on the elastic scattering of X-rays from structures that have a long range order. In a typical experiment, the sample is hit with X-rays and the intensity of the X-rays diffracted from the sample is recorded as a function of angular movement of both the detector and the sample. By this technique, information such as spacing in the crystal lattice, bond lengths and angles and purity, can be obtained.

Grazing incident X-ray diffraction (GIXRD) measurements were made using a Bruker-AXS D8-Discover diffractometer equipped with parallel incident beam (Göbel mirror), vertical θ-θ goniometer, XYZ motorized stage and with a GADDS (General Area Diffraction System). Polymer samples were held in a circular sample holder for transmission mode and the area of interest was selected with the aid of a video-laser focusing system. An X-ray collimator system combined with a direct beam stop of 4 degrees of aperture, allows to

UNIVERSITAT ROVIRA I VIRGILI
FABRICATION AND CHARACTERIZATION OF POLYMER MICRO- AND NANOSTRUCTURES
BY TEMPLATE-BASED METHOD
Raquel Palacios Higueras
ISBN:978-84-693-9440-3/DL:T.63-2011

analyse areas of 500 µm. The X-ray diffractometer was operated at 40 kV and 40 mA to generate $Cu_{k\alpha}$ radiation. The GADDS detector was 30x30 cm with a 1024x1024 pixel CCD sensor. We collected one frame (2D XRD patterns) in transmission mode at a distance of 15 cm from the sample. These measurements were preformed by out-of-plane incidence that means that the detector rotates horizontally with respect to the sample.

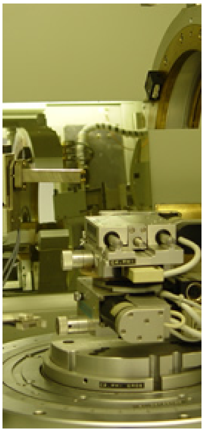

Fig. A. 4. Digital photograph of the diffractometer.

Raman spectroscopy

Raman is a scattering method that is useful for providing structural information about molecules in terms of their functional groups, the orientation of those groups and the information on isomers. It can be used to examine most kind of sample and is non-destructive. Raman radiation spans the range 4000 down to about zero cm^{-1}.

The Raman effect arises when incident light distorts the electron density in the molecule, which subsequently scatters the light. A very small proportion of the light is scattered at a different wavelength than the incident light. This inelastic scattered light is called Raman effect. The energy difference between the incident light and the Raman scattered light is equal to the energy involved in getting a molecule to vibrate.

In this work, all the Raman spectra of the polymer samples were recorded with a Raman FT-IR spectrometer (Renishaw), which is shown in Fig. A. 5.

Fig. A. 5. Digital photograph of the Raman spectrometer.

Appendix B. Gaussian functions

Spectrum bands are often very broad and their more or less characteristic shoulders show that the observed bands consist of several overlapping sub-bands. In most cases, the bands to be separated can be approximated by Gaussian functions. This decomposition technique has been widely applied in different spectra [126-128]. The Gaussian functions can be written as follows:

$$y = y_0 + \frac{A}{w\sqrt{\pi/2}} \exp\left(-2 \left(\frac{x - x_c}{w} \right)^2 \right)$$

where y_0 is the baseline offset, x_c is the position of peak value, A is the total area under the curve from the baseline and w is 2 "sigma", approximately 0.849 the width of the peak at half height, and w/2 is the standard deviation.

In Chapter 5, the UV-Vis absorption and photoluminescence (PL) spectra measured were fitted by Gaussian functions in order to be studied and compared. The obtained Gaussian functions are presented in this appendix.

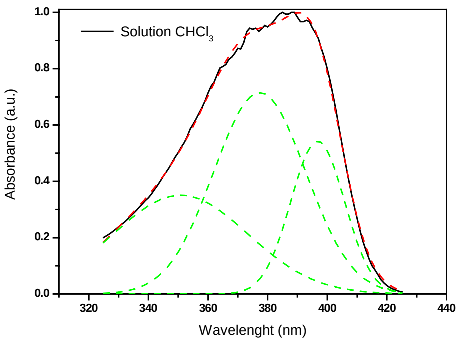

R^2	0.999
y_0	0.00
x_{c1}	350.78
w_1	45.29
A_1	19.89
x_{c2}	377.36
w_2	30.91
A_2	27.69
x_{c3}	396.78
w_3	18.02
A_3	12.26

Fig. B. 1. Gaussian functions for UV-Vis absorption of PFO solution ($CHCl_3$).

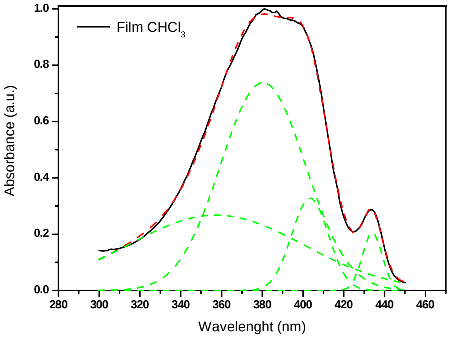

R^2	0.999
y_0	0.00
x_{c1}	357.28
w_1	85.93
A_1	28.83
x_{c2}	380.34
w_2	41.50
A_2	38.40
x_{c3}	403.44
w_3	17.87
A_3	7.38
x_{c4}	434.00
W_4	9.63
A_4	2.51

Fig. B. 2. Gaussian functions for UV-Vis absorption of PFO film ($CHCl_3$).

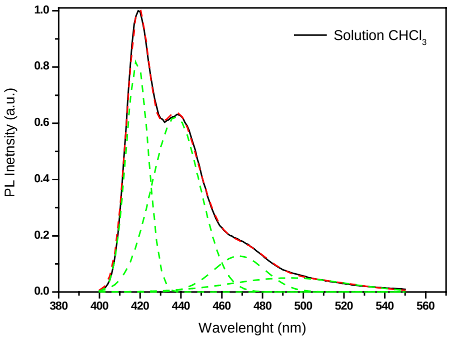

R^2	0.999
y_0	0.00
x_{c1}	418.50
w_1	10.94
A_1	11.30
x_{c2}	437.47
w_2	23.78
A_2	18.60
x_{c3}	468.58
w_3	25.22
A_3	4.05
x_{c4}	493.11
W_4	56.57
A_4	3.54

Fig. B. 3. Gaussian functions for PL of PFO solution ($CHCl_3$).

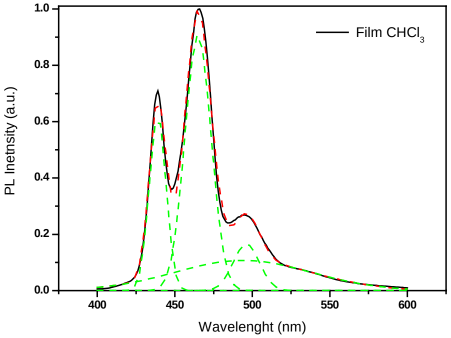

R^2	0.997
y_0	0.00
x_{c1}	438.92
w_1	10.75
A_1	8.43
x_{c2}	464.95
w_2	16.89
A_2	19.23
x_{c3}	496.12
w_3	16.91
A_3	3.52
x_{c4}	494.04
W_4	88.20
A_4	11.85

Fig. B. 4. Gaussian functions for PL of PFO film ($CHCl_3$).

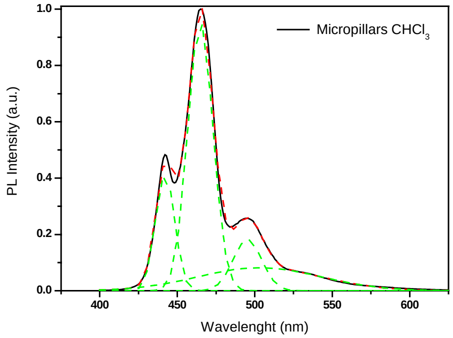

R^2	0.999
y_0	0.00
x_{c1}	442.12
w_1	12.26
A_1	6.43
x_{c2}	464.90
w_2	16.19
A_2	19.42
x_{c3}	495.26
w_3	18.56
A_3	4.22
x_{c4}	503.15
W_4	79.44
A_4	8.14

Fig. B. 5. Gaussian functions for PL of PFO micropillars ($CHCl_3$).

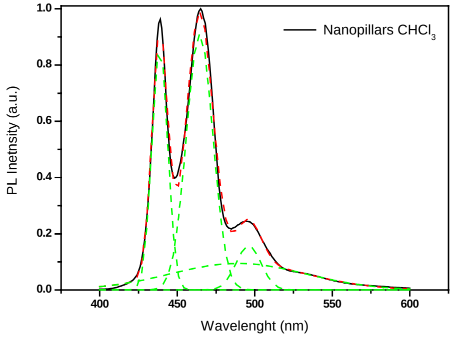

R^2	0.997
y_0	0.00
x_{c1}	438.73
w_1	10.09
A_1	11.00
x_{c2}	464.42
w_2	17.07
A_2	19.48
x_{c3}	496.03
w_3	16.24
A_3	3.19
x_{c4}	489.25
W_4	87.49
A_4	10.38

Fig. B. 6. Gaussian functions for PL of PFO nanopillars ($CHCl_3$).

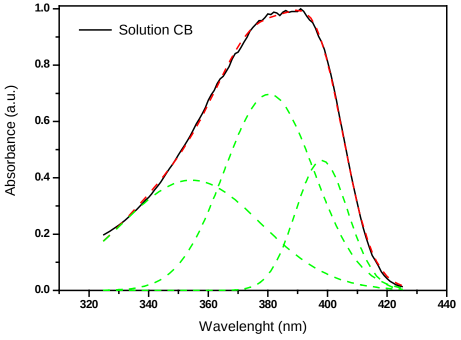

R^2	0.999
y_0	0.00
x_{c1}	354.42
w_1	46.52
A_1	22.84
x_{c2}	380.41
w_2	30.22
A_2	26.41
x_{c3}	398.08
w_3	17.54
A_3	10.17

Fig. B. 7. Gaussian functions for UV-Vis absorption of PFO solution (CB).

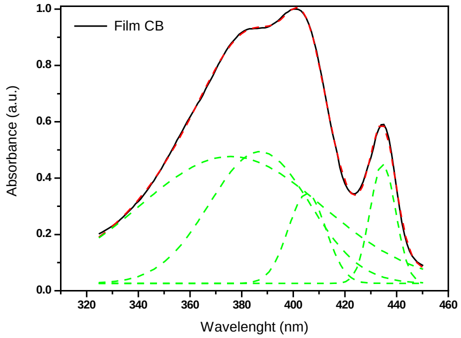

R^2	1.000
y_0	0.03
x_{c1}	375.79
w_1	71.20
A_1	40.21
x_{c2}	386.99
w_2	38.79
A_2	22.75
x_{c3}	405.32
w_3	14.54
A_3	5.83
x_{c4}	434.64
W_4	9.89
A_4	5.29

Fig. B. 8. Gaussian functions for UV-Vis absorption of PFO film (CB).

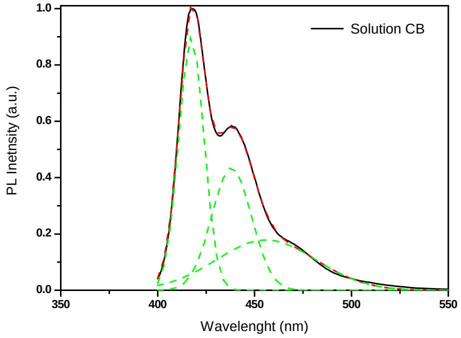

R^2	1.000
y0	0.00
xc1	417.40
w1	13.04
A1	14.68
xc2	438.16
w2	20.54
A2	11.19
xc3	455.92
w3	51.48
A3	11.51

Fig. B. 9. Gaussian functions for PL of PFO solution (CB).

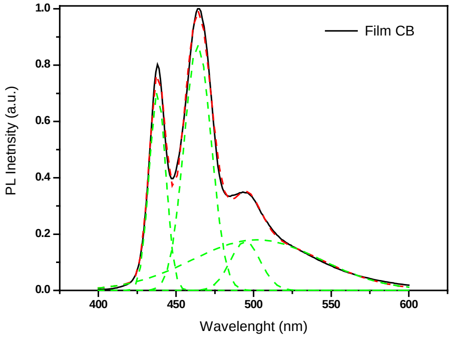

R^2	0.998
y_0	0.00
x_{c1}	438.04
w_1	10.57
A_1	9.40
x_{c2}	463.94
w_2	17.58
A_2	19.23
x_{c3}	494.64
w_3	19.43
A_3	4.24
x_{c4}	502.04
W_4	83.06
A_4	18.70

Fig. B. 10. Gaussian functions for PL of PFO film (CB).

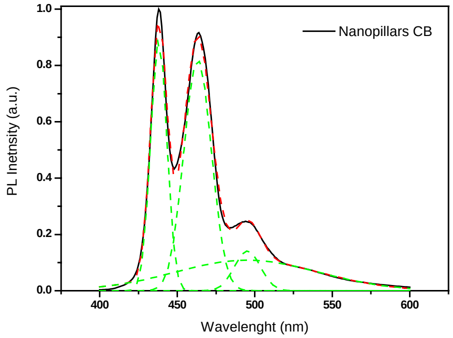

R^2	0.998
y_0	0.00
x_{c1}	438.05
w_1	10.37
A_1	11.69
x_{c2}	463.13
w_2	17.74
A_2	18.30
x_{c3}	495.30
w_3	16.72
A_3	2.97
x_{c4}	494.91
W_4	93.03
A_4	12.65

Fig. B. 11. Gaussian functions for PL of PFO nanopillars (CB).

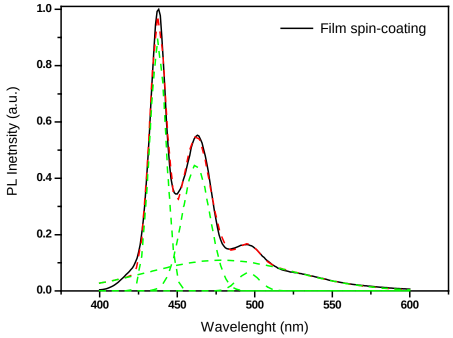

R^2	0.997
y_0	0.00
x_{c1}	437.47
w_1	10.39
A_1	11.65
x_{c2}	462.10
w_2	17.69
A_2	9.97
x_{c3}	495.85
w_3	14.13
A_3	1.15
x_{c4}	478.72
W_4	95.53
A_4	13.07

Fig. B. 12. Gaussian functions for PL of PFO film by spin-coating (CB).

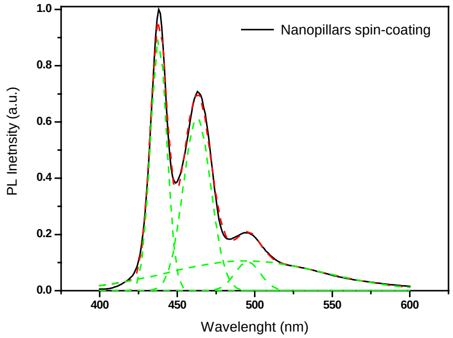

R^2	0.998
y_0	0.00
x_{c1}	437.98
w_1	10.46
A_1	11.81
x_{c2}	462.75
w_2	17.67
A_2	13.67
x_{c3}	495.38
w_3	16.33
A_3	2.11
x_{c4}	494.23
W_4	100.53
A_4	13.36

Fig. B. 13. Gaussian functions for PL of PFO nanopillars by spin-coating (CB).

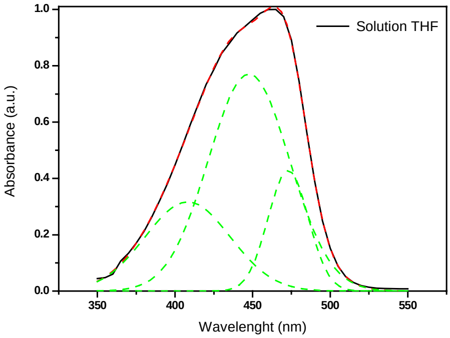

R^2	1.000
y_0	0.00
x_{c1}	408.15
w_1	55.03
A_1	21.83
x_{c2}	447.64
w_2	52.25
A_2	50.48
x_{c3}	472.98
w_3	25.94
A_3	13.93

Fig. B. 14. Gaussian functions for UV-Vis absorption of F8BT solution (THF).

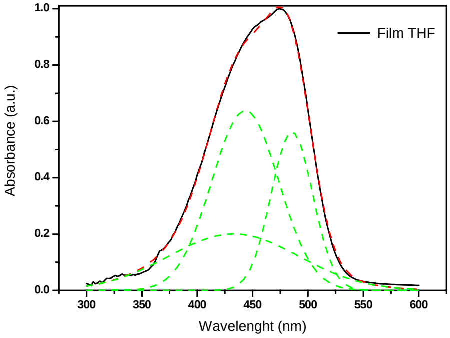

R^2	0.999
y_0	0.00
x_{c1}	432.90
w_1	117.36
A_1	29.51
x_{c2}	443.38
w_2	60.66
A_2	48.55
x_{c3}	485.51
w_3	37.62
A_3	26.55

Fig. B. 15. Gaussian functions for UV-Vis absorption of F8BT film (THF).

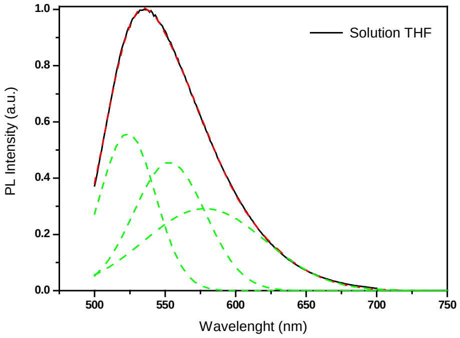

R^2	1.000
y_0	0.00
x_{c1}	523.56
w_1	39.28
A_1	27.59
x_{c2}	553.03
w_2	50.99
A_2	29.14
x_{c3}	578.10
w_3	86.15
A_3	31.51

Fig. B. 16. Gaussian functions for PL of F8BT solution (THF).

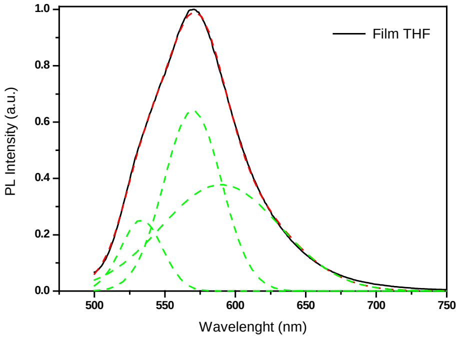

R^2	1.000
y_0	0.00
x_{c1}	533.46
w_1	29.36
A_1	9.35
x_{c2}	569.80
w_2	40.76
A_2	32.80
x_{c3}	589.74
w_3	84.36
A_3	39.99

Fig. B. 17. Gaussian functions for PL of F8BT film (THF).

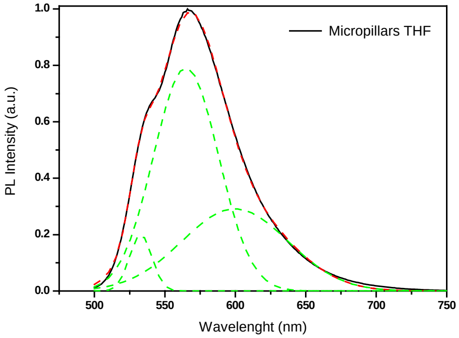

R^2	1.000
y_0	0.00
x_{c1}	532.85
w_1	15.82
A_1	3.98
x_{c2}	564.99
w_2	46.11
A_2	45.75
x_{c3}	599.70
w_3	75.26
A_3	27.48

Fig. B. 18. Gaussian functions for PL of F8BT micropillars (THF).

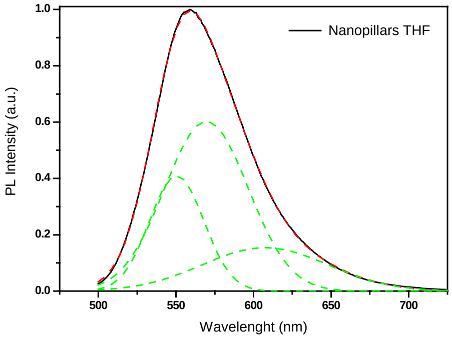

R^2	1.000
y_0	0.00
x_{c1}	550.47
w_1	35.27
A_1	18.07
x_{c2}	569.66
w_2	54.00
A_2	40.72
x_{c3}	607.51
w_3	80.88
A_3	15.64

Fig. B. 19. Gaussian functions for PL of F8BT nanopillars (THF).

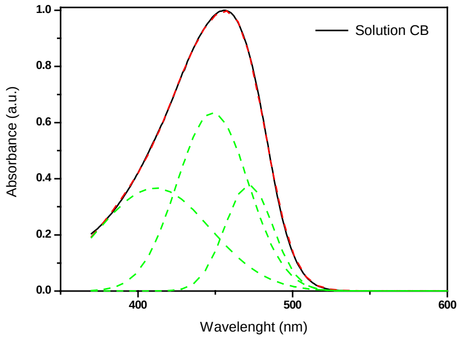

R^2	1.000
y_0	0.00
x_{c1}	410.99
w_1	71.73
A_1	33.02
x_{c2}	448.38
w_2	45.84
A_2	36.75
x_{c3}	471.77
w_3	30.81
A_3	14.74

Fig. B. 20. Gaussian functions for UV-Vis absorption of F8BT solution (CB).

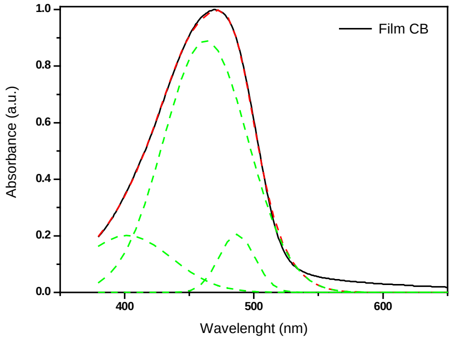

R^2	0.997
y_0	0.00
x_{c1}	401.88
w_1	68.43
A_1	17.29
x_{c2}	462.80
w_2	65.13
A_2	72.87
x_{c3}	486.93
w_3	27.63
A_3	7.14

Fig. B. 21. Gaussian functions for UV-Vis absorption of F8BT film (CB).

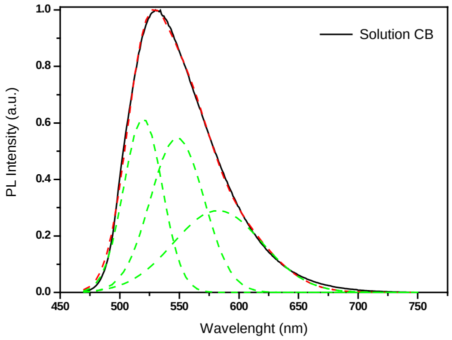

R^2	0.999
y_0	0.00
x_{c1}	519.55
w_1	32.51
A_1	25.10
x_{c2}	548.26
w_2	44.87
A_2	30.79
x_{c3}	582.36
w_3	74.41
A_3	27.02

Fig. B. 22. Gaussian functions for PL of F8BT solution (CB).

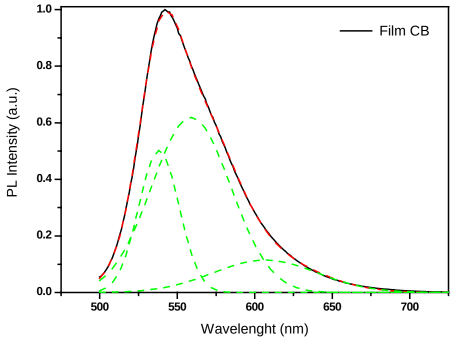

R^2	1.000
y_0	0.00
x_{c1}	538.17
w_1	26.00
A_1	16.38
x_{c2}	606.84
w_2	67.33
A_2	9.67
x_{c3}	558.95
w_3	51.02
A_3	39.55

Fig. B. 23. Gaussian functions for PL of F8BT film (CB).

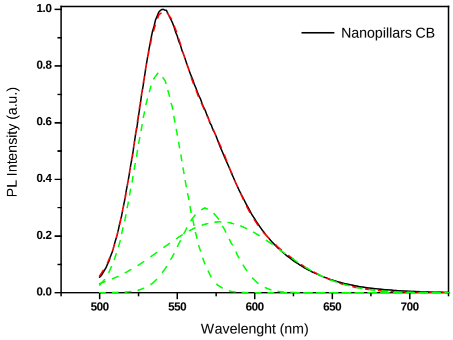

R^2	1.000
y_0	0.00
x_{c1}	538.05
w_1	29.33
A_1	28.65
x_{c2}	568.05
w_2	32.50
A_2	12.18
x_{c3}	577.68
w_3	76.98
A_3	24.12

Fig. B. 24. Gaussian functions for PL of F8BT nanopillars (CB).

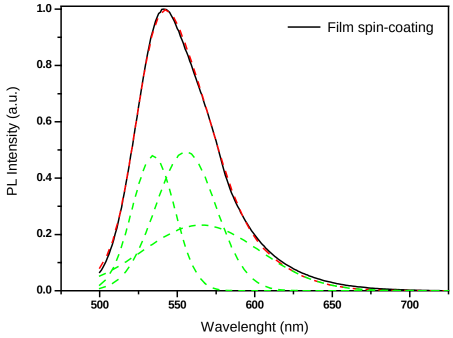

R^2	0.999
y_0	0.00
x_{c1}	534.63
w_1	27.45
A_1	16.55
x_{c2}	555.50
w_2	38.86
A_2	24.12
x_{c3}	565.41
w_3	75.80
A_3	22.17

Fig. B. 25. Gaussian functions for PL of F8BT film by spin-coating (CB).

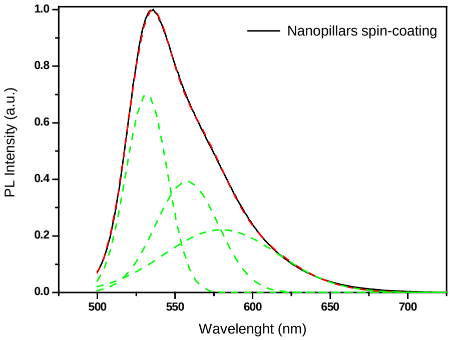

R^2	1.000
y_0	0.00
x_{c1}	531.74
w_1	26.65
A_1	23.49
x_{c2}	557.67
w_2	40.86
A_2	20.09
x_{c3}	579.84
w_3	73.96
A_3	20.55

Fig. B. 26. Gaussian functions for PL of F8BT nanopillars by spin-coating (CB).

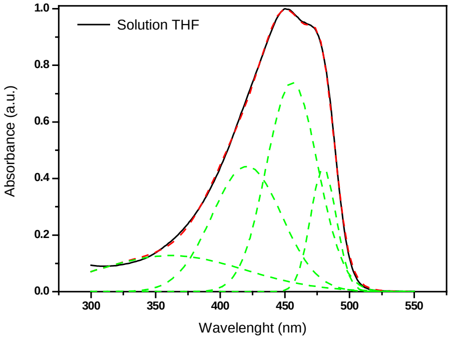

R^2	1.000
y_0	0.00
x_{c1}	361.77
w_1	114.15
A_1	18.24
x_{c2}	455.57
w_2	39.62
A_2	36.68
x_{c3}	479.73
w_3	19.88
A_3	10.86
x_{c4}	420.58
W_4	54.13
A_4	30.07

Fig. B. 27. Gaussian functions for UV-Vis absorption of F8T2 solution (THF).

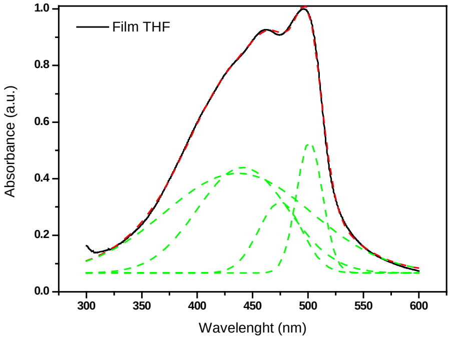

R^2	0.999
y_0	0.07
x_{c1}	436.79
w_1	132.75
A_1	58.58
x_{c2}	441.12
w_2	81.74
A_2	38.21
x_{c3}	474.99
w_3	39.00
A_3	12.24
x_{c4}	501.39
W_4	23.26
A_4	13.60

Fig. B. 28. Gaussian functions for UV-Vis absorption of F8T2 film (THF).

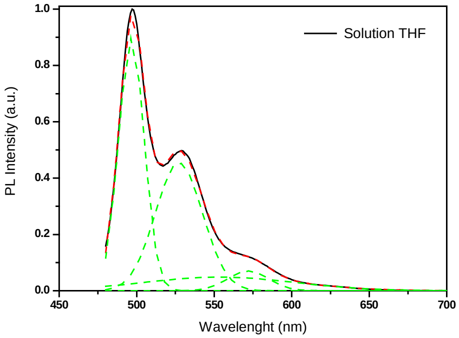

R^2	1.000
y_0	0.00
x_{c1}	496.62
w_1	16.46
A_1	18.48
x_{c2}	527.28
w_2	30.48
A_2	17.37
x_{c3}	571.94
w_3	26.57
A_3	2.34
x_{c4}	553.29
W_4	97.38
A_4	5.95

Fig. B. 29. Gaussian functions for PL of F8T2 solution (THF).

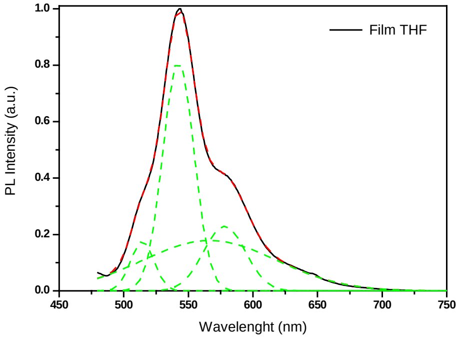

R^2	1.000
y_0	0.00
x_{c1}	514.40
w_1	17.87
A_1	3.96
x_{c2}	542.30
w_2	24.06
A_2	24.68
x_{c3}	577.93
w_3	32.48
A_3	9.35
x_{c4}	566.55
W_4	103.86
A_4	23.25

Fig. B. 30. Gaussian functions for PL of F8T2 film (THF).

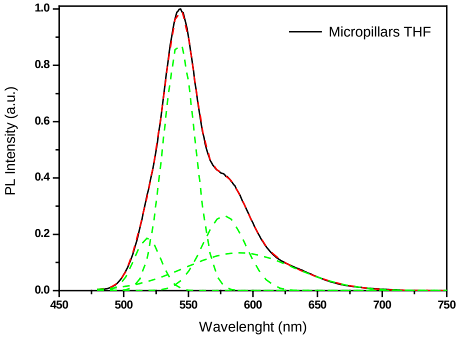

R^2	1.000
y_0	0.00
x_{c1}	514.97
w_1	17.04
A_1	6.01
x_{c2}	543.48
w_2	25.96
A_2	29.20
x_{c3}	579.79
w_3	32.03
A_3	10.31
x_{c4}	588.13
W_4	88.19
A_4	15.18

Fig. B. 31. Gaussian functions for PL of F8T2 micropillars (THF).

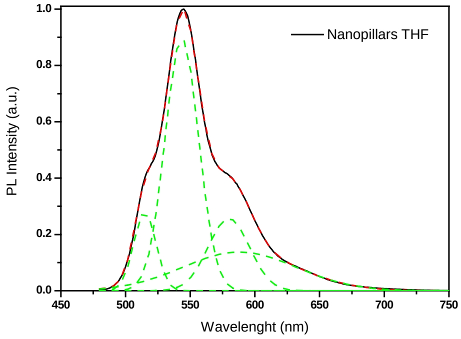

R^2	1.000
y_0	0.00
x_{c1}	518.30
w_1	20.34
A_1	4.77
x_{c2}	542.84
w_2	24.51
A_2	27.21
x_{c3}	577.56
w_3	33.23
A_3	11.16
x_{c4}	589.50
W_4	84.40
A_4	14.19

Fig. B. 32. Gaussian functions for PL of F8T2 nanopillars (THF).

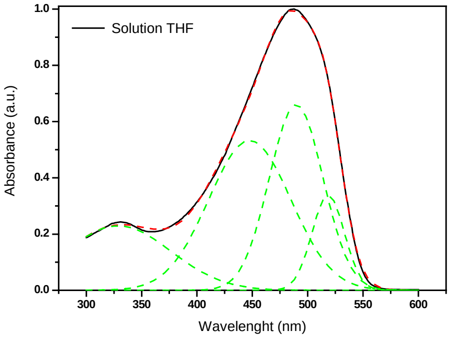

R^2	1.000
y_0	0.00
x_{c1}	328.90
w_1	95.12
A_1	27.35
x_{c2}	447.69
w_2	74.32
A_2	49.58
x_{c3}	489.63
w_3	48.50
A_3	40.11
x_{c4}	518.55
W_4	29.31
A_4	12.43

Fig. B. 33. Gaussian functions for UV-Vis absorption of MDMO-PPV solution (THF).

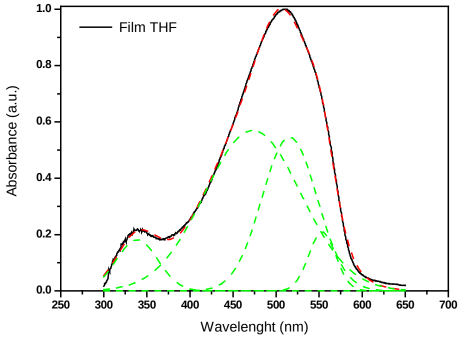

R^2	0.999
y_0	0.00
x_{c1}	338.71
w_1	48.12
A_1	10.96
x_{c2}	472.94
w_2	111.92
A_2	79.94
x_{c3}	515.65
w_3	63.88
A_3	43.77
x_{c4}	553.55
W_4	31.19
A_4	8.23

Fig. B. 34. Gaussian functions for UV-Vis absorption of MDMO-PPV film (THF).

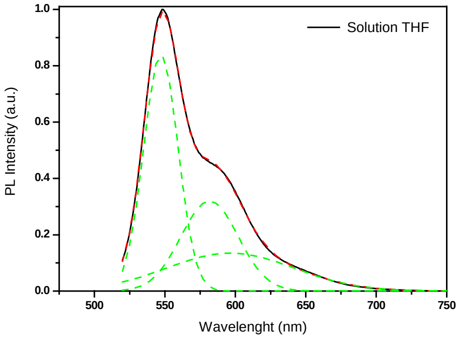

R^2	1.000
y_0	0.00
x_{c1}	547.17
w_1	24.43
A_1	25.76
x_{c2}	581.73
w_2	40.63
A_2	16.30
x_{c3}	596.46
w_3	90.48
A_3	15.27

Fig. B. 35. Gaussian functions for PL of MDMO-PPV solution (THF).

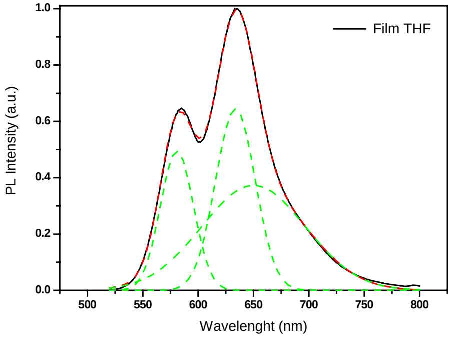

R^2	1.000
y_0	0.00
x_{c1}	580.86
w_1	29.94
A_1	18.58
x_{c2}	633.71
w_2	35.89
A_2	29.02
x_{c3}	649.99
w_3	93.86
A_3	43.82

Fig. B. 36. Gaussian functions for PL of MDMO-PPV film (THF).

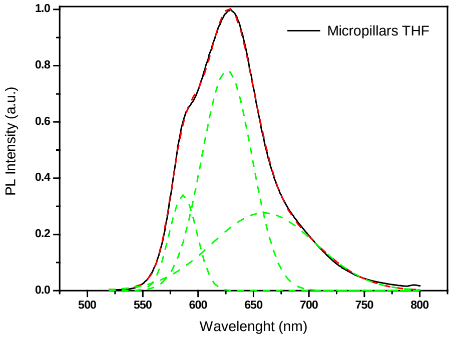

R^2	1.000
y_0	0.00
x_{c1}	586.48
w_1	24.75
A_1	10.55
x_{c2}	625.97
w_2	45.39
A_2	44.61
x_{c3}	659.34
w_3	93.43
A_3	32.39

Fig. B. 37. Gaussian functions for PL of MDMO-PPV micropillars (THF).

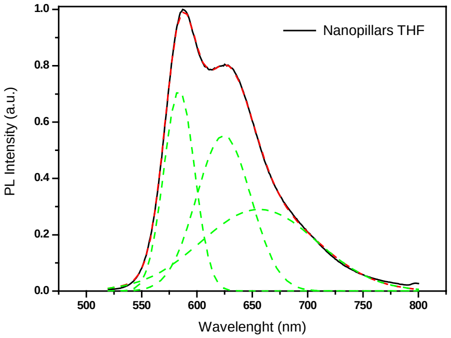

R^2	1.000
y_0	0.00
x_{c1}	583.98
w_1	27.72
A_1	24.79
x_{c2}	624.14
w_2	49.11
A_2	34.02
x_{c3}	656.12
w_3	104.53
A_3	38.02

Fig. B. 38. Gaussian functions for PL of MDMO-PPV nanopillars (THF).

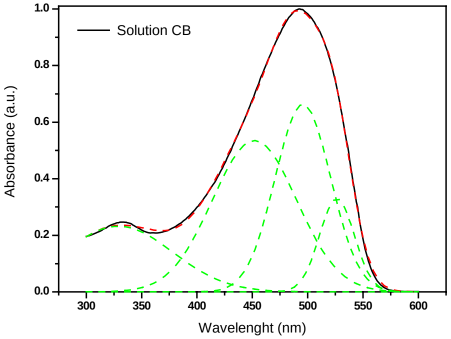

R^2	1.000
y_0	0.00
x_{c1}	329.06
w_1	97.76
A_1	28.49
x_{c2}	451.99
w_2	76.21
A_2	51.08
x_{c3}	495.73
w_3	50.33
A_3	41.83
x_{c4}	526.42
W_4	31.51
A_4	13.03

Fig. B. 39. Gaussian functions for UV-Vis absorption of MDMO-PPV solution (CB).

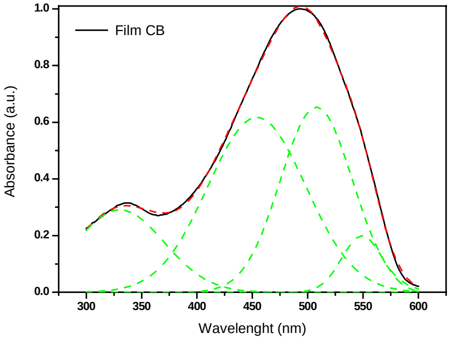

R^2	1.000
y_0	0.00
x_{c1}	330.21
w_1	80.22
A_1	29.28
x_{c2}	454.10
w_2	88.49
A_2	68.45
x_{c3}	507.88
w_3	64.98
A_3	53.24
x_{c4}	549.17
W_4	36.64
A_4	9.15

Fig. B. 40. Gaussian functions for UV-Vis absorption of MDMO-PPV film (CB).

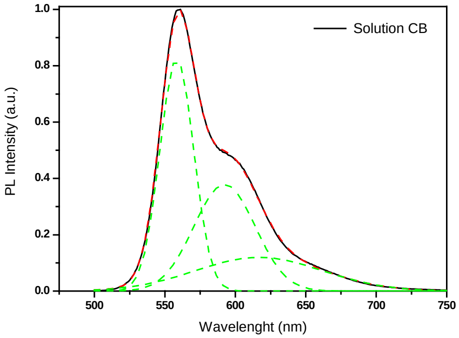

R^2	1.000
y_0	0.00
x_{c1}	558.46
w_1	24.02
A_1	24.90
x_{c2}	592.30
w_2	43.48
A_2	20.64
x_{c3}	616.78
w_3	90.14
A_3	13.52

Fig. B. 41. Gaussian functions for PL of MDMO-PPV solution (CB).

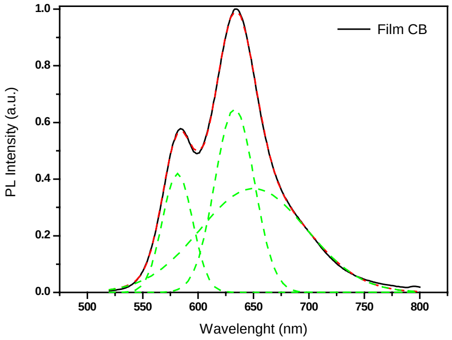

R^2	1.000
y_0	0.00
x_{c1}	581.41
w_1	27.22
A_1	14.34
x_{c2}	632.97
w_2	35.52
A_2	28.93
x_{c3}	649.96
w_3	96.42
A_3	44.27

Fig. B. 42. Gaussian functions for PL of MDMO-PPV film (CB).

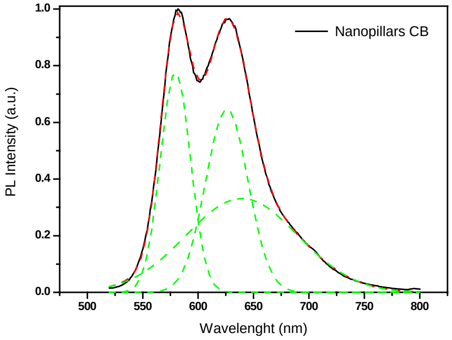

R^2	1.000
y_0	0.00
x_{c1}	579.56
w_1	27.12
A_1	26.49
x_{c2}	625.93
w_2	38.33
A_2	31.10
x_{c3}	639.54
w_3	101.01
A_3	41.93

Fig. B. 43. Gaussian functions for PL of MDMO-PPV nanopillars (CB).

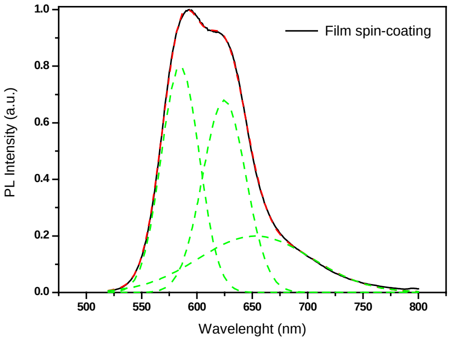

R^2	1.000
y_0	0.00
x_{c1}	584.92
w_1	34.29
A_1	34.40
x_{c2}	624.61
w_2	39.06
A_2	33.31
x_{c3}	652.64
w_3	101.84
A_3	25.47

Fig. B. 44. Gaussian functions for PL of MDMO-PPV film by spin-coating (CB).

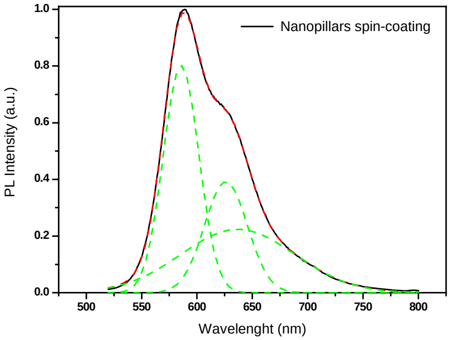

R^2	1.000
y_0	0.00
x_{c1}	585.66
w_1	32.16
A_1	32.33
x_{c2}	626.12
w_2	38.81
A_2	19.08
x_{c3}	636.85
w_3	102.73
A_3	28.77

Fig. B. 45. Gaussian functions for PL of MDMO-PPV nanopillars by spin-coating (CB).

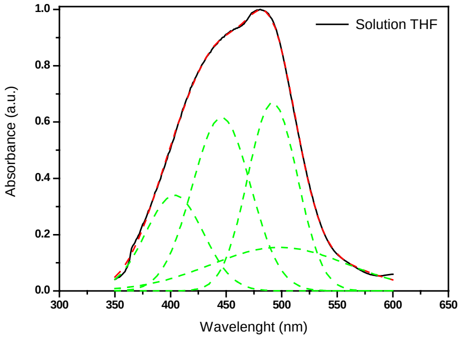

R^2	1.000
y_0	0.00
x_{c1}	403.64
w_1	52.01
A_1	22.19
x_{c2}	445.85
w_2	52.49
A_2	40.55
x_{c3}	491.85
w_3	44.70
A_3	37.47
x_{c4}	498.21
W_4	123.20
A_4	23.92

Fig. B. 46. Gaussian functions for UV-Vis absorption of P3HT solution (THF).

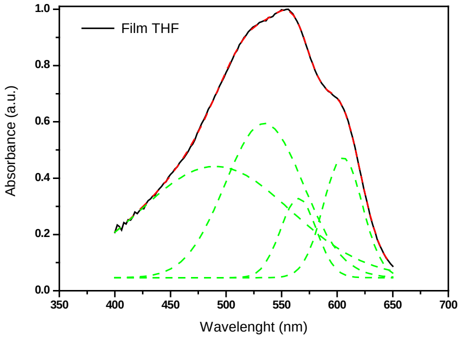

R^2	1.000
y_0	0.05
x_{c1}	490.31
w_1	135.10
A_1	66.94
x_{c2}	534.28
w_2	70.39
A_2	48.37
x_{c3}	565.11
w_3	32.34
A_3	11.43
x_{c4}	605.14
W_4	35.12
A_4	18.78

Fig. B. 47. Gaussian functions for UV-Vis absorption of P3HT film (THF).

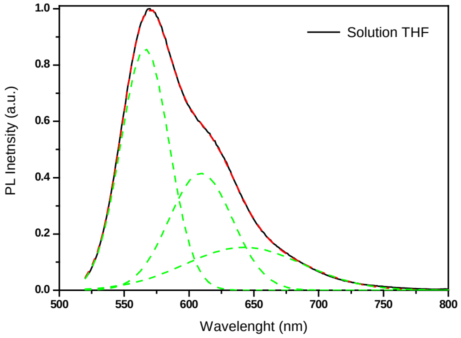

R^2	1.000
y_0	0.00
x_{c1}	566.08
w_1	37.51
A_1	40.34
x_{c2}	609.12
w_2	49.07
A_2	25.55
x_{c3}	642.41
w_3	91.05
A_3	17.39

Fig. B. 48. Gaussian functions for PL of P3HT solution (THF).

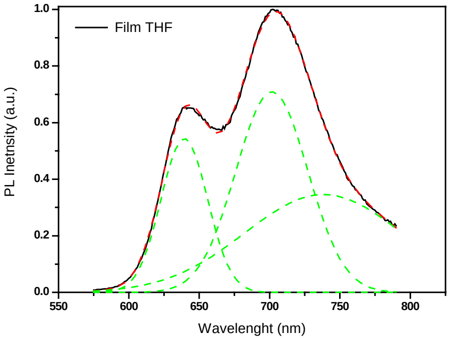

R^2	1.000
y_0	0.00
x_{c1}	639.41
w_1	33.08
A_1	22.54
x_{c2}	701.64
w_2	51.16
A_2	45.46
x_{c3}	738.30
w_3	112.24
A_3	48.61

Fig. B. 49. Gaussian functions for PL of P3HT film (THF).

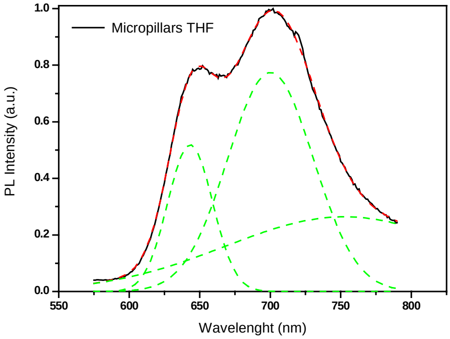

R^2	0.999
y_0	0.00
x_{c1}	643.25
w_1	31.82
A_1	20.72
x_{c2}	700.21
w_2	60.74
A_2	58.97
x_{c3}	752.50
w_3	168.45
A_3	55.76

Fig. B. 50. Gaussian functions for PL of P3HT micropillars (THF).

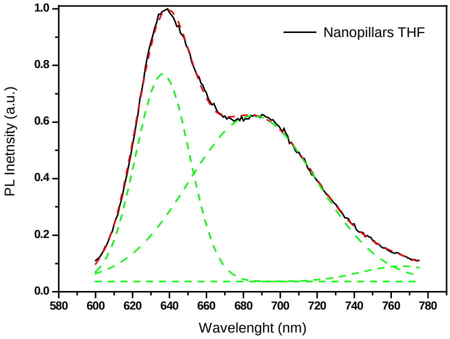

R^2	0.999
y_0	0.04
x_{c1}	636.29
w_1	29.29
A_1	26.98
x_{c2}	685.23
w_2	69.21
A_2	50.83
x_{c3}	765.76
w_3	44.42
A_3	3.02

Fig. B. 51. Gaussian functions for PL of P3HT nanopillars (THF).

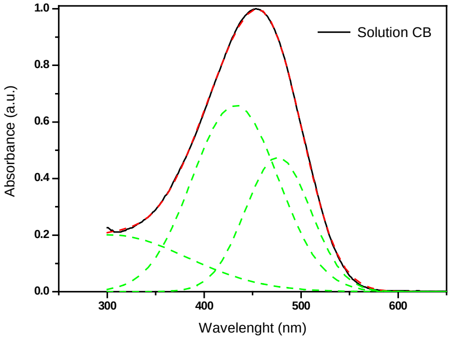

R^2	1.000
y_0	0.00
x_{c1}	303.25
w_1	157.47
A_1	39.67
x_{c2}	432.07
w_2	89.00
A_2	73.53
x_{c3}	476.15
w_3	67.30
A_3	40.19

Fig. B. 52. Gaussian functions for UV-Vis absorption of P3HT solution (CB).

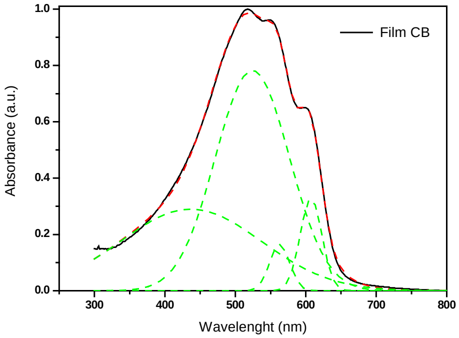

R^2	1.000
y_0	0.00
x_{c1}	436.85
w_1	199.74
A_1	72.55
x_{c2}	524.19
w_2	104.96
A_2	102.97
x_{c3}	562.86
w_3	28.58
A_3	5.92
x_{c4}	607.36
W_4	30.69
A_4	12.70

Fig. B. 53. Gaussian functions for UV-Vis absorption of P3HT film (CB).

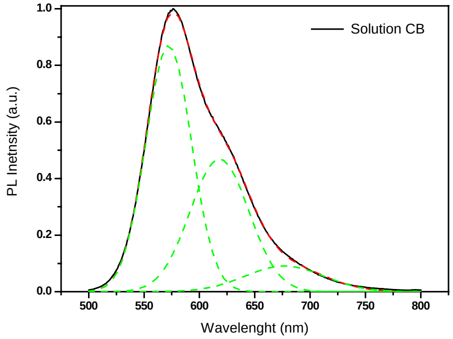

R^2	1.000
y_0	0.00
x_{c1}	572.23
w_1	41.39
A_1	45.14
x_{c2}	676.87
w_2	71.32
A_2	8.11
x_{c3}	618.15
w_3	53.07
A_3	31.23

Fig. B. 54. Gaussian functions for PL of P3HT solution (CB).

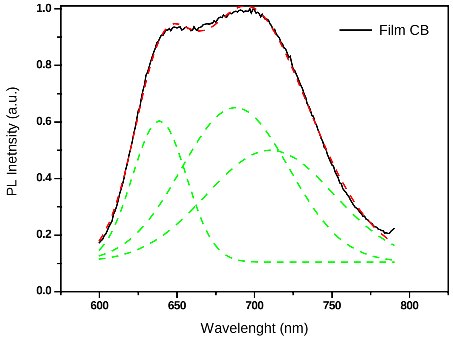

R^2	0.998
y_0	0.10
x_{c1}	638.66
w_1	34.90
A_1	21.85
x_{c2}	687.67
w_2	69.47
A_2	47.54
x_{c3}	710.22
w_3	82.02
A_3	40.65

Fig. B. 55. Gaussian functions for PL of P3HT film (CB).

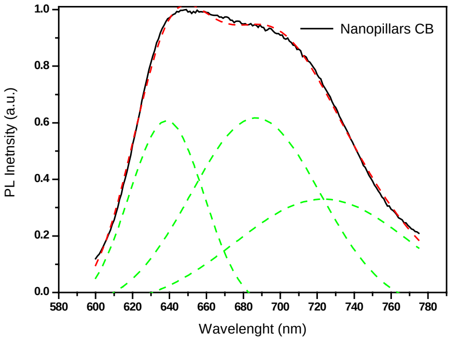

R^2	0.998
y_0	-0.06
x_{c1}	638.44
w_1	40.55
A_1	33.94
x_{c2}	686.71
w_2	69.94
A_2	59.38
x_{c3}	723.23
w_3	95.55
A_3	46.76

Fig. B. 56. Gaussian functions for PL of P3HT nanopillars (CB).

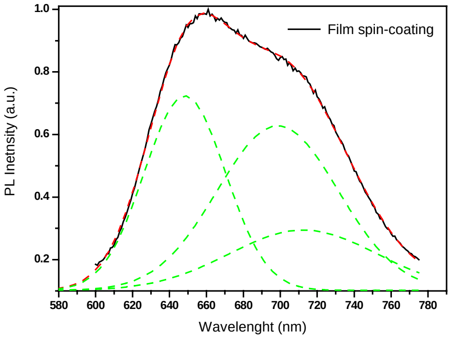

R^2	0.999
y_0	0.10
x_{c1}	648.33
w_1	43.97
A_1	34.28
x_{c2}	698.60
w_2	65.47
A_2	43.16
x_{c3}	712.34
w_3	79.92
A_3	19.30

Fig. B. 57. Gaussian functions for PL of P3HT film by spin-coating (CB).

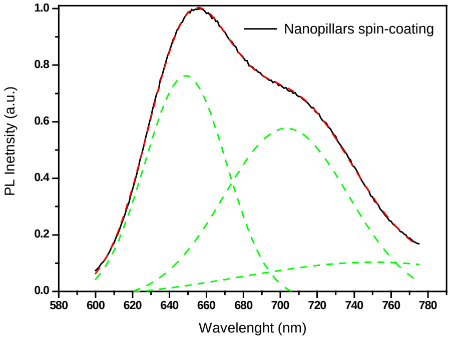

R^2	1.000
y_0	-0.03
x_{c1}	648.75
w_1	44.41
A_1	44.05
x_{c2}	703.28
w_2	67.44
A_2	51.13
x_{c3}	750.64
w_3	144.00
A_3	23.70

Fig. B. 58. Gaussian functions for PL of P3HT nanopillars by spin-coating (CB).

References

[1] B. D. Gates, X. Qiaobing, M. Stewart, D. Ryan, C. G. Willson, G. M. Whitesides, *Chem. Rev.* **105**, 1171 (2005)

[2] A. del Campo, E. Arzt, *Chem. Rev.* **108**, 911 (2008)

[3] G. Chen, S. A. Soper, R. L. McCarley, *Langmuir* **23**, 11777 (2007)

[4] J. Guan, B. Yu, L. J. Lee, *Adv. Mater.* **19**, 1212 (2007)

[5] M. Tormen, L. Businaro, M. Altissimo, F. Romanato, S. Cabrini, F. Perennes, R. Proietti, H.-B. Sun, S. Kawata, E. Di Fabrizio, *Microelectron. Eng.* **73–74** 535–541 (2004)

[6] J. Martín, C. Mijangos, *Langmuir* **25**, 1181 (2009)

[7] V. Gowrishankar, N. Miller, M. D. McGhee, M. J. Misner, D. Y. Ryu, T. P. Russell, E. Drockenmuller, C. J. Hawker, *Thin Solid Films* **513**, 289 (2006)

[8] Y. H. Kang, S. S. Oh, Y.-S. Kim, C.-G. Choi, *Microelectronic Engineering* **87**, 125 (2010)

[9] Z. Cui, *Micro-nanofabrication*, Beijing: Higher Education Press; [Berlin]: Springer, cop. (2005)

[10] A. G. MacDiarmid, W. E. Jones, Jr., I. D. Norris, J. Gao, A. T. Johnson, Jr., N. J. Pinto, J. Hone, B. Han, F. K. Ko, H. Okuzaki, M. Llaguno, *Synthetic Metals* **119**, 27 (2001)

[11] M. Bozniki, W. Czado, T. Frese, A. Schaper, M. Hellwig, M. Steinhart, A. Greiner, J. H. Wendorff, *Adv. Mater.* **13**, 70 (2001)

[12] G. Cao, *Nanostructures and nanomaterials*, London: Imperial College Press, cop. (2004)

[13] O. Ikkala, G. ten Brinke, *Science* **295**, 2407 (2002)

[14] C. R. Martin, *Adv. Mater.* **3**, 457 (1991)

[15] C. R. Martin, *Science* **266**, 1961 (1994)

[16] C. R. Martin, *Acc. Chem. Res.* **28**, 61 (1995)

[17] M. Steinhart, J. H. Wendorff, A. Creiner, R. B. Wehrspohn, K. Nielsch, J. Schilling, J. Choi, U. Gösele, *Science* **296**, 1997. (2002)

[18] J. D. Klein, R. D. Herrick, D. Palmer, M. J. Sailor, *Chem. Mater.* **5**, 902 (1993)

[19] G. A. O'Brien, A. J. Quinn, D. Iacopino, N. Pauget, G, Redmond, *J. Mater. Chem.* **16**, 3237 (2006)

[20] S. Grimm, K. Schwirn, P. Göring, H. Knoll, P. T. Miclea, A. Greiner, J. H. Wendorff, R. B. Wehrspohn, U. Gösele, M. Steinhart, *Small* **3**, 993 (2007)

[21] M. Steinhart, R. B. Wehrspohn, U. Gösele, J. H. Wendorff, *Angew. Chem., Int. Ed.* **43**, 1334 (2004)

[22] M. Steinhart, J. H. Wendorff, A. Greiner, and R. B. Wehrspohn, *Chem. Phys. Chem.* **4**, 1171 (2003)

[23] M. Steinhart, R. B. Wehrspohn, U. Gösele, J. H. Wendorff, *Angew. Chem., Int. Ed.* **116**, 1356 (2004)

[24] M. Aryal, K. Trivedi, W. Hu, *ACS Nano* **3**, 3085 (2009)

[25] X. Liu, F. Xu, Z. Li, J. Zhu, W. Zhang, *Optical Materials* **30**, 1861 (2008)

[26] A. Ulhir, *Bell System Technology Journal* **35**, 333 (1956)

[27] D. R. Turner, *J. Electrochem. Soc.* **138**, 807 (1991)

[28] H. Masuda, K. Fukuda, *Science* **268**, 1466 (1995)

[29] H. Kanaan, P. Jolinat, G. Ablart, P. Destruel, C. Renaud, C. W. Lee, T.-P. Nguyen, *Organic Electronics* **11**, 1047 (2010)

[30] J. W. Nicholson, *The chemistry of polymers*, Cambridge: Royal Society of Chemistry, cop. (1997)

[31] G. Chen, R. L. McCarley, S. A. Soper, C. Situma, J. G. Bolivar, *Chem. Mater.* **19**, 3855 (2007)

[32] J. N. Lee, C. Park, G. M. Whitesides, *Anal. Chem.* **75**, 6544 (2003)

[33] J.-H. Jang, C. K. Ullal, T. Gorishnyy, V. V. Tsukruk, E. L. Thomas, *Nano Letters* **6**, 740, (2006)

[34] R. Farchioni, G. Grosso, *Organic electronic materials*, Berlin; New York: Springer, cop. (2001)

[35] M. Wan, *Conducting polymers with micro or nanometer structure*, Beijing: Tsinghua University Press; Berlin: Springer, cop. (2008)

[36] W. Brütting, *Physics of organic semiconductors*, Weinheim: Wiley-VCH, cop. (2005)

[37] H.-C. Chen, C.-T. Wang, C.-L. Liu, Y.-C. Liu, W.-C. Chen, *Journal of polymer science* **47**, 463 (2009)

[38] D. A. Bernards, R. M. Owens, G. G. Malliaras, *Organic semiconductors in sensor applications*, Berlin, [etc.]: Springer, cop. (2008)

[39] E. Lim, B.-J. Jung, H.-K. Shim, *Macromolecules* **36**, 4288 (2003)

[40] D. O'Carroll, I. Lieberwirth, G. Redmond, *Small* **3**, 1178 (2007)

[41] S. H. Chen, A. C. Su, C. H. Su, *Macromolecules* **38**, 379 (2005)

[42] S. H. Chen, A. C. Su, *J. Phys. Chem. B* **109**, 10067 (2005)

[43] D. O'Carroll, D. Iacopino, A. O'Riordan, P. Lovera, E. O'Connor, G. A. O'Brien, G. Redmond, *Adv. Mater.* **20**, 42 (2008)

[44] M. Ariu, M. Sims, M. D. Rahn, J. Hill, A. M. Fox, D. G. Lidzey, *Physs. Rev. B* **67**, 195333 (2003)

[45] S. K. Lee, T. Ahn, J.-H. Park, Y. K. Jung, D.-S. Chung, C. E. Park, H. K. Shim, *J. Mater. Chem.* **19**, 7062 (2009)

[46] C. L. Donley, J. Zaumseil, J. W. Andreasen, M. M. Nielsen, H. Sirringhaus, R. H. Friend, J.-S. Kim, *J. Am. Chem. Soc.* **127**, 12899 (2005)

[47] J. Zaumseil, R. J. Kline, H. Sirringhaus, Appl. Phys. Lett. **92**, 073304 (2008)

[48] J. Jo, D. Vak, Y.-Y. Noh, S.-S. Kim, B. Lim, D.-Y. Kim, *J. Mater. Chem.* **18**, 654 (2008)

[49] J. Shinar, *Organic light-emitting devices*, New York: AIP Press/Springer, cop. (2004)

[50] M. M. Alam, S. A. Jenekhe, *Chem. Mater.* **16**, 4647 (2004)

[51] M. Watanabe, N. Yamasaki, T. Nakao, K. Masuyama, H. Kubo, A. Fujii, M. Ozaki, *Synthetic Metals* **159**, 935 (2009)

[52] Y. Suzuki, K. Hashimoto, K. Tajima, *Macromolecules* **40**, 6521 (2007)

[53] S. Hotta, S. D. D. V. Rughooputh, A. J. Heeger, F. Wudl, *Macromolecules* **20**, 212 (1987)

[54] S. Hoshino, M. Yoshida, S. Uemura, T. Kodzasa, N. Takada, T. Kamata, K, Yase *J. Appl. Phys.* **95**, 5088 (2004)

[55] J. Piris, N. Kopidakis, D. C. Olson, S. E. Shaheen, D. S. Ginley, G. Rumbles, *Adv Funct. Mater.* **17**, 3849 (2007)

[56] D. E. Motaung, G. F. Malgas, C. J. Arendse, S. E. Mavundla, C. J. Oliphant, D. Knoesen, *Solar energy materials and solar cells* **93,** 1674 (2009)

[57] E. Dovgolevsky, S. Kirmayer, E. Lakin, Y. Yang, C. J. Brinker, G. L. Frey, *J. Mater. Chem.* **18**, 423 (2008)

[58] S. Thorslund, R. Larsson, J. Bergquist, F. Nikolajeff, J. Sanchez, *Biomed microdevices* **10**, 851 (2008)

[59] B. A. Evans, A. R. Shields, R. L. Carroll, S. Washburn, M. R. Falvo, R. Superfine, *Nano Letters* **7**, 1428 (2007)

[60] Y. Tanaka, K. Morishima, T. Shimizu, A. Kikuchi, M. Yamato, T. Okano, T. Kitamori, *Lab on chip* **6**, 230 (2006)

[61] G. Hadziioannou, G. G. Malliaras, *Semiconducting polymers*, Vol. 2, Weinheim: Wiley, cop. (2007)

[62] Z. Bao, A. Dodabalapur, A. J. Lovinger, *Appl. Phys. Lett.* **69**, 4108 (1996)

[63] H. Kaji, K. Koiwai, Y. Hirose, Y. Ohmori, *Organic electronics* **11**, 509 (2010)

[64] G. Hadziioannou, G. G. Malliaras, *Semiconducting polymers,* Vol. 1, Weinheim: Wiley, cop. (2007)

[65] D. H. Kim, Y. Jang, Y. D. Park, K. Cho, *J. Phys. Chem. B* **110**, 15763 (2006)

[66] D. C. Olson, J. Piris, R. T. Reuben, T. Collins, S. E. Shaheen, D. S. Ginley, *Thin Solid Films* **496**, 26 (2006)

[67] M.-C. Wu, H.-C. Liao, S. Chen, Y.-Y. Lin, W.-C. Yen, T.-W. Zeng, C.-W. Chen, Y.-F. Chen, W.-F. Su, *Solar energy materials and solar cells* **93**, 961 (2009)

[68] C. Müller, T. A. M. Ferenczi, M. Campoy-Quiles, J. M. Frost, D. D. C. Bradley, P. Smith, N. Stingelin-Stutzmann and J. Nelson, *Adv. Mater.* **20**, 3510 (2008)

[69] D. Cheyns, K. Vasseur, C. Rolin, J. Genoe, J. Poortmans P. Heremans, *Nanotechnology* **19**, 424016 (2008)

[70] E. L. Ratcliff, J. L. Jenkins, K. Nebesny, N. R. Armstrong, *Chem. Mater.* **20**, 5796 (2008)

[71] H.-S. Wang, L.-H. Lin, S.-Y. Chen, Y.-L. Wang, K.-H. Wei, *Nanotechnology* **20**, 075201 (2009)

[72] A. Bruyant, G. Lérondel, P. J. Reece, M. Gal, *Appl. Phys. Lett.* **82**, 3227 (2003)

[73] H. S. Nalwa, *Silicon Based Materials and Devices,* Vol. 2: *Properties and Devices*, San Diego, Calif. [etc.]: Academic Press, cop. (2001)

[74] J. Charrier, M. Guendouz, L. Haji, P. Joubert, *Phys. Stat. Sol. (a)* **182**, 431 (2000)

[75] L. De Stefano, L. Moretti, A.M. Rossi, I. Rendina, *Sen. Actuators A* **104**, 179 (2003)

[76] J. Volk, J. Balázs, A.L. Tóth, I. Bársony, *Sen. Actuators B* **100**, 163 (2004)

[77] E. K. Squire, P. A. Snow, P. St. Russell, L. T. Canham, A. J. Simons, C. L. Reeves, *J. Luminescence,* **80**, 125 (1999)

[78] M. Hejjo al Rifai, M. Christophersen, S. Ottow, J. Carstensen, H. Föll, *J. Electrochem. Soc.* **147**, 627, (2000)

[79] E. Xifré, *Desing, fabrication and characterization of porous silicon multiplayer optical devices*, Universitat Rovira i Virgili, Spain (2007)

[80] A. Vyatkin, V. Starkov, V. Tzeitlin, H. Presting, J. Konle, U. König, *J. Electrochem. Soc.* **149**, G70 (2002)

[81] V. V. Starkov, *Phys. Stat. Sol. (a)* **197**, 22, (2003)

[82] D. N. Pagonis, A. G. Nassiopoulou, *Microelectronic Engineering* **82**, 1421 (2006)

[83] M. D. Abramoff, P. J. Magelhaes, S. J. Ram, *Biophotonics International* **11**, 36 (2004)

[84] T. Trifonov, *Photonic bandgap analysis and fabrication of macroporous silicon by electrochemical etching*, Universitat Rovira i Virgili, Spain (2004)

[85] V. Lehmann, H. Föll, *J. Electrochem. Soc.* **137**, 653, (1990)

[86] U. Grüning, V. Lehmann, C. M. Engelhardt, *Appl. Phys. Lett.* **66**, 3254, (1995)

[87] P. G. Sheasby, W. E. Cook, *Transaction of the Institute of Metal Finishing* **52**, 103 (1974)

[88] J. W. Diggle, T. C. Downie, C. W. Goulding, *Chemical Reviews* **69**, 365 (1969)

[89] O. Jessensky, F. Muller, U. Gosele, *Applied Physics Letters* **72**, 1173 (1998)

[90] Z. Wu, C. Richter, L. Menon, *Journal of the Electrochemical Society*, **154**, E8 (2007)

[91] F. Y. Li, L. Zhang, R. M. Metzger, *Chemistry of Materials* **10**, 2470 (1998)

[92] A. L. Friedman, D. Brittain, L. Menon, *Journal of Chemical Physics* **127**, 154717 (2007)

[93] O. Jessensky, F. Muller, U. Gosele, *Journal of the Electrochemical Society* **145**, 3735 (1998)

[94] L. Vojkuvka, *Development of technology and applications based on porous alumina nanostructures*, Universitat Rovira i Virgili, Spain (2009)

[95] A. P. Li, F. Muller, U. Gosele, *Electrochemical and Solid State Letters* **3**, 131 (2000)

[96] A. Rauf, M. Mehmood, M. A. Rasheed, M. Aslam, *J. Solid State Electrochem.* **13**, 321 (2009)

[97] V. V. Yuzhakov, H. C. Chang, A. E. Miller, *Physical Review B* **56**, 12608 (1997)

[98] C. E. Caicedo-Martinez, G. E. Thompson, E. V. Koroleva, *Surface Engineering* **18**, 145 (2002)

[99] J. M. Montero-Moreno, M. Sarret, C. Muller, *Surface & Coatings Technology* **201**, 6352 (2007)

[100] G. C. Schwartz, V. Platter, *Journal of the Electrochemical Society* **123**, 34 (1976)

[101] G. C. Schwartz, V. Platter, *Journal of the Electrochemical Society* **122**, 1508 (1975)

[102] L. Vojkuvka, L. F. Marsal, J. Pallares, *Spanish Conference on Electron Devices, Proceedings*, 41 (2007)

[103] D. Chandra, S. Yang, *Accounts of chemical research* **43**, 1080 (2010)

[104] R. Valaski, L. M. Moreira, L. Micaroni, I. A. Hümmelgen, *J. Appl. Phys.* **92**, 2035 (2002)

[105] J. Liu, Y. Shi, L. Ma, Y. Yang, *J. Appl. Phys.* **88**, 605 (2000)

[106] J. Jaczewska, A. Budkowski, A. Bernasik, E. Moons, J. Rysz, *Macromolecules* **41**, 4802 (2008)

[107] G. A. O'Brien, A. J. Quinn, D. A. Tañer, G. Redmond, *Adv. Mater.* **18**, 2379 (2006)

[108] T.-Q. Nguyen, V. Doan, B. J. Schwartz, *J. Chem. Phys.* **110**, 4068 (1999)

[109] C. L. Chochos, S. P. Economopoulos, V. Deimede, V. G. Gregoriou, M. T. Lloyd, G. G. Malliaras, J. K. Kallitis, *J. Phys. Chem. C* **111**, 10732 (2007)

[110] H. Neugebauer, M. A. Loi, C. Winder, N. S. Sariciftci, G. Cerullo, A. Gouloumis, P. Vázquez, T. Torres, *Solar Energy Materials and solar Cells* **83**, 201 (2004)

[111] A. R. Campbell, J. M. Hodgkiss, S. Westenhoff, I. A. Howard, R. A. Marsh, C. R. McNeill, R. H. Friend, N. C. Greenham, Nano Lett. **8**, 3942 (2008)

[112] P. Boland, S. S. Sunkavalli, S. Chennuri, K. Foe, T. Abdel-Fattah, G. Namkoong, *Thin Solid Films* **518**, 1728 (2010)

[113] C. De Marco, E. Mele, A. Camposeo, R. Stabile, R. Cingolani, D. Pisignano, *Adv. Mater.* **20**, 4158 (2008)

[114] H. A. Liu, D. Zepeda, J. P. Ferraris, K. J. Balkus, *ACS Applied Materials and Interfaces* **1**, 1958 (2009)

[115] M. Fakis, V. Gianneta, P. Persephonis, V. Giannetas, A. G. Nassiopoulou, *Optical Materials* **31**, 1184 (2009)

[116] M. C. Gather, D. C. Bradley, *Adv. Funct. Mater.* **17**, 479 (2007)

[117] H.-M. Liem, P. Etchegoin, K. S. Whitehead, D. C. Bradley, *Adv. Funct. Mater.* **13**, 66 (2003)

[118] T. Erb, U. Zhokhavets, G. Gobsch, S. Raleva, B. Stühn, P. Schilinsky, C. Waldauf, C. J. Brabec, *Adv. Funct. Mater.* **15**, 1193 (2005)

[119] D. O'Carroll, G. Redmond, *Chem. Mater.* **20**, 6501 (2008)

[120] E. Lim, B. Jung, J. Lee, H. Shim, J. Lee, Y. S. Yang, L. Do, *Macromolecules* **38**, 4531 (2005)

[121] J. M. Winfield, C. L. Donley, R. H. Friend, J.-S. Kim, *J. Appl. Phys.* **107**, 024902 (2010)

[122] K. Paudel, M. Arif, M. Chandrasekhar, S. Guha, *Phys. Status Solidi B* **246**, 563 (2009)

[123] M. Ariu, D. G. Lidzey, D. D. C. Bradley, *Synthetic Metals* **111**, 607 (2000)

[124] S.-H. Yang, P. Le Rendu, T.-P. Nguyen, C.-S. Hsu, *Rev. Adv. Mater. Sci.* **15**, 144 (2007)

[125] G. McMahon, *Analytical instrumentation*, Chichester, England: John Wiley & Sons, cop. (2007)

[126] H.-H. Perkampus, *UV-Vis spectroscopy and its applications*, Berlin [etc.]: Springer-Verlag, cop. (1992)

[127] L. G. Yanga, Q. H. Zhang, W. Peng, T. C. Huang, L. C. Zeng, P. F. Gu, X. Liu, *Journal of Luminescence* **114**, 31 (2005)

[128] M. Dieterle, G. Weinberg, G. Mestl, *Phys. Chem. Chem Phys*. **4**, 812 (2002)